Surface Topography Effects on Seismic Ground Motion and Correlation with Building Damages during the 2015 Mw 7.8 Nepal Earthquake

MD. ASHRAFUZZAMAN
March 2017

SUPERVISORS:
Prof. Dr. M. van der Meijde
Prof. Dr. N. Kerle

ADVISOR:
Saad Khan, PhD Candidate

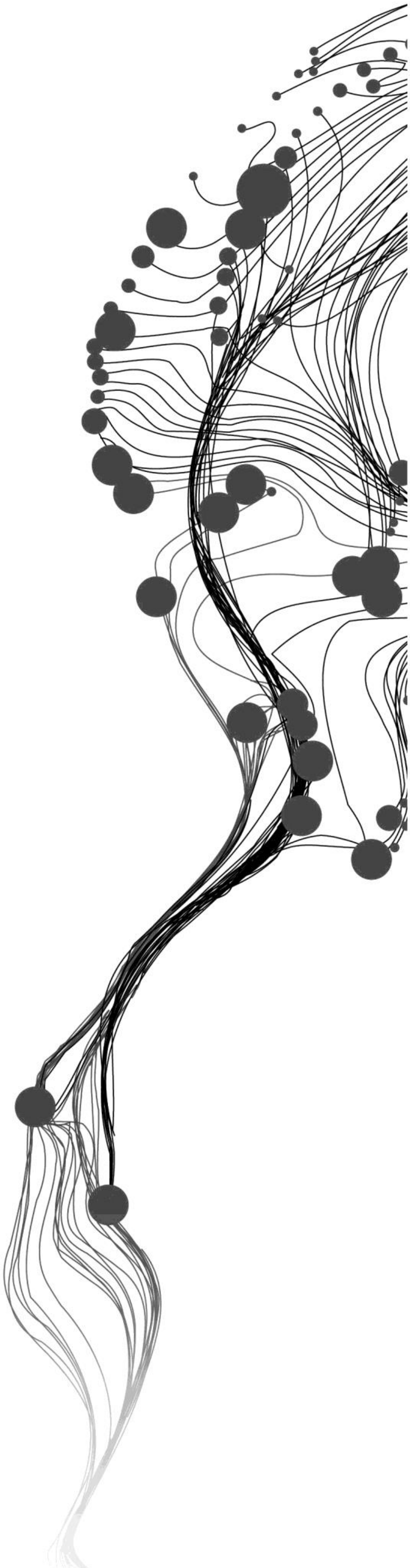

Surface Topography Effects on Seismic Ground Motion and Correlation with Building Damages during the 2015 Mw 7.8 Nepal Earthquake

MD. ASHRAFUZZAMAN
Enschede, The Netherlands, March, 2017

Thesis submitted to the Faculty of Geo-Information Science and Earth Observation of the University of Twente in partial fulfilment of the requirements for the degree of Master of Science in Geo-information Science and Earth Observation.
Specialization: Applied Earth Sciences

SUPERVISORS:
Prof. Dr. M. van der Meijde
Prof. Dr. N. Kerle

ADVISOR:
Saad Khan, PhD Candidate

THESIS ASSESSMENT BOARD:
Prof. Dr. F.D. van der Meer (Chair)
Prof. Dr. Christine Thomas, External Examiner, University of Münster

ABSTRACT

The April 25, 2015 Mw 7.8 Nepal earthquake caused surprisingly limited ground shaking and less damage than might be expected from such major earthquake event. Specially, in the Kathmandu valley, this earthquake produced ground vibration more typical of a smaller earthquake of magnitude 6.0 ~6.5, and the actual ground shaking was almost one-third of the predicted amount. The earthquake was a shallow event that occurred at a depth of ~12 km. Besides, Kathmandu valley is surrounded by the distinct mountains and hills. So, the interaction of the seismic wave field with the surface topography was inevitable. However, the role of surface topography behind this unexpected but fortunate result was unknown.

The overriding purpose of this study was to investigate whether the surface topography played any role behind the limited ground shaking observed during this large event. The research used the spectral element method to develop a 3D geometrical model incorporating realistic earth surface of the Kathmandu valley and its surrounding areas. Then, the seismic wave of the 2015 Mw 7.8 mainshock was simulated through the 3D model to observe the effects. Here, it was shown that during the earthquake, the surface topography acted as a natural insulator of seismic wave, reducing the amount of seismic energy propagating into the valley. As a result, the amplification of peak ground displacement (PGD) in the valley was restricted at very low level (maximum ~10%amplification).

The research also investigated the varying role of surface topography by analysing the expected consequences for hypothetical earthquakes through shifting the earthquake source of the 2015 Mw 7.8 earthquake to four other locations along the fault-rupture propagation path. It was found that the central urbanized area of the Kathmandu valley would experience very high ground shaking if the earthquake source was located around 10 km and 20 km north-west from the actual position. However, the ground shaking would be low (~20% amplification) if the earthquake occurred around 30 km south-east from the actual position. In fourth case, where the earthquake centre was placed 15 km south-east from its real position, half of the valley would suffer violent shaking while other half would feel no shaking. The result indicated that the surface topography would behave differently depending on the position of earthquake source. Such behaviour could range from shielding the valley fully or partly from the earthquake to playing 'no role' in the propagation of seismic wave.

Another very important purpose of this research was to establish the relation between the topography induced amplification with the pattern of observed building damages. Here, the research identified the distribution of amplification value for different grade of buildings damages by performing statistical analysis. The analysis found higher amplification value in higher grade of damages. For example, the average amplification level at each 'destroyed' building position was ~29% whereas it was ~10% for 'Moderate to Severe damage' building. Similarly, the amplification value at each 'No damage' building location was found close to zero. In addition, around 62% cases, the model successfully explained the intensity of damages in the study area. The results indicate that the building damages can be used as an indirect proxy of the ground motion amplification.

The overall findings emphasize that surface topography should be considered for seismic hazard assessment in the Kathmandu valley and surrounding regions.

One Sentence Summary: The position of surface topography prevented the seismic energy to enter into the valley and thereby, restricted the amplification of peak ground displacement to 10% (even de-amplification at many places) and kept the intensity of damage low in the valley interior.

LIST OF ABBREVIATIONS

ARIA	Advanced Rapid Imaging and Analysis
ASCII	American Standard Code for Information Interchange
ASTER	Advanced Spaceborne Thermal Emission and Reflection Radiometer
CBS	Central Bureau of Statistics
CIG	Computational Infrastructure for Geodynamics
CMT	Centroid Moment Tensor
DEM	Digital Elevation Model
DR	Damage Ratio
EMS	European Macroseismic scale
GLL	Gauss-Lobatto-Legendre
GMT	Generic Mapping Tools
GPS	Global Positioning System
InSAR	Interferometric synthetic aperture radar
KTP	Kirtipur Municipality Office, Kirtipur
KKN4	Kakani 4
NASA	National Aeronautics and Space Administration
NGA	National Geospatial-Intelligence Agency
OCHA	Office for the Coordination of Humanitarian Affairs
PGA	Peak Ground Acceleration
PGD	Peak Ground Displacement
PGV	Peak Ground Velocity
SAC	Seismic Analysis Code
SAF	Seismic Amplification Factor
SAR	Synthetic Aperture Radar
SEM	Spectral Element Method
SPECFEM3D	Spectral Finite Element Method 3D
SRTM	Shuttle Radar Topography Mission
UN-OSOCC	United Nations On-Site Operations Coordination Centre
UNITAR	United Nations Institute for Training and Research
UNOSAT	United Nations Operational Satellite Applications Programme

ACKNOWLEDGEMENT

The completion of my thesis required a lot of guidance, mentorship and encouragement from my two supervisors Professor Dr. M. van der Meijde, Professor Dr. N. Kerle and my advisor Mr. Saad Khan. I am extremely fortunate to have got this all along the completion of my thesis. Because of them, I have found MSc research as fun as well as an inspirational learning experience. They are really great mentors. From the core of my heart, I respect and thank them.

I am highly grateful to the Joint Japan World Bank Graduate Scholarships Program (JJ/WBGSP) for fully funding my study. Without their scholarship, it was impossible for me to come to ITC for study.

I am indebted to my employer, Roads and Highways Department, Government of the Peoples' republic of Bangladesh for allowing me to come to the Netherlands for study and communicating with me regularly to check whether I need any help from their end. I will not forget to thank them.

My thanks and appreciation also goes to the colleagues and the teachers of the department of Earth System Analysis, who have really made this department the most dynamic and friendly in ITC premises.

I would like to thank my parents, my spouse and my relatives to continuously provide me mental support which prevented me from having a nervous breakdown under many stressful occasions. During my stay in Netherlands, I have realized that they are the most precious in my life.

Thanks to Almighty God. Without His grace and blessings, this study would not have been possible.

TABLE OF CONTENTS

1. Introduction 1
   1.1. Justification of the Research 1
   1.2. Research Problem 2
   1.3. Research Objectives and Research Question 2
   1.4. The Research in a wider context 3
   1.5. Organization of the Thesis 4
2. Review on Surface Topography Effects on Seismic Ground Motion 6
   2.1. Surface Topography Effects on Seismic Ground Motion: Some Examples 6
   2.2. Evolution of the Studies Performed on Topographic Effects 6
   2.3. Spectral Element Method (SEM) in Seismic Wave Propagation : Some Applications 8
3. Review on M_w7.8 Nepal Earthquake 11
   3.1. Seismicity, Seismotectonic Setting and the 2015 Mw 7.8 Gorkha, Nepal Earthquake 11
   3.2. A Brief Overview of Damage Distribution 13
   3.3. Research Attempt on Earthquake and Ground Motion 13
   3.4. Research Attempt on Building Damages 15
4. Research Methodology 18
   4.1. The Spectral Element Method of Seismic Wave Propagation 18
   4.2. Representation of Nepal Earthquake: Point Source Vs Finite Element Source 22
   4.3. Research Stages 22
5. Results and Discussion 31
   5.1. Surface Topography Effects on Seismic Ground Motion 31
   5.2. Relation Between Seismic Amplification and Observed Buildings Damages 41
6. Conclusions and Recommendations 51

LIST OF FIGURES

Figure 3-1 : Seismo-tectonic setting of the Himalayan region.. 12
Figure 3-2 : Building damages and affected population.. 14
Figure 4-1 : Finite Earth Model 18
Figure 4-2 : Mapping of an element on a reference cube... 20
Figure 4-3 : The five Lagrange polynomial of degree N=4. 20
Figure 4-4 : Methodological flow chart for the study 25
Figure 4-5 : USGS Finite-Fault Model and Position of CMT 27
Figure 4-6 : Classification of damage to masonry and reinforced buildings (EMS-1998) 28
Figure 5-1 : Spectral Element Mesh 31
Figure 5-2 : Distribution of element size for mesh with topography 33
Figure 5-3 : Distribution of element size for mesh without topography 33
Figure 5-4 : Peak Ground Displacement (PGD) Model along with Digital Elevation Model 35
Figure 5-5 : PGD amplification due to the shift of CMT to four different locations 37
Figure 5-6 : Snapshots of displacement wave field for X, Y and Z component 39
Figure 5-7 : Location of Accelerometer and GPS station installed inside the Kathmandu valley 40
Figure 5-8 : Comparison between the observed and synthetic ground acceleration. 40
Figure 5-9 : Damage map of the study area.. 42
Figure 5-10 : 'No Damage' building class overlaid on PGD amplification map. 43
Figure 5-11 : Amplification distribution of 'No Damage' building 44
Figure 5-12 : Destroyed buildings spatially overlaid on PGD amplification map. 44
Figure 5-13 : Amplification distribution of 'Destroyed' buildings 45
Figure 5-14 : Location of destroyed buildings inside the Kathmandu valley on Google Earth Image 45
Figure 5-15 : Spatial overlay of intermediate damage buildings on amplification map 46
Figure 5-16 : Amplification value distribution for all damage classes 47
Figure 5-17 : Total buildings map and Total damage map. 48
Figure 5-18 : Damage data in the valley. 49
Figure 5-19 : Damage ratio map and Amplification map 49
Figure 5-20 : Agreement level between amplification and damage ratio. 50

LIST OF TABLES

Table 1-1: Specific objectives and related research questions 3
Table 5-1: Mesh properties for simulation of seismic wave 32
Table 5-2: Statistics of the Damage Buildings Mapped by NGA, UNOSAT and Copernicus 42
Table 5-3 : Overall summary of amplification value distribution for three damage classes 48

1. INTRODUCTION

1.1. Justification of the Research

The magnitude 7.8 earthquake that struck Nepal on 25 April 2015 surprisingly caused weaker ground shaking and less damage than might be expected from an earthquake of such large magnitude. Especially in the Kathmandu valley, this earthquake produced ground vibration more typical of a smaller earthquake of magnitude 6.0 ~6.5 and the actual ground shaking was almost one-third of the estimated amount (Detweiler & Reddy, 2016; Galetzka et al., 2015; Goda et al., 2015; Hand, 2015; Hough, 2015; Moss et al., 2015; Qiu, 2015; Showstack, 2015). Because of this unusual, unexpected but fortunate result, the scientific community has paid enormous attention to this Mw 7.8 temblor to find out the actual reason behind it. The present research is undertaken from such an interest of identifying the reason of limited ground shaking generated from this major earthquake.

As a result of growing interest among the scientific community, many research efforts have been done so far on the 2015 Nepal Earthquake. These researches, which are reviewed in detail in section 3.2, are divided into two broad types. The first type of research has mainly focused on analysing the processes and the propagation of fault rupture, commonly named as fault-rupture model. This model has claimed that the specific type of fault rupture process and the consequent high-frequency deficient radiated energy is responsible for less shaking. According to this research, the rupture was smooth and slow and when it was closest to the Kathmandu valley, it mainly radiated low-frequency waves which eventually generated less ground shaking. The second type of research is based on seismograph and accelerometer recordings, which mainly has dealt with the response of deep sediment deposits in the valley. This type of research has explained that the deep part of sediment in the bowl-shaped valley reduced the ground shaking. In other words, the first type of research has tried to explain the status of seismic wave before its entry into the valley and the second type of research has described about how the seismic wave was reacted by the sediment after the entrance of seismic wave into the valley regardless of the amount of seismic wave the valley received.

So, two questions have been tried to be answered by the researches so far performed. How and what type of seismic energy was radiated from the source? How the entered seismic energy responded to the sediments inside the valley? However, a third question which is equally important is not yet answered. How much seismic energy was received by the valley before the sediment deposit came into effect? Did deep sediments further reduce the ground shaking which was already reduced to some extent by something else? It is noted that the source of the earthquake was outside the valley and the valley is bordered by complex topography and significant mountains and hills. The rupture propagation path was surrounded by distinct mountains. The earthquake was also a shallow event. As a result, the interaction of seismic wave field with the surface topography was inevitable for this event. So, a third issue, the role of surface topography, came into effect during the earthquake. However, there is no single research done which specifically has dealt with this factor to explain the limited ground shaking observed during the earthquake. The present research is an attempt to fill this research gap by investigating whether the surface topography really played a crucial role in reducing the incoming seismic energy into the valley.

Like the ground shaking felt, the observed damage was also not as intense as feared in the Kathmandu valley (Detweiler & Reddy, 2016; Galetzka et al., 2015; Goda et al., 2015; Hand, 2015; Hough, 2015; Martin et al., 2015; Moss et al., 2015; Qiu, 2015; Showstack, 2015). However, not all affected areas suffered less damage. In the valley, the damage was more pronounced along the valley margin as compared to its interior. Outside the valley, the damage was distributed in a predominant east-west direction. Nevertheless, the damage was more intense in the districts located to the east of the valley whereas the districts located in the west experienced comparatively less damage (Hashash et al., 2015). This research also tries to explore whether the topography-induced seismic amplification can explain or not the particular damage pattern observed in the aftermath of the 2015 Mw 7.8 Nepal Earthquake.

To sum up, the research aims to model the seismic amplification due to surface topography and its correlation with the observed buildings damages for the 25 April, 2015 Mw 7.8 Nepal Earthquake. At first, the study has made an attempt to identify whether the topography plays a role to reduce the incoming seismic wave energy into the Kathmandu valley. The research has tried to explore this issue through numerical representation of realistic topography and simulation of full elastic seismic wave based on the Spectral Element Method-a numerical technique which has already been successfully applied for different earthquake events (e.g., Chaljub, 2006; Jayalakshmi & Raghukanth, 2016; Komatitsch et al., 2004; Lee et al., 2014; Lee et al., 2009; Lee et al., 2008; Raghukanth et al., 2012). Then, correlation analysis has been performed to evaluate the performance of the modelled ground shaking for explaining the damage pattern observed in the valley and surrounding areas.

1.2. Research Problem

In the 2015 Mw 7.8 Nepal earthquake, the maximum amount of seismic energy, the centroid moment tensor (CMT) location (www.globalcmt.org), was released at ~22 km to the north of the Kathmandu valley. After the initiation at approximately 75 km northwest of Kathmandu and a shallower depth of about 12 km, the earthquake propagated towards the valley and released maximum energy at CMT point where the substantial and complex mountains surrounds the valley. So, it is expected that when the seismic wave interacts with the surface topography before or during its entry into the valley, the wave energy shows constructive or destructive interference and is subsequently (de-)amplified. However, no single study has done so far to test it. Moreover, in order to understand clearly about the influence of surface topography on the propagation and amplification of seismic waves, it is very crucial to incorporate more detail and realistic topography into the analysis. Only an exact representation of surface topography can precisely determine the actual role of topography on seismic ground motion.

Not only that, for densely populated areas in rugged terrain like Kathmandu and its surrounding districts, it is very essential for the local government, planners and engineers to know about how much the topography-induced seismic amplification can explain the pattern of building damages.

1.3. Research Objectives and Research Question

The general objective of this study is to assess the role of surface topography on the radiation pattern of seismic wave and amplification of ground as well as to establish the correlation between the seismic amplification and the resulting damage pattern during the 2015 Mw 7.8 Nepal earthquake.

To accomplish the general objective, two specific objectives are needed to be achieved and five research questions (RQ) are essential to be answered by this research. These specific objectives and research questions are presented in Table 1-1.

Table 1-1: Specific objectives and related research questions

Specific Objectives	Research Questions
To analyse the characteristics pattern of the seismic wave radiation due to the shape and position of the topography	RQ-1: Is the seismic energy reduced (or, increased) by surface topography during its entry into the Kathmandu valley? RQ-2: What would be the level of ground shaking if the earthquake would occur at some other locations along the fault rupture line inside the study area? RQ-3: How does the ground amplification vary spatially due to the surface topography?
To establish the linkage between the topography-induced ground amplification and the actual building damages	RQ-4: How effectively can the modelled ground shaking predict the pattern and distribution of damages? RQ-5: To what extent, the distribution and pattern of damages are similar to the distribution and pattern of amplification?

1.4. The Research in a wider context

Earthquakes are considered as one of the most unpredictable and destructive events, which not only causes widespread infrastructural damage and fatalities but also induces other hazards like tsunamis, floods and landslides. Unlike floods and cyclones, accurate prediction of earthquake is not yet possible at the current advancement of science due to a lack of full understanding of the complex fundamental processes of this phenomenon and also its in-built randomness (Geller et al., 1997; Huang et al., 2016). Because of the impossibility of preventing an earthquake, more focus has now been given on effective earthquake preparedness, response and recovery. Whatever the magnitude or mechanism of an earthquake, the ground shaking and damage extent are the two things that the people feel or experience during an earthquake and are, therefore, very important indicators for post-earthquake response, rescue and recovery operations. At the same time, it is equally important to know about how the seismic ground shaking and damages varies spatially in relation to the local site conditions because these greatly help the government, planners and engineers to better plan, design and develop earthquake-resilient urban and rural settlements. In this context, the translation from the interaction between the seismic wave and the site conditions into the estimation of ground vibration or damage distribution is highly beneficial for the society.

What people feel during an earthquake is nothing but the result of the combined effects of the amount of seismic energy released during an earthquake, the pattern and direction of seismic wave radiation, and the interaction of the seismic wave with the local site conditions. A release of larger amount of earthquake energy does not always necessarily mean that people feel more shaking unless the seismic energy radiates and travels towards that particular locations where people live in. When earthquake waves radiate more energy in a certain direction, the surface or sub-surface topography further interacts with the wave and either amplify or de-amplify it. For example, Mexico city suffered heavy damage due to the 1985 Mw8.0

earthquake because of the combination of directivity of seismic energy and soft soil effects, despite the fact that the city's position was 400 km away from the epicentre (Scholl, 1989; National Oceanic and Atmospheric Administration, 2016). In general, people who reside on the upper part of the hills or on areas having soft soils underneath experience longer and higher level of ground vibration. The reason is that seismic ground motions are generally amplified on the top of hills and attenuated at the toe of it. Soft soils trap seismic energy and therefore, amplify ground motion. Moreover, soft soil deposits are more susceptible to liquefaction (i.e., soil acts as a fluid) due to the significant reduction of resistance to shear stress caused by earthquake shaking. So, the intensity of ground shaking of a particular locality depends on the amount of earthquake energy entering into that neighbourhood and the level of amplification or de-amplification of that energy by the local site conditions. In this context, for a given earthquake, it is vital to identify the areas where the high seismic energy enters and amplify the ground motion.

In the aftermath of an earthquake, the most important thing that the government and inhabitants of an area are concerned with is the severity and spatial distribution of infrastructure damages (specially the building damages) and fatalities. Typically, the areas with high ground shaking tend to suffer more damages though it is not true in all cases. However, damage depends not only on the intensity of ground shaking but also on other factors specially the building type (e.g., concrete, cement mortar or masonry), building height, and quality of construction. For example, an earthquake-resistant building can survive under any form of ground shaking whereas a masonry or adobe structure can easily collapse under moderate or low shaking. Actually, the location, height, type and structural engineering information of buildings are generally available in local government or municipality authority. So, if the seismic ground shaking is correctly modelled, the concerned authority can precisely predict the pattern, concentration and distribution of buildings damages. For instance, damage tends to be more pronounced in highly amplified zone. But high amplification does not cause equal damage to all buildings. If a long period ground motion is predominant in the amplified zone then the ground shaking can have a devastating effect on high rise building whereas low rise building may remain unscathed. The opposite thing may happen for short period ground motion. In this context, an accurate estimation of the seismic ground shaking is very important for the authority to correctly identify the vulnerable area for damages as well as types of damages. In other words, actual building damage can be considered as a tool to evaluate the performance of the ground shaking model. So, correlation analysis between the ground shaking and building damages is essential not only for testing the model performance but also for making preparedness plan for future earthquakes.

1.5. Organization of the Thesis

The thesis is divided into the following six chapters:

Chapter One: Introduction-This chapter describes the research gap (why this research?), research problem, research objectives and questions. Moreover, the practical significance of this research in greater context is also covered.

Chapter Two: Review on Surface Topography Effects- The chapter review some evidences of surface topography effects in different earthquakes, evolution of different types of studies conducted on this issue, the strengths and weakness of these studies, evaluation of the spectral element method (SEM) as compared to the other techniques, and some well-known examples where SEM has been successfully applied.

Chapter Three: Review on the 2015 Mw 7.8 Nepal Earthquake –The chapter covers the seismicity and tectonic setting of Nepal , description of the 2015 Earthquake and the observed ground motion and building damages of this event. It also review the studies so far conducted on this earthquake and the building damages.

Chapter Four: Research Methodology- This chapter describes the research stages through which the whole research was performed in order to achieve the research objectives.

*Chapter Five: Results and Discussion-*This chapter summarizes the findings of the results, the interpretation and discussion of the results in relation to the specific research questions.

*Chapter Six: Conclusions and Recommendations-*The chapter discusses the insights gained from the results, the limitation of the research and possible research direction.

2. REVIEW ON SURFACE TOPOGRAPHY EFFECTS ON SEISMIC GROUND MOTION

This chapter presents some examples of surface topography effects on seismic ground motion in different earthquakes. The chapter also briefly describes the different types of studies performed on this topic and the advantages and limitations of these studies. It also explains the justification of using Spectral Element Method in this research. Finally, some examples of using SEM in different earthquake events are presented at the end of this chapter.

2.1. Surface Topography Effects on Seismic Ground Motion: Some Examples

Surface topography effects are commonly known as the modification and (-de) amplification of seismic wave energy by the surface irregularities through scattering, diffraction, focusing and defocusing processes. In mountainous regions, the surface heterogeneity especially the large variation of slope and height makes these processes intense. As a result of these processes, the seismic wave energy is either reduced or increased and the amplitude, frequency and duration of ground motion are changed. For example, during the 2008 Mw 8.0 Wenchuan earthquake, topography reduced the earthquake wave energy in the forward direction of rupture by scattering it in different directions (Zhang et al., 2008). The same pattern of effects was found in Los Angeles Basin as a result of simulation of the 1812 Mw 7.5 earthquake. The peak ground velocity was reduced by 20-30% when the seismic wave cross the topography to enter into the basin (Ma et al., 2007). On the other hand, high peak ground acceleration (PGA) of 1.8g was observed at the vicinity of a small relatively gently sloped hill in Tarzana whereas other areas received PGA of less than 1.0g during the 1994 Mw 6.7 Northridge (USA) earthquake (Bouchon & Barker, 1996; Spudich et al., 1996). Another notable case of topographic amplification is the Pacoima Dam Abutment during the 1971 Mw 6.6 San Fernando (USA) earthquake, where Boore, (1973) concluded that ground motion was amplified by 50 percent at high frequencies due to topography.

There are many examples of earthquakes in which surface topographic effects were profoundly observed in the form of distinct damage pattern in the affected areas. For instance, during the 1985 Mw7.8 Chile earthquake, many four or five storied buildings located on the ridge of Canal Beagle were destroyed (Celebi, 1987). Some other well-known examples are the 1909 Mw6.0 Lambesc (France) earthquake, the 1971 Mw6.6 San Fernando (USA) earthquake, the 1976 Mw 6.5 Friuli (Italy) earthquake, the1995 Mw 6.6 Kozani-Grevena (Greece) earthquake, the 1999 Mw 6.0 Athens (Greece) earthquake and the 2003 Mw6.4 Bingöl (Turkey) earthquake (Assimaki, 2004; Rai, 2015; Restrepo, 2013), the 2009 Mw 6.3 L'Aquila (Italy) earthquake (Celebi et al., 2010), and the 2010 Mw 7.0 Haiti Earthquake (Hough et al., 2010). In these examples, a clear pattern and distribution of building damages were found in top and/or steep slopes of mountainous regions. In recent examples, severe building damages and slope stability failures were observed in the hills and mountains surrounding the Kathmandu Valley during the 2015 Mw 7.8 Nepal Earthquake (Hashash et al., 2015).

2.2. Evolution of the Studies Performed on Topographic Effects

Many research attempts have been made so far to investigate the role of surface topography on seismic wave propagation and ground shaking. These studies can be mainly grouped into two broad categories which are observational/instrumental methods and numerical methods (Assimaki, 2004; Géli et al., 1988; Rai, 2015; Restrepo, 2013). Observational studies are conducted by analysing either the damage distribution in the affected areas or the instrumental recordings. There are many cases where evidence of topographic amplification were marked by observations (e.g., Bouchon & Barker, 1996; Celebi, 1991; Davis & West, 1973; Kawase & Aki, 1990) and/or recorded ground motions (e.g., Griffiths & Bollinger, 1979; Rogers et al., 1974; Shakal et al., 1994; Trifunac & Hudson, 1971). All of these studies generated results that were quite consistent with the theory. According to these studies, the ground motions was amplified on convex features like the top of mountains/hills and de-amplified on concave features such as the toe of hills, valleys and canyons. Therefore, the structures located on those convex features suffered more damages. However, observational studies do not clearly and quantitatively explain the role of topography on ground motions except for some qualitative trends (Géli et al., 1988). There was a clear quantitative disagreement found between the theoretical (based on sophisticated 2D or 3D models) and observational amplifications (Bouchon et al., 1996). Moreover, these studies were limited to the isolated hill/mountain (Shafique et al., 2011) and therefore, are not suitable for analysis on large scale.

In order to address the above limitations, 2D-numerical models (e.g., Assimaki, 2004; Athanasopoulos et al., 1999; Bard, 1982; Boore, 1972; Boore et al., 1981; Bouckovalas & Papadimitriou, 2005; Kamalian et al., 2006; Nguyen & Gatmiri, 2007; Sánchez-Sesma et al., 1982; Smith, 2007) were developed. However, most of the studies were limited to two dimensional ridges and simple topographic shape (Géli et al., 1988; Restrepo, 2013). Moreover, the realistic topography was not fully characterized in those numerical models and many of those used simplified 2D synthetic terrain (Lee et al., 2009). Therefore, 3D numerical models were suggested by the researchers for incorporating realistic topographic characteristics of seismic site into the analysis especially in regional scale in order to precisely estimate the role of topography on the radiation and propagation of seismic energy.

Regarding regional or large scale 3D-numerical simulation of the seismic wave, mainly three different approaches are used: finite differences method (FDM) (Bohlen & Saenger, 2006; Frankel & Vidale, 1992; Pitarka et al., 1998; Sato et al., 1999), finite element method (FEM), (Bao et al., 1998; Bielak et al., 2003; Hughes et al., 2008; Semblat et al., 2008) and spectral element method (SEM) (Lee et al., 2008; Lee et al., 2009; Lee et al., 2009b; Raghukanth et al., 2012; Zhang et al., 2008). FDM is mainly used for simple geometries because this method is inadequate to represent complicated 3D irregular topography and accurate free surface conditions (Chaljub et al., 2005; Komatitsch & Vilotte, 1998; Semblat, 2006). On the contrary, FEM and SEM can easily manage complex and irregular geometrics with numerous heterogeneous media because of which these two modelling techniques have been used in many studies for performing large-scale simulation. But the accuracy of FEM is unknown in many cases and empirical rules are used to determine simulation parameters (Delgado, 2009).

At present, SEM has been increasingly used in simulating seismic wave propagation because of its higher accuracy as compared to FEM (Semblat, 2006). In fact, SEM is a higher order finite element method that can very accurately deal with the implementation of non-flat free surface condition (Chaljub, 2006), geometrical flexibility, local variation of material property (Dhanya et al., 2016), discontinuities in the sub surface and boundary conditions (Delgado, 2009), and precisely incorporate realistic free surface topography (Lee et al., 2009). It has the capability to manage 3D high resolutions simulations of seismic wave propagation (Casarotti et al., 2008). Because of these reasons, SEM is found very promising for simulation of the seismic waves and modelling the ground vibration by integrating realistic earth surfaces. But the performance and reliability of SEM mainly depends on the quality of the mesh incorporating in the volume block (Komatitsch et al., 2005). In SEM, a brick-like high quality hexahedral (i.e., six faces) mesh incorporating real site features is designed though the task may require 'discouraging expertise' (Casarotti et al., 2008) and take months even under expert supervision. Moreover, SEM is computationally expensive. However, because of the superiority of SEM over other techniques, the research has applied this method for modelling surface topography effects on ground shaking for the 2015 Nepal Mainshock. In the next section, some studies of seismic wave propagation using SEM scheme is briefly described.

2.3. Spectral Element Method (SEM) in Seismic Wave Propagation : Some Applications

The SEM is firstly introduced by Patera, (1984) in the field of fluid dynamics. After that, it's application in 3D-seismic wave field modelling was developed by Komatitsch & Tromp, (1999). Since then, the SEM method has been used in solving 3D-problems of seismic wave propagation in different earthquake events. Specially, the effects of realistic surface and subsurface topography on seismic ground motion were investigated by using SEM scheme in many earthquakes. Komatitsch et al., (2004) conducted simulation of ground motion in Los Angeles Basin including San Gabriel Mountains for the 9 September 2001 Mw 4.2 Hollywood earthquake and the 3 September 2002 Mw 4.2 Yorba Linda earthquake. An unstructured mesh of volume 516 km × 507 km × 60 km was designed to resolve seismic waves up to frequencies of 0.5 Hz. The grid resolution at the surface of the mesh is 335 m. The study found significant amplification in the basin. Noted, the study did not fully capture the topography effect on seismic wave propagation, rather it gave more focus on comparing the synthetic data and observed data. A very good agreement was found between them. However, the authors suggested to apply SEM in simulating ground motion at higher frequencies (>2 Hz) for larger and multiple earthquake events for seismic risk assessment on this region.

Ma et al., (2007) simulated the 1812 Mw 7.5 earthquake to study the effect of San Gabriel Mountains (SGB), which are located between San Andreas Fault and Los Angeles Basin (LAB), on seismic ground motion in LAB. They discretized the volume of 209.6 km x 120 km x 46 km by slightly unstructured mesh where three doubling layers were used in three velocity transition zones over the depth. The S-wave speed (Vs) was considered 3464 m/s at the bottom and 500 m/s at the surface of the basin. Because of this configuration, the element size at surface and at the bottom of the mesh was 100 m and 800 m respectively. The maximum frequency that the designed mesh resolved was 0.5 Hz. After simulation, it was found that the San Gabriel Mountains reduced the ground motion in LAB by 20% to 30%, even 50% in some areas. The authors described it as a 'Shielding effect" due to SGB. However, the opposite type of effect was found when simulation was done by placing the earthquake source inside the basin. In that case, surface topography surrounding the basin reflected back the wave energy into the basin and thus, caused amplification of ground motion in basin interior. Because of those results, the authors emphasized to consider large scale surface topography for seismic hazard analysis.

The SEM scheme was extensively used in different studies for earthquakes in Taiwan (e.g., Lee et al., 2014; Lee et al., 2009; Lee et al., 2008; Lee et al., 2009b). In Lee et al., (2008), a SEM mesh was designed to cover a region of 101.9 km x 87.5 km x 102.89 km incorporating low velocity sedimentary Taipei Basin and surrounding surface topography with a view to resolve maximum frequency of 1.0 Hz. The mesh was designed considering depth varying velocity of P-wave (Vp) and S-wave (Vs). The study considered maximum Vp = 6000 m/s and maximum Vs=3464 m/s at the bottom, minimum Vp =3000 m/s and minimums Vs=1155 m/s at the basin surface, maximum density =2700 kg/me and minimum density=2300 kg/m3. In the designed mesh, the average Gauss-Lobatto-Legendre (GLL) distance at the surface was 28 m. The resolution of DEM was 40 m. The simulation considered a small earthquake of Richter magnitude M_L 3:8 occurred on 9.2 km depth on 23 October 2004. The results showed that PGA was amplified in the range of +50% and -50% at the ridge and toe of the mountain respectively, whereas it was amplified by more than 100% by the sediments in the basin. The amplification was mainly influenced by basin depth and slow shear wave speed. The dual behaviour of sediment was also observed. The surface wave was refracted by the sediment in the western edge of the basin causing PGA de-amplified whereas other areas were amplified by the sediment deposit. It was also found that the duration of the ground shaking was increased due to the reflection of wave energy by the surface topography. A second study (Lee et al., 2009) was done with the same configured mesh to analyse the interaction between large scale topography and Taipei basin in different rupture scenarios for the March 2002, Mw 7.0 earthquake. The analysis revealed that for shallow earthquake (at 2 km depth), the Peak Ground Velocity (PGV) in the Taipei basin was reduced because of the scattering of surface wave by the mountains. In contrast, for a deep-hypocentre earthquake (>15 km depth), the PGV was amplified by +50% to +70% as a result of the constructive interference of wave field due to the reflection by the mountains and therefore, the wave propagated and spread into the basin as surface waves. An another study was conducted by Lee et al., (2009b) on small-scale (4.2 km x 3.9 km x 4.6 km) to investigate the effect of high resolution topography on seismic ground motion . The study used 2m LiDAR DEM and 40m DEM and compared the results after simulating a hypothetical earthquake represented by double-couple point source located at a depth of 4.92 km. In both cases, peak ground acceleration was amplified at mountain tops and ridges and de-amplified at the valleys but the high resolution model showed a complex distribution of ground motion with larger value at mountain tops and lower value at valleys as compared to the results based on 40m DEM. Therefore, the study recommended very high resolution mesh to generate ground shaking map for seismic hazard analysis especially for densely populated mountain areas.

Finally, Lee et al. (2014) developed a real time online earthquake simulation system (ROS) via SEM mesh. They designed a mesh by using detail geo-physical and geological data of the region which extends 279.27 km x 428.42 km horizontally and +3.93 km to -110.00 km vertically. The mesh covered most land and offshore areas of Taiwan. The grid resolution at the mesh surface is 545 m. According to the 3D-velocity model used in this study, the maximum and minimum shear wave speed was 4900 m/s and 2450 m/s respectively but in the Taipei basin the minimum shear wave speed was considered at 340 m/s. The mesh was sufficient to resolve the seismic wave frequencies up to 1.0 Hz. The 22 September 2011 Hualian earthquake (Mw 4.3) was simulated and ground motion maps were produced in five minutes. Because of having near real-time simulation capacity and generating ground shaking map in five minutes (it required 117 seconds for getting earthquake information and 3 minutes for simulation), the model was claimed very useful for rapid response after an earthquake event.

Chaljub, (2006) applied SEM for 3D wave propagation in the Alphine valley of Grenoble, France. The study developed SEM mesh for both weak motion (Mw <3) and strong motion (Mw=6) cases. The mesh was accurate up to 2.0 Hz frequencies. The results showed that surface topography was less important in amplifying the ground motion inside the valley (40% variations in PGV) as compared to the amplification at rock sites outside the valley where PGV was amplified by 250%. The comparison between observed and synthetic seismograms showed reasonable agreement in vertical component of PGV but some disagreement was found in horizontal component. According to the author, this disagreement could be improved by tuning the source location and mechanism as well as selecting S-wave velocities more realistic.

Stupazzini et al., (2009) investigated the effects of near-fault and soil non-linearity on ground motion in the same area by applying SEM. The results showed that the location of hypocentre and the valley as well as the directivity effect were the reasons for amplifying PGV up to a factor of 5 and increasing PGV value more than 1m/s even in low to moderate seismicity zones. In contrast, the non-linear behaviour of soil inside the valley was less important as this induced the variability of PGV by a factor of maximum 0.5.

Magnoni et al., (2014) performed numerical simulation of wave for the 6 April 2009 Mw 6.3 L'Aquila earthquake in Italy by using SEM. The full complexities of low wave speed basin, surface topography, attenuation, and Moho discontinuity were incorporated in the mesh of volume 200 km x 200 km x 60 km for resolving wave frequencies up to 0.5 Hz. The generated synthetic peak ground velocity maps were quite consistent with the field observations and the model was claimed very useful for seismic hazard assessment.

In Raghukanth et al., (2012), a chunk of globe covering the area of India and neighbourhood was taken from SPECFEM3D GLOBE (Tromp et al., 2008) for simulating the 18th September 2011 event (Mw 6.9) in Sikkim, India. The simulation for this earthquake showed that the peak ground displacement was dominant in north-south direction, which was due to the effect of rupture directivity and fault orientation. A contour map of PGD was also generated near epicentre region in order to use it for designing underground tunnel, gas and transmission lines in those areas.

The main issue of SEM simulation was discussed by Lee et al., (2014) when centroid moment tensor (CMT) as a single point source of an earthquake was used for simulation. According to the author, it is fairly accurate to represent small earthquakes of magnitude less than 6.0 as single point source. However, for earthquakes of Mw≥ 6.0, it is important to consider the source complexity, slip mechanism and complete propagation path. In that case, the finite source model is required to perform a precise ground shaking simulation. However, the large earthquake can be considered as a multiple source CMTs by which this limitation can be overcome. The similar recommendation was found in Komatitsch et al., (2004) where the authors recommended SEM for finite size sources in place of single point source by summing individual focal mechanism from each point sources located along the sub-faults of a big earthquake. Jayalakshmi & Raghukanth, (2016) divided the fault plane (45 km X 25 km) of a hypothetical Mw 7.1 earthquake into 100 sub-faults of size 4.5 km X 2.5 km each of which was considered as a point source. It is worth mentioning that, multiple CMT sources analysis was performed for different earthquakes. For example, the 2012 Sumatra earthquake (Mw=8.6) and the great 2004 Sumatra-Andaman earthquake (Mw=9.3) were mimicked by two and five point sources respectively (Duputel et al., 2012; Tsai et al., 2005). For the 2015 Nepal earthquake, U.S. Geological Survey, (2016) developed a finite fault model where the whole fault plane (220 km x 165 km) was divided into 121 sub-faults (each with dimension 20 km x 15 km) and CMT solution was provided for 103 sub-faults . However, there are some advantages of using single CMT in place of multiple sub-faults CMTs. According to Yenier & Atkinson, (2014), the single point source is simple and it provides a standard against which the ground motion at near-fault during large earthquake can be compared to differentiate other complex source effects like hanging-wall and foot-wall effects. Moreover, the point source method is computationally efficient if the seismic source is capable to generate earthquake at any location. Furthermore, in seismic hazard analysis, all future earthquakes are generally represented as point source because of which the point source seismic wave simulation is useful (Baker, 2008; Bommer & Akkar, 2012).

Based on the review of the examples of SEM applications for different earthquakes, as mentioned above, some similarities are found. These are (i) the SEM was used for earthquake simulation in very large scale except Lee et al., (2009) (ii) Except Lee et al., (2009) and Ma et al., (2007), the earthquake moment magnitude in all cases were less than 7.0 (iii) All the studies which dealt with surface topography concluded that surface topography was needed to be taken into account for seismic hazard analysis. However, how SEM can be used for seismic hazard analysis is not clear from those studies. The capability of SEM for predicting the consequences for different earthquake scenarios was not evaluated by these studies. The local scale applicability of SEM for major earthquake in high seismicity area like Nepal is also an important issue. Moreover, it is also essential to test the performance of SEM for predicting the damages. However, these issues were also not covered by these studies.

3. REVIEW ON MW7.8 NEPAL EARTHQUAKE

This chapter reviews the seismicity and tectonic setting in Nepal to get an idea about the occurrence of the 2015 Mw7.8 Nepal earthquake. A general description and the consequences of this earthquake are also provided. Finally, a summary of the studies, so far, performed on this event are presented to gain a deeper understanding about this earthquake. This section also helps to identify the research gap that is needed to be filled, based on which the present research is undertaken.

3.1. Seismicity, Seismotectonic Setting and the 2015 Mw 7.8 Gorkha, Nepal Earthquake

Nepal is recognized as a 'Hotspot' of earthquake hazard because of having long history of earthquakes and specially, the country's inescapable and dreadful experience in ten major earthquakes including four most devastating earthquakes in the past, the 1934 Nepal-Bihar earthquake of Magnitude 8.1, the 1833 earthquake of Mw 7.1 ~7.7, the 1505 Mw 8.2 earthquake and the 1255 earthquake of Mw 8+ (Hashash et al., 2015; Elliott et al., 2016; Goda et al., 2015). Because of seismotectonic setting, Nepal is located in high seismic hazard zone where most of the area of Nepal falls in modified Mercalli Intensity (MMI) shaking IX or above for a 475 year return period (Global Seismic Hazard Assessment Program, 1999).

As can be seen from Figure 3-1[a-b], Nepal is located in the central part of Himalayan Arc through which five major thrust fault Main Frontal Thrust (MFT), Main Boundary Thrust (MBT), Main Central Thrust (MCT), South Tibetan Detachment System (STD) and Indus-Yarlung Suture (IYS) have passed through. These faults divided the whole region into four tectonic units Outer Himalaya, Lesser Himalaya, Higher Himalaya, and Tethyan Himalaya (Yin, 2006). The MFT, MBT and MCT converge at the dynamically deformed Main Himalayan Thrust (MHT) which is a detachment along which the Indian plate are separated from the Eurasian (Tibetan) plate (Avouac, 2003; Zhao et al., 1993).The Himalayan mountain range is the result of the collision between these two massive tectonic plates. The Indian plate is continuously sliding beneath the Eurasian plate at a rate of 20-21 mm per year (Ader et al., 2012; Avouac, 2003). The 2400 km x 270 km collision zone extends in 2400 km along east-west direction. Because of the remarkable mountains and continuous aseismic creep along the subduction interface, this region produced many major and great earthquakes throughout the history (Bilham, 1995).

The 25 April 2015 earthquake occurred at 12 km depth on or near the active MHT (Figure 3-1c). The rupture was initiated at 28.1473 latitude and 84.7079 longitude in Barpak village of Gorkha region, about 80 km northwest of central Kathmandu, and propagated in east-southeast direction towards the north of Kathmandu for about 160 km with a duration of ~60 seconds (Qin & Yao, 2016; USGS, 2016b). The rupture dimensions were approximately 160 km along strike, and 120 km down dip located between the gap of rupture zones of the 1934 (Mw 8.1) Bihar earthquake and the 1505 (Mw 8.2) Central Himalayan earthquake and is partly overlapped with the 1833 (Mw 7.3~7.7) earthquake (Figure 3-1a) (Fan & Shearer, 2015; Zhang et al., 2016). In fact, a small part of Main Himalayan Thrust was ruptured by this earthquake (Avouac et al., 2015). According to the Global CMT catalogue (Ekström et al., 2012), the earthquake was as a result of pure thrust mechanism with fault geometry of strike 293°, dip 7°, and rake 108°. The centroid depth was ~12 km located around 20 km north of Kathmandu. The seismic moment of this earthquake is 7.76×10^{20} N-m which corresponds to a moment magnitude of Mw7.8~7.9.

The 2015 Mw 7.8 earthquake is considered as the largest earthquake after the 1934 Bihar-Nepal earthquake. The earthquake caused $7 billion US$ economic losses (Dixit et al., 2015), ~9000 fatalities, ~23000 injuries (Wang & Fialko, 2015), and 290,000 buildings partly or fully damaged (USAID, 2016) in

Kathmandu and surrounding districts. The mainshock was followed by nearly 700 aftershocks out of which five were with Mw>6.0 and the largest one was with Mw 7.3 (Hashash et al., 2015). The earthquake also caused thousands of landslides which made the devastation level worse.

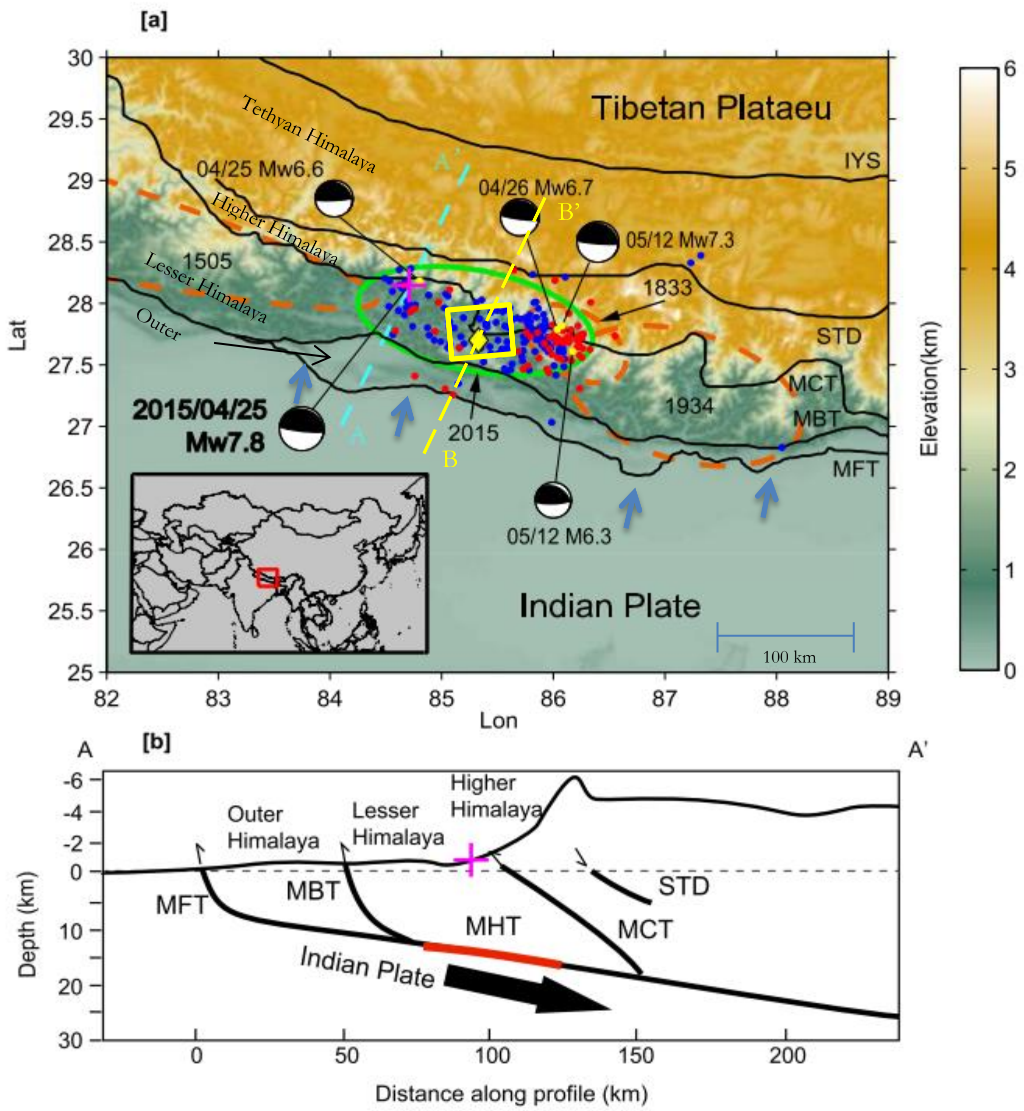

Figure 3-1: Seismo-tectonic setting of the Himalayan region [a] Tectonic setting of the Himalayan Region with topography (modified from Qin & Yao, (2016), p. 73) . MFT=Main Frontal Thrust, MBT=Main Boundary Thrust, MCT=Main Central Thrust, STD= Southern Tibetan Detachment System, IYS=Indus-Yarlung Suture. Purple cross is the epicentre of main shock and yellow dots are the large aftershocks. Their focal mechanism is shown by black and white beach balls. The blue dots are the aftershocks (Mw>3.5) occurred between the mainshock (25 April, 2015) and the largest aftershock Mw 7.3 (12 May 2015). The red dots are the aftershocks (Mw>3.5) occurred after largest aftershocks to till 30 May 2015. The brown ellipses show rupture areas of the 1934 (Mw 8.1), the 1833 (Mw 7.6) and the 1505 (Mw 8.2) earthquake and green ellipse shows fault plane of the 2015 Mw7.8 mainshock. The yellow square is the study area on which the research is performed. The blue arrows describe about the convergence between Indian and the Eurasian (Tibetan) plates towards the north-northeast, which cause Himalayan mountain ranges uplift by approximately 18 mm per year (USGS, 2016b). [b] The cross section along AA' in [a] that shows the approximate location of slip of Mw7.8 Mainshock with epicenter location (purple cross) and approximate fault rupture (red line). MHT= Main Himalayan Thrust.

[c]

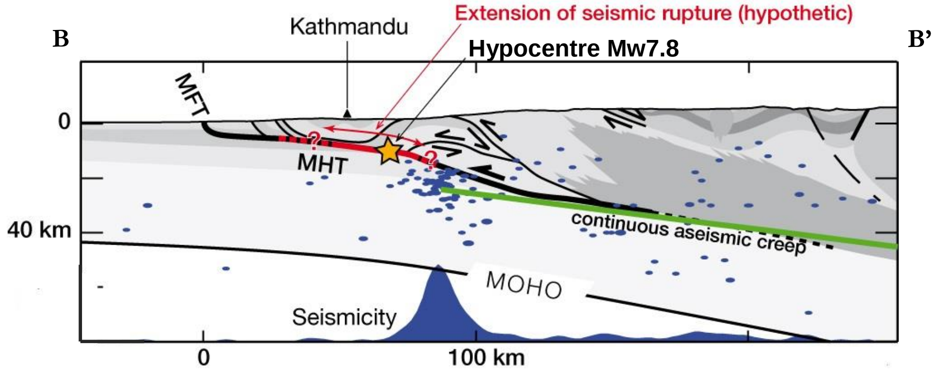

Figure 3-1c: The cross section along BB' in Figure 3-1[a] is shown in [c] which depicts the seismicity of the region. The green line shows the continuous aseismic creep in deeper part of MHT whereas the shallow part of MHT extended to MFT is locked (Grandin et al., 2012) . Figure [c] is modified from IPGP, (2016).

Almost in all of the historical earthquakes in Nepal, the intensity of ground shaking and infrastructure damages was proportionate with the magnitude of earthquake (i.e. the higher the magnitude, the higher the ground shaking and damages) (Lizundia et al., 2016). Based on the past experiences and the ground motion prediction equation as suggested by Boore et al., (2014) the researchers, scientist and experts expected high ground shaking and feared massive loss and damages in the Kathmandu valley and surrounding districts due to the Mw 7.8, 2015 earthquake. According to the Boore et al. (2014) equation, a peak ground acceleration (PGA) of 0.49g was predicted for the Mw 7.8 earthquake but in reality it was found one-third (0.16g) of the estimated PGA (Dixit et al., 2015; Moss et al., 2015). This unusual phenomena raised key questions (Hough, 2015) among the scientific community and urged for investigation and research to find out the actual reason behind it.

3.2. A Brief Overview of Damage Distribution

After the Mainshock, the United Nations On-Site Operations Coordination Centre (UN-OSOCC) with support from Ministry of Home Affairs, Government of Nepal, Multi-National Military and Coordination Centre and Map Action performed the situation analysis and estimated the overall buildings damages. In addition, based on the National Population and Housing Census, 2011, the number of affected population was estimated directly from the number of destroyed buildings. Figure 3-2 presents the worst affected districts in terms of the number of destroyed buildings and affected population. The figure shows that Sindhupalchak, Gorkha, Nuwakot and Ramechhap are the worst affected districts where more than half of the population was suffered by the earthquake.

3.3. Research Attempt on Earthquake and Ground Motion

After the 25 April, 2015 Mw 7.8 earthquake in Nepal, a lot of research was done to analyse the characteristics of the earthquake source, its focal mechanism, rupture process and deformation. Most of the researches were focused on developing finite source models as these models can explicitly explain the physics behind the process of earthquake and therefore, successfully predict the ground motion. As a result, lots of rupture models have been developed for this earthquake. All of these studies used either teleseismic P-wave data (Fan & Shearer, 2015; Koketsu et al., 2016; Qin & Yao, 2016; Yagi & Okuwaki, 2015; Zhang et al., 2016; Zhang et al., 2016b) or geodetic data (GPS, InSAR, SAR and/or strong motion

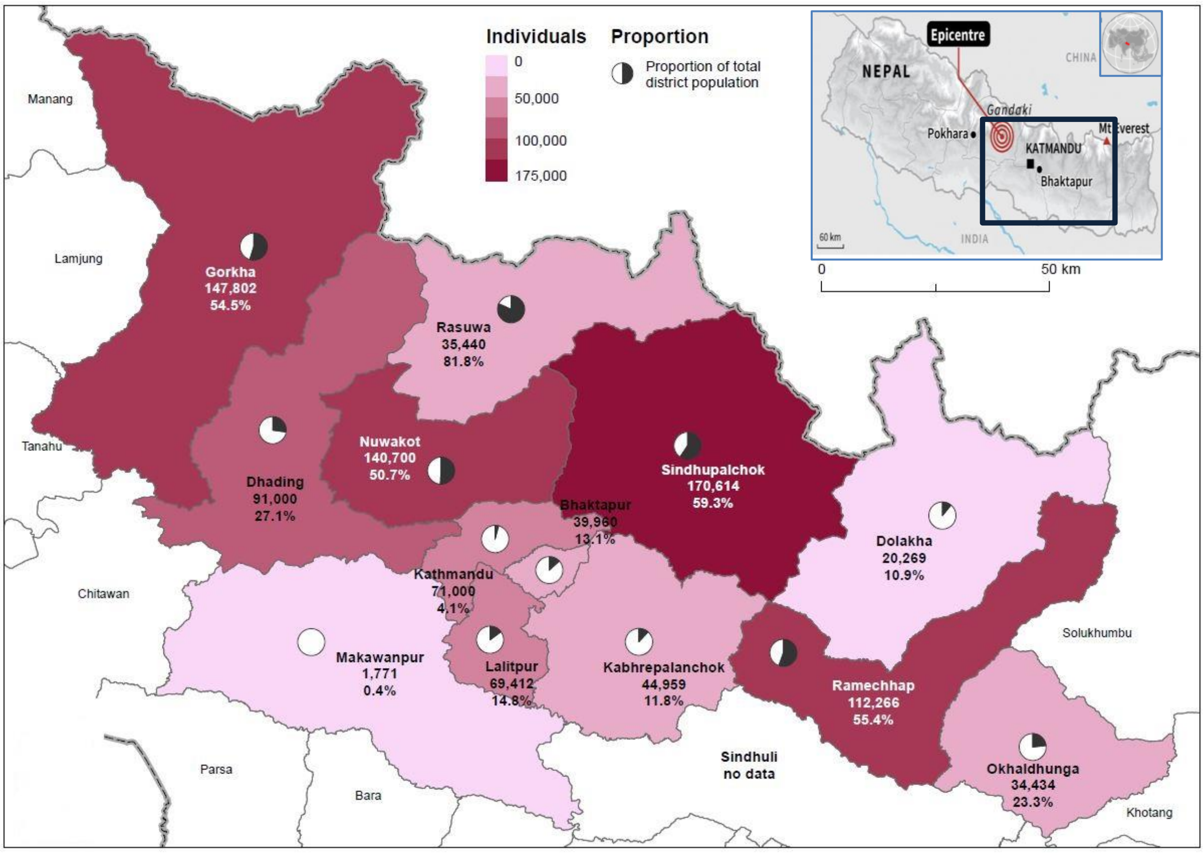

Figure 3-2: Building damages and affected population. The number of population was estimated from the number of 'destroyed' houses. The dark colour indicates highest damage intensity. Source: (OCHA, 2015)

data) (Diao et al., 2015; Lindsey et al., 2015; McNamara et al., 2016; Wang & Fialko, 2015; Yadav et al., 2016) or joint inversion of seismological and geodetic data or combination of multiple datasets or waveforms (Avouac et al., 2015; Galetzka et al., 2015; Grandin et al., 2015; Liu et al., 2016; USGS, 2015b; Yue et al., 2016) . Almost all of the models have explained the similar nature of reasons and mechanism behind this event except some disagreement found in quantifying the earthquake parameter. The main characteristics of this earthquake that these models finally deduced were : (1) the event was as a result of pure thrust mechanism and the rupture propagated unilaterally at ~3.0 km/sec in east-southeast direction from the hypocentre for about 140~160 kilometre along the strike at a depth of 8 ~12 kilometre with duration of about 50 ~80 seconds. (2) The frequency content of the seismic energy varied from 0.05 to 2.0 Hz and high frequency energy was mainly radiated near 1 Hz though there are some disagreements found to identify the locations of high frequency radiation. (3) The large slip area was located to the north of the Kathmandu valley and the maximum slip is 5~6 meter though the slip was slightly overestimated to 7.5 m by Yagi & Okuwaki, (2015) and 7.0 m by Mencin et al., (2016). In addition, rupture directivity released most of radiated seismic energy (0.5 -2 Hz) towards the Kathmandu valley (Galetzka et al., 2015), and (4) The rupture did not reach the surface and is locked in shallower part of Main Himalayan Thrust system which implies increased seismic risk in future. However, except Fan & Shearer, (2015) and Grandin et al., (2015) none of these model explained the reason of less ground shaking observed from such a major earthquake. According to them, the rupture process was smooth and the seismic wave (0.05-0.2 Hz) suffered lack of high frequency energy at the time of releasing maximum seismic moment at a point located at 20 km north of Kathmandu valley, which 'could be' or 'likely' be the reason behind less ground shaking. Avouac et al., (2015) mentioned that the rupture radiated high frequency energy (0.5-2

Hz) for about 45 seconds while propagating along the eastward direction along the strike until it reached close to the Kathmandu valley. After ~45 seconds, the rupture derailed from the along-strike direction and propagated with abruptly decayed amplitude to the southeast direction.

A significant number of researches (Bhattarai et al., 2015; Dhakal et al., 2016; Rajaure et al., 2016; Takai et al., 2016) were also done to analyse the sedimentary basin effect on ground motion during the 2015 Nepal earthquake by using the data recorded on the 4 (four) accelerometers, 1(one) seismograph and 2 (two) GPS stations installed in the Kathmandu valley. All of the researchers found that the long period (3-5 seconds) of energy dominated the seismic ground motion inside the valley and the peak ground acceleration (PGA) (0.15g ~0.24g) was very low as compared to the estimated PGA. Takai et al., (2016) performed a comprehensive analysis using the data of all stations as mentioned above. The research concluded that horizontal ground acceleration was largely amplified on the sedimentary site as compared to the rock site. Moreover, low-frequency energy (~0.25 Hz) was abundant in the seismic wave inside the valley. Dhakal et al. (2016) and Bhattarai et al., (2015) used the single station data from which it was concluded that the deep sedimentary deposit beneath the center of the valley amplified the long period (0.2~0.25 Hz) and de-amplified the short period (>0.5 Hz) of wave. Dixit et al., (2015) used the data recorded in three low cost Quake-Catcher Network (QCN) strong-motion accelerometers where the study claimed that the ground motion was strongly peaked at 5 seconds (i.e., 0.2 Hz) period in the Kathmandu. A conclusion on amplification of sedimentary basin at low frequencies (0.1-2.5 Hz) and de-amplification at higher frequencies (>2.5 Hz) relative to rock sites was made by Rajaure et al., (2016) who specially worked on characterizing basin sediment response during this earthquake. All these researches described this dual behaviour as a non-linear response of soil site. However, these models did not explain the large variation of distribution of ground shaking in and around Kathmandu valley. Takai et al., (2016) suggested more studies on 3-D velocity model to explain the valley response behind less ground shaking observed in the valley interior as compared to its edge.

Though, the 3-D numerical methods has been increasingly used for modelling the seismic ground motion, surprisingly except Koketsu et al., (2016) and Dhanya et al., (2016), no such research was found for this earthquake. However, these two researches did not fully focus on numerical analysis, rather numerical modelling was done to support finite-fault rupture models. Koketsu et al., (2016) conducted simulation of peak ground velocities using finite-element method (FEM) with voxels in a 3D-mesh of size 540 km x 190 km x 64 km in order to identify the effect of Kathmandu basin on ground motion. The analysis found that the horizontal component of ground velocities were amplified twice or more by the sediments at the deepest part (750 m) of the basin but no amplification in the vertical component. Dhanya et al., (2016) applied spectral element method (SEM) to estimate the ground motion at larger scale with coarse hexahedral element (minimum size 3.34 km x 3.34 km x 0.4 km) in 3D-mesh of dimension 800 km x 800 km x 80km but the research was concentrated on analysing low frequency displacements near epicentre region.

3.4. Research Attempt on Building Damages

Few studies on the Mw 2015 Nepal earthquake are found where the reasons behind less damage inside Kathmandu valley have been mentioned. Bhattarai et al., (2015), Galetzka et al., (2015) and Takai et al., (2016) concluded that the long period of ground motion in Kathmandu valley caused more damages to taller structures. In addition, Bhattarai et al., (2015) and Galetzka et al., (2015) indicated that most of the buildings of Kathamndu valley were not high enough (four stories) because of which the overall damage was observed less. According to the Martin et al., (2015), the period of ground motion (~5s) in Kathmandu valley is quite longer than the resonant periods (~0.5s) of vernacular structures most of which are less than five stories tall. As a result, the damage in Kathmandu valley was lower than predicted. In contrast, damage intensities were found higher outside of the Valley because of having large number of vulnerable masonry typed buildings.

Yamada et al., (2016) conducted a damage survey on the buildings located in the Kathmandu valley and the areas to the east and north of the valley. They assigned four damage grades (D1: non-structural damage or minor structural damages, D2: Moderate structural damages D3: Serious structural damages D4: Totally collapsed) based on the damages observed in the structural or non-structural components of the structures. They also defined D2 as partially collapsed and D3-D4 totally collapsed and made it equivalent to the grade 4 and 5 of EMS-98 damage grade respectively. Their study showed that the damage distribution inside the Kathmandu valley was localized and heterogeneous, and the number of totally collapsed buildings was <5%. Outside the valley, this percentage went more than 40% in the Sindhupalchok district and 20-30% in the north areas. Their studied indicated that the earthquake source characteristics might play a role behind less damage in the valley rather the local site conditions.

Unexpectedly, the number of studies which solely focused on developing the relation between ground shaking and damage distribution is very limited. In most of the cases (Gautam et al., 2015; Ohsumi, 2015; Shakya & Kawan, 2016), the damage distributions were studied separately in selected areas through field investigation and, were not spatially linked with ground shaking.

Parajuli & Kiyono (2015) conducted a damage survey of 149 buildings in a small area outside the Kathmandu valley and tried to relate the damage pattern with topography by plotting the buildings of different damage grade onto the elevation contour of the area. The analysis found that buildings located on ridge lines were heavily damaged. Still this limited scale study is not sufficient to establish correlation at regional scale. However, a rapid damage mapping (so called, 'damage proxy map') attempt was made by Yun et al. (2015) in larger scale by using SAR images. According to the prepared proxy map, damages are more pronounced along north-south direction in the west margin of the valley. However, a district named Bhaktapur located in south-east of the valley also suffered heavy damages. The study also revealed that the damage distribution was influenced by the seismic wave directivity and the topography. Nevertheless, the study suggested further work to explore topographic effects on damage distribution.

A comprehensive damage study on 532 buildings was done by Okamura et al., (2015) along the north-south centre line (N-S line) of the valley to analyse the correlation between building damages and ground motion. They also analysed microtremor measurements which were done on 2009. The study found the short predominant period of ground motion in the edge and long predominant period in the centre of valley. Only 5% of the buildings was identified heavily damaged along the N-S line. However, the damage correlation analysis based on one N-S line was sceptical and therefore, the researchers recommended selection of a wider area having denser distribution of damages for detailed correlation analysis. Later, Koketsu et al., (2016) performed numerical simulation to obtain peak ground velocity (PGV) distribution in the area of 540 km x 190 km along the fault plane and linked with the distribution of damage intensities. The study also used fatality rate as a proxy for damage intensity where data was not available. The research concluded that the rupture directivity caused the variation of ground motion and damage intensities and the relation between PGV and damage intensities was 'fairly well'. However, no statistical analysis was done on this study and the concluding remark 'fairly well' was done by visually comparing two maps. Hashash et al., (2015) concluded that the overall damage distribution was asymmetric (more damage in east than west) in the fault plane area and damage was more noticeable along the margin than the valley interior. In the centre of the valley, the damage pattern was more irregular and did not follow any particular trend. Finally, the study highly emphasized on collecting structural, foundation and height information of buildings for making firm conclusion on the damage pattern.

Based on the above literature review, it can be concluded that a lot of researches were done on modelling the seismic ground motion and analysing the building damages after the 2015 Nepal Earthquake. The seismic ground motion modelling mainly focused on the rupture geometry and the role of sediment deposits. However, the role of surface topography was not covered by these studies. Regarding the damage analysis, most of the damage studies were done separately and limited to small areas. Many studies described the damage pattern and identified possible reasons (radiation of long period wave, sediment etc.) behind a particular distribution of damage. But the studies were limited to small scale and performed randomly in different areas in and outside of the valley. However, the reasons behind the overall damage pattern at regional scale were not fully analysed and the spatial relation between the ground shaking and the damage was not fully covered by those studies. Especially, how much the topography-induced amplification is capable to explain the damage pattern inside the valley and surrounding districts is still an unknown issue.

4. RESEARCH METHODOLOGY

As already mentioned in section 2.2, the research used Spectral Element Method (SEM) because of its advantages over other techniques for accurately representing realistic earth surfaces which is very crucial to identify the role of surface topography in influencing seismic wave energy. In this chapter, at first, a brief overview of the SEM is presented. After that, the research stages and the methodology are described in details.

4.1. The Spectral Element Method of Seismic Wave Propagation[1]

The spectral element method (SEM), principally based on the theory of computation fluid mechanics Patera, (1984), has recently been used in various areas of seismology. Basically, SEM is a high-order finite element method which combines the finite element method with the accuracy of spectral method (Meza-Fajardo & Papageorgiou, 2008). This technique is now extensively used to numerically solve the following seismic wave equation (Komatitsch et al., 2005):

$$\rho\, \partial_t^2 \mathbf{s} = \nabla . \mathrm{T} + \mathrm{F} \qquad 4.1$$

Where **s** denotes the displacement at position x and time t, ρ(x) is the 3D- distribution of mass density, and F(x, t) the external body force represents the earthquake. The stress tensor T is linearly related to the strain tensor by the Hooke's law (Tromp et al., 2008):

$$T = c : \nabla \mathrm{s} \qquad 4.2$$

Where, **c** denotes a fourth-order tensor that describes the properties of the medium.

Considering the above wave equation, the modelling domain of SEM can be defined as an earth model with volume $\boldsymbol{\Omega}$, outer free surface $\partial\boldsymbol{\Omega}$, vertical boundary Γ and the unit outward on the normal surface $\hat{n}$ and the location of earthquake source $\mathbf{x}_s$ which are shown in Figure 4-1. The volume $\boldsymbol{\Omega}$ is sub-divided into a number of non-overlapping elements Ωe, e=1,2,……n_e, such that,

$$\Omega = \cup_{e=1}^{n_e} \Omega_e \qquad 4.3 \quad \text{(Komatitsch et al., 2005)}$$

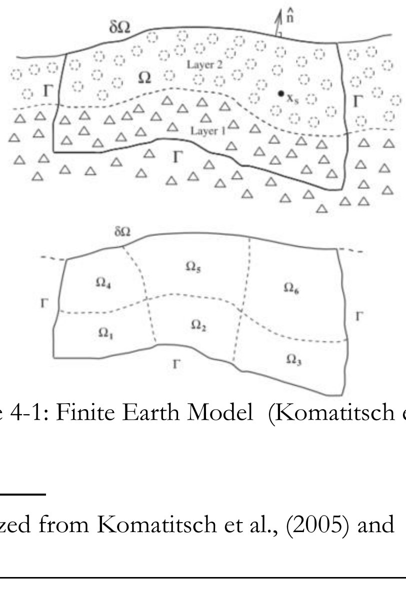

Figure 4-1: Finite Earth Model (Komatitsch et al., 2005, p. 207)

[1] This section is mainly summarized from Komatitsch et al., (2005) and Tromp et al., (2008)

If the study area is not the whole earth (i.e., for local or regional simulations), the vertical boundary Γ works as a fictitious boundary to absorb the seismic energy. On the other hand, for simulation in global scale, no absorbing boundary condition is needed (Komatitsch et al., 2005). However, irrespective of the size of the study area, the free surface **Ω** interacts with the seismic energy and the traction must disappear on this free surface (Tromp et al., 2008) as shown in the following equation:

$$\hat{n}.\mathrm{T} = 0 \quad \text{on } \partial\Omega \qquad 4.4$$

Moreover, at time t=0 (i.e. initial condition), the displacement wave field **s**(x,t) is zero, which is defined by

$$\mathrm{S}(\mathrm{x},0)=0\ ,\ \partial_t \mathbf{s}(\mathrm{x},0)=0 \qquad 4.5 \qquad \text{(Tromp et al., 2008)}$$

Finally, the Xs and F denote the location and external force respectively which defines the characteristics of the earthquake. In spectral element simulation, earthquake is represented by point source which actually explains the seismic moment distribution. The point source can be termed as the seismic moment tensors which explain the movement of fault during an earthquake. The parameters (centroid moment tensors, centroid latitude, longitude, depth, and time) that describe the point source of an earthquake can be obtained from the Centroid Moment Tensor Webpage (Global Centroid Moment Tensor Catalog, 2016).

The location of each subdivided spectral element **Ω**e as shown in Figure 4-1 and Equation$\Omega = \bigcup_{e=1}^{n_e} \Omega_e$ 4.3 4.3 can be defined by Cartesian points X =(x,y,z). Each element is mapped to a reference cube within which the points can be denoted by local coordinates **ξ**= (ξ,η,ζ) where −1≤ξ,η,ζ≤1. Generally, the function which does this transformation is defined by:

$$\mathrm{X}^{\mathrm{e}}(\xi) = \sum_{a=1}^{M} \mathrm{X}_a^e \, N_a(\xi) \qquad 4.6$$

$$\mathrm{X}^{\mathrm{e}}(\xi,\eta,\zeta) = \sum_{a=1}^{M} \mathrm{X}_a^e \, N_a(\xi,\eta,\zeta) \qquad 4.7$$

Where, X_a^e are the M anchor points of the e-th element i.e., $\mathrm{X}_a^e = \mathrm{X}^e(\xi_a, \eta_a, \zeta_a)$, and shape function $N_a(\xi,\eta,\zeta)$ define the geometry of an element. At least 8 (eight) anchors are required to describe the geometry of a spectral element. The mapping of a 3D element on a reference cube is shown in Figure 4-2 .

The shape function $N_a(\xi,\eta,\zeta)$ is generally the products of degree 1 or 2 Lagrange polynomials and their derivatives. A SEM generally uses higher degree Lagrange interpolant (degree 4 to 10) to represent the function of an element. (Komatitsch & Tromp, 1999; Komatitsch et al., 2005; Tromp et al., 2008). In general, if degree of Lagrange polynomial =N, then number of control points (ξ) are $N+1$ which defines the number of Lagrange polynomials. The equation is as follows:

$$\ell_\alpha^N = \frac{(\xi-\xi_0)\ldots\ldots(\xi-\xi_{\alpha-1})(\xi-\xi_{\alpha+1})\ldots\ldots(\xi-\xi_N)}{(\xi_\alpha-\xi_0)\ldots\ldots(\xi_\alpha-\xi_{\alpha-1})(\xi_\alpha-\xi_{\alpha+1})\ldots\ldots(\xi_\alpha-\xi_N)} \qquad 4.8 \quad \text{(Tromp et al., 2008)}$$

Where, $-1 \le \xi_\alpha \le 1, \alpha = 0, \ldots, n$

If degree of Lagrange polynomials $N = 1$, then number of control points are two ($\xi = -1, \xi = 1$) and the polynomials are:

$$\ell_0^1(\xi) = \frac{(\xi-(+1))}{(-1-(+1))} = \frac{1-\xi}{2}\ ,\ \ell_1^1(\xi) = \frac{(\xi-(-1))}{(-1-(-1))} = \frac{1+\xi}{2}$$

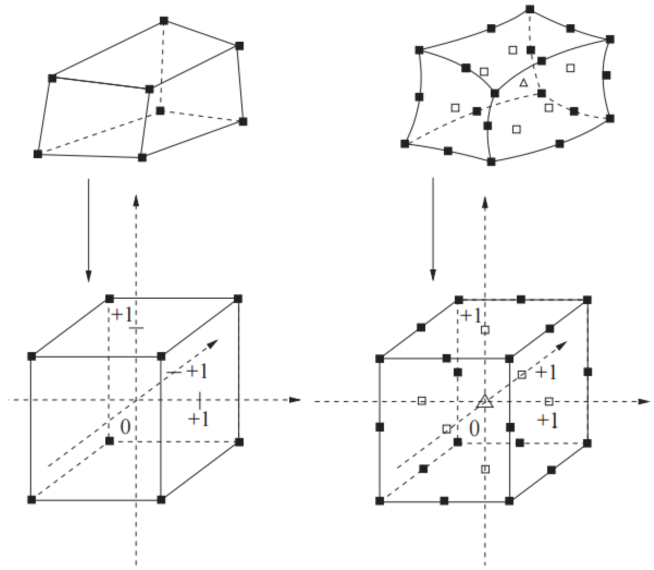

Figure 4-2: Mapping of an element on a reference cube. (Schuberth, 2003, p. 57). (Left) Eight control nodes with straight edges and faces. (Right) Twenty seven control nodes (eight corners plus twelve edge centres showed black squares, plus six face centres showed by open squares plus the centre of the whole element)

Similarly, if $N = 2$, the control points are $\xi = -1, \xi = 0, \xi = 1$ and the Lagrange polynomials are:

$$\ell_0^2(\xi) = \frac{(\xi - (+1))\,(\xi - 0)}{(-1 - (+1))\,(-1 - 0)} = \frac{\xi^2 - \xi}{2}$$

$$\ell_1^2(\xi) = \frac{(\xi - (-1))\,(\xi - (+1))}{(0 - (-1))\,(0 - (+1))} = 1 - \xi^2$$

$$\ell_2^2(\xi) = \frac{(\xi - (-1))\,(\xi - 0)}{(1 - (-1))\,(-1 - 0)} = \frac{\xi^2 + \xi}{2}$$

So, in a SEM, the control points ξ_α are chosen to be $N + 1$ Gauss-Lobatto-Legendre (GLL) points. If Lagrange polynomials and GLL quadrature is used together, the mass matrix is exactly diagonal which is very important for numerical accuracy. The Lagrange interpolants of degree 4 and the distribution of associated GLL points to discretize the wave field are shown in Figure 4-3.

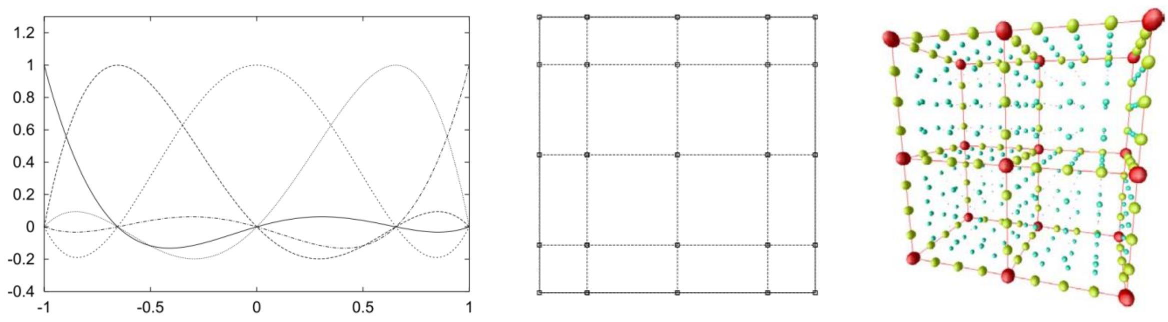

Figure 4-3: The five Lagrange polynomial of degree N=4. (Left Figure): The Lagrange polynomials are, by definition, equal to 1 or 0 at each of GLL points. Because of this, the mesh element must have to be hexahedra. (Middle and right Figure): Distribution of GLL points which are non-evenly spaced. Each 2D-face contains $(n + 1)^2$ GLL points. Each 3D-spectral element of mesh contains $(n + 1)^3$ GLL points. Here evenly spaced GLL points have been shown for simplicity (Carrington et al., 2008; Komatitsch et al., 2005, p.214)

In a SEM, if the degree of Lagrange interpolants is less than four, the performance of SEM is similar to FEM which suffers a great amount of numerical dispersion. Choosing the degree greater than 10 makes the SEM very accurate to solve the seismic wave propagation but in this case, the computational cost is very high. As GLL points are non-evenly spaced, a high degree make GLL points clustered together at the edge of the element. Because of very close distance between the GLL points, very small time step is required which make the spectral-element simulation very expensive (Canuto et al., 1988).

According to the principles behind the subdivision of model domain into non-overlapping hexahedral element and the use of Lagrange polynomials of degree between 4 to 10 during SEM meshing, the following conditions must have to be fulfilled during designing of all-hexahedral conforming mesh in order to ensure the numerical accuracy and stability of SEM for simulation of seismic wave propagation:

1. Though SEM uses Lagrange Polynomials of degree (N) 4 to 10, the selection of N for a model depends on the grid spacing or the size of the elements d. The element size should be selected such that at least five GLL nodes per minimum wavelength throughout the entire model is ensured for sampling the seismic wave field (Komatitsch & Vilotte, 1998) . This can be summarized by the following equation (Cupillard et al., 2012):

$$d \leq \frac{N}{5} \vartheta_{min} T_0 \qquad 4.9$$

Where, ϑ_{min} is the minimum seismic wave speed, T_0 is the shortest period that the model resolve. The product of this two determine the shortest wavelength (λ_{min}) of seismic wave propagated through the mesh.

2. To ensure stable time scheme for spectral-element simulation the selection of time-step Δt is restricted by the following equation:

$$\Delta t \leq C \, min_{\Omega}(\frac{\Delta x}{\vartheta}) \qquad 4.10$$

Where, C is the Courant stability number usually varies between 0.3 to 0.4, Ω is the model volume, Δx is the distance between two GLL nodes and ϑ is the P-wave speed.

3. The quality of mesh depends on the level of distortion in each element. A large distortion may cause numerical error. So, the mesh requires an acceptable level of geometrical distortion of the elements. In ideal case, there is no distortion. This means, the six sides of a hexahedral element are in full contact of the sides of other neighbouring elements. In another way, it can be said that the angle between the edges of the faces of every element of a mesh should be perfectly 90 degree. If it deviates from the 90 degree angle, the element is defined as distorted. The level of distortion is measured by the skewness. A skewness value of '0' means no deviation from the right angle position (i.e. perfect hexahedral element) and '1' means maximum deviation (i.e. very bad element). Fortunately, in SEM mesh, the elements with very high distortion perform well if higher degree of polynomials $N \geq 6$ is used (Oliveira & Seriani, 2011). For N=4, the skewness should be limited to <0.8 (Casarotti et al., 2008).

To sum up, the key features during designing of mesh and simulation of seismic wave under Spectral Element Method (SEM) are the followings:

I. The SEM discretization process requires that the model domain is decomposed into a number of non-overlapping hexahedral elements.
II. In each spectral element, the interpolation nodes are GLL nodes where the displacement and its spatial derivatives are evaluated. This means that the representation and spatial integration of functions on hexahedral elements is based on GLL points (Casarotti et al., 2008)
III. The number of grid points per minimum wavelength is required to be the same everywhere in the model. This implies that the size of the element of a particular region of a mesh depends on the wave speed of that region. The higher the wave speed, the higher the element size is allowed to be. In another way, it can be stated that the slowest wave speed control the resolution of the mesh.
IV. The selection of the size of the element for resolving a certain amount of seismic wave frequencies and the time step for ensuring stability of the spectral-element simulation is controlled by the equation 4.9 and 4.10. A very small element in high seismic wave speed region means that the time step required for stable simulation is very small which ultimately make the simulation very expensive.

4.2. Representation of Nepal Earthquake: Point Source Vs Finite Element Source

As already mentioned in literature review (section 2.3 and 3.3), the finite source model is the preferred choice for large earthquake like the Nepal mainshock, because it explicitly deals with the source complexity, fault-rupture geometry and rupture directivity. However, the research used a point source model for this earthquake. There were few reasons behind it. First: The study area (58 km x 57 km) was significantly small as compared to the fault plane (220 km x 165 km) of this earthquake. As the area of the fault plane extends far beyond the study area, a point source representation of Mw 7.8 earthquake for this study area was justifiable. Second: each-sub fault under finite fault model is not independent. So, all sub-faults need to be considered if a finite fault model is used. On the other hand, the single point source is independent of the whole fault plane. Third: The point source concept is efficient if an earthquake can occur to any location within the study area. In this case, the point source can be shifted to any location within the study area to see the consequence of each placement of point source. Fourth: The point source concept is simple and fifth: Incorporating the whole fault plane into the SEM mesh would require a significant amount of computational facilities. Still that would be possible, if the grid spacing of DEM and the element size would be increased significantly. However, this could lose the detail of topographic information, because of which the simulation could not be realistically performed.

4.3. Research Stages

The whole research was performed in two parts and six stages Figure 4-4 [a-b]. The Part-1 consists of four stages (Stage S1 to S4) that deal with the modelling of surface topography effect on seismic wave energy. The stages S1 to S4 were done for both cases of actual surface topography and assumed plain surface (i.e. without surface topography) of the study area. These are shown in the left and right part of the flow chart (Figure 4-4a) respectively. The analysis was made based on peak ground displacement (PGD). At the end of this part, ground motion maps (i.e. Amplification Map) were developed. These maps were used in Research Part-2. This Part was covered in two stages (Stages S5 to S6) (Figure 4-4b) to analyse the relation between the seismic ground motion and building damages. The description of each stage is provided below:

4.3.1. Stage 1: Construction of the Mesh for the Study Area

Designing of the mesh is the most crucial step for accurate simulation of seismic wave (Komatitsch et al., 2005; Lee et al., 2008). In this stage, a brick-like six faces hexahedral mesh incorporating realistic free surface topography of the Kathmandu valley and its surrounding areas was constructed by SEM method.

The SRTM Digital Elevation Model (DEM), which is freely available, was used for incorporating realistic surface topography into the SEM hexahedral mesh. The research used SRTM DEM ~270m (9 arc seconds grid spacing) to develop a 3D numerical model.

However, it was important to consider the resolution and accuracy of DEM for developing 3D surface topography model. DEM resolution coarser than the topographic features lose information about the surface irregularities and therefore, the accuracy of the output would be under question. The morphometric properties like slope, internal relief, aspect and curvature of the topography heavily influence the scattering, diffraction, focusing, trapping and reflection pattern of seismic wave which are very crucial factors for increasing or decreasing ground amplification (Shafique et al., 2011). The finer resolution and the higher accuracy of DEM truly represent the actual morphometric properties of the seismic site from which the seismic ground amplification could be precisely modelled. As SEM is computationally expensive, using high resolution DEM would generate higher number of spectral elements, which would make SEM more expensive in terms of memory storage and computation time. By making the resolution coarser, this issue was solved. But, in general, a coarser DEM produces less realistic results as compared to the finer DEMs. So a trade-off was required where the model provide realistic results even if the DEM resolution was low. Khan et al., (2015) have investigated the effect of DEM resolution in 3D modelling of seismic response through using ASTER DEM in various resolutions (by resampling the original 30 m resolution). Their study depicts that any DEM resolution coarser than 270 m produce less accurate results. Moreover, in another study, it is found that SRTM DEMs is more consistent with elevation and morphometric properties than ASTER DEMs (Shafique et al. 2011). So, selection of 270 m SRTM DEM was a reasonable choice keeping in mind the limitation of available computational facilities.

For creation of the free surface topography, the value of XYZ (Easting, Northing and Elevation) was required. These values were extracted from SRTM DEM. To keep consistency with the DEM resolution, the element size at the top surface of the mesh was also fixed at 270m.

In this study, a polynomial degree $N = 4$ was used to sample the wave field, which means each spectral element consists 125 Gauss–Legendre–Lobatto (GLL) points as shown in Figure 4-3. In order to reduce the computational time and cost, the total number of elements in the mesh was reduced by applying one mesh tripling to allocate finer element near the surface, and larger element at the bottom. However, it was ensured that the condition, as mentioned in Equation 4.9, for determining the element size was not violated by tripling. Mesh refinement (if required) was also done to make sure that there was no distorted element near the topography surface.

The mesh was constructed by using hexahedral mesher software CUBIT 13.0. This software toolkit is used for creation of finite element meshes (Sandia, 2016). The mesh developed under this research was a homogeneous half-space type which was basically a single block consists of elastic materials.

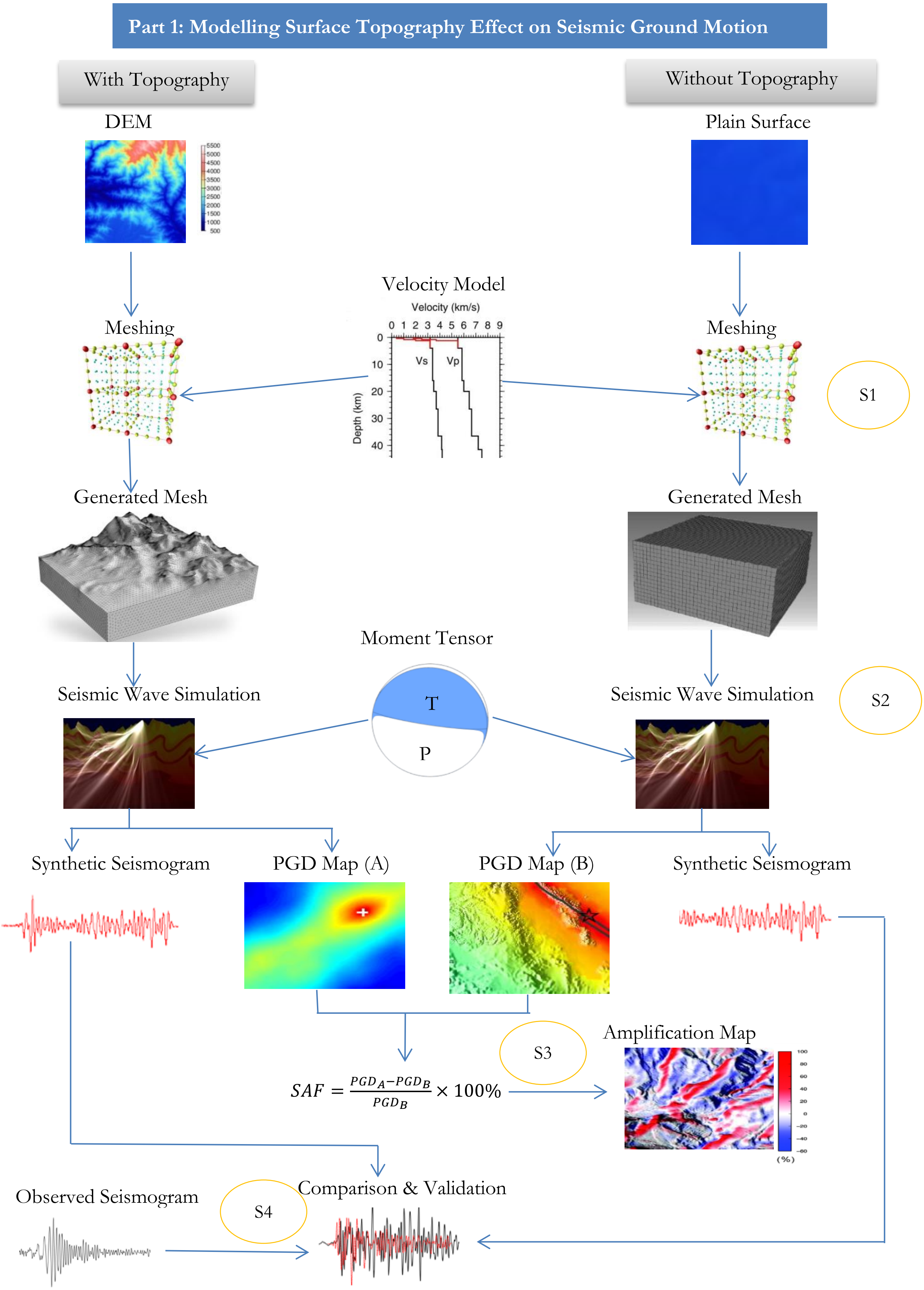

[a] : Methodological flowchart for modelling ground motion (Part-1) (stage S1 to S4)

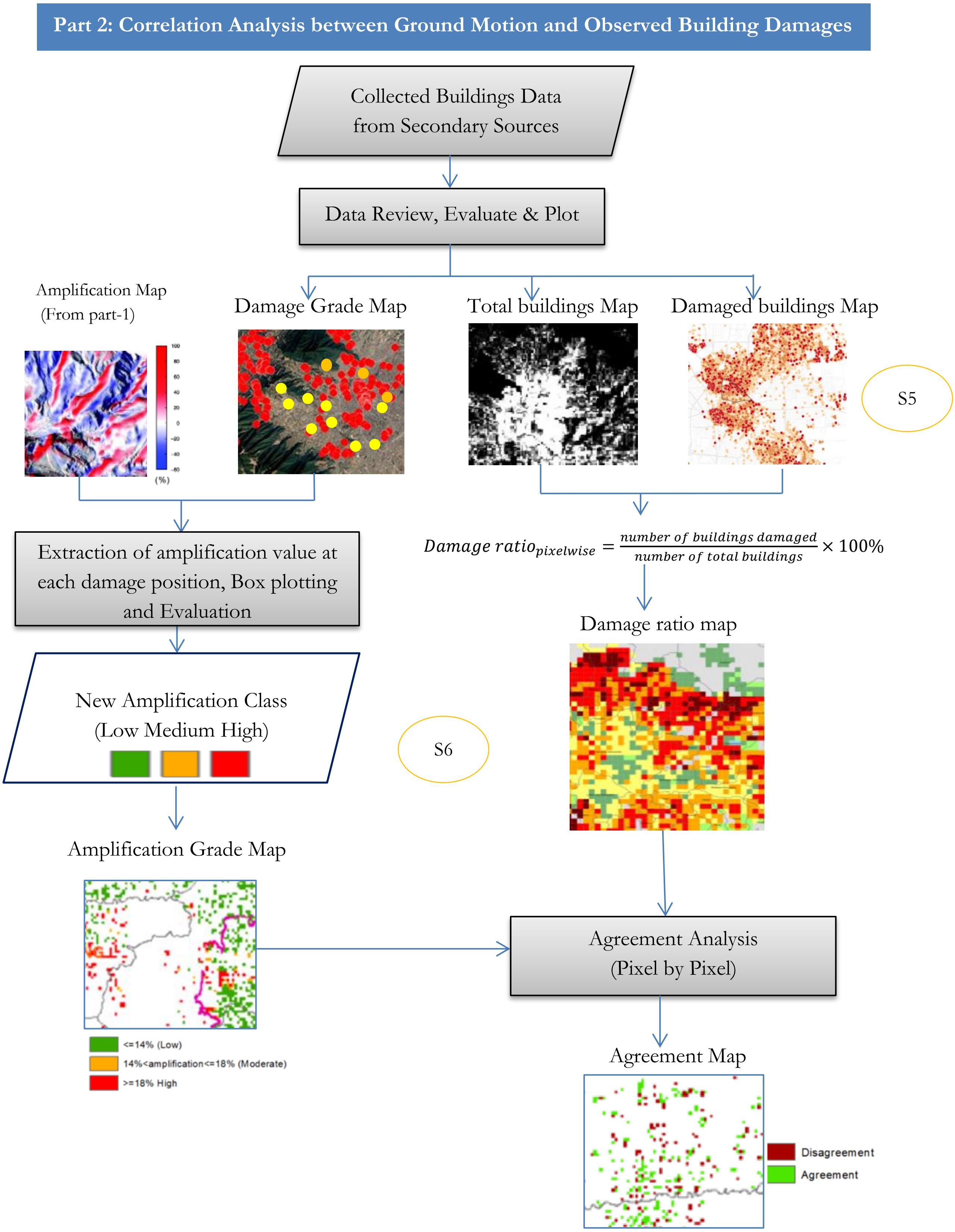

[b]: Methodological flowchart for correlation analysis (Part-2) (Stage S5 to S6)

Figure 4-4: Methodological flow chart for the study

4.3.2. Stage 2: Simulation of Seismic Wave Propagation

At this stage, the constructed mesh was exported into a SPECFEM3D Cartesian file format. SPECFEM3D is an open source code developed for simulation of full elastic seismic wave propagation based on the principles of SEM (CIG, 2016). The earthquake point source used for simulation of the Nepal Mw 7.8 earthquake was the Centroid Moment Tensor (CMT). The moment tensor is the mathematical model of the fault movement, which depends on the amount of seismic energy released by the source and the orientation of the fault plane. (USGS, 2016a). The CMT is the centre of the earthquake energy distribution which is defined by six moment tensor, the coordinates (i.e. location), the depth and centroid time (Ekström et al., 2012). In other words, CMT is the location with dominant moment release. The CMT data is freely available in the website http://www.globalcmt.org/. The CMT solution for the 2015 Nepal mainshock is provided in Annex –A1. Before starting simulation, each element was defined with material properties (velocity of P-wave (Vp) and S-wave (Vs), density of the material and attenuation). A constant wave speed of Vp and Vs (Vs=3370 m/s, Vp=5850 m/s) and density (3280 kg/m3) were assigned in the mesh model. The Vs and Vp were selected based on the average value of the velocities used or modelled by different studies performed on Nepal or Himalayan region. (e.g., Galetzka et al., 2015; Ichiyanagi et al., 2016; Koketsu et al., 2016; Monsalve et al., 2006). The Vp/Vs ratio (1.735) was consistent with the value used in some studies (e.g., Adhikari et al., 2015; Mahesh et al., 2013; Monsalve et al., 2006). Because of the lack of information, the density value was set at 3280 kg/m3 based on the empirical formula $\rho = \mathrm{Vp}/3 + 1280$, (Stidham et al., 2001). No attenuation was assumed in the bedrock. The locations of all seismographs/accelerometers installed in the Kathmandu valley were also defined by latitude, longitude, elevation and burial depth.

During simulation, the length of each time step was set based on Equation 4.10. Moreover, the number of time steps was set to fix the duration of simulation (i.e., total simulation time=length of each time step $\times$ number of time steps). At first, the simulation was done for the mesh considering realistic topography of the study site. Then another simulation was carried out for the mesh without real topography (i.e. assuming that the surface of the study area is perfectly flat). The simulation results were used to produce ground shaking map which is presented in the next stage.

To identify the changing pattern of ground shaking as a result of earthquake occurrence at different locations inside the study area, a total of five simulations were done by placing the CMT source in five different locations along the fault rupture line that passed through the study area. The points were chosen from the finite fault model developed by U.S. Geological Survey, (2016a). Figure 4-5 shows the USGS finite fault model and the placement of CMT at five different positions (denoted by P0 to P4). All five positions were chosen on the fault rupture line. The simulation conducted on point P0 was the original CMT position of the Nepal Earthquake. So, the results obtained from this point were used for analysing relationship between amplification and damage. The sub-fault points 2 and 6 were also considered for simulation (P3 and P4). However, the third largest sub-fault point 3 was just outside of the study area. So, a point (P1) was chosen at the corner of the study area, so that it became close to the point 3. As point 1 was close to the Centroid CMT, this was not considered for simulation. In between P0 and P1, a point P2 was chosen by visual interpretation of Google earth and SRTM DEM, where the surface topography between the point (P2) and the valley were not very rugged as compared to the other points. This point was selected to see the PGD amplification under the absence of significant topography between the source and the site. Moreover, the results obtained from P2 and P0 simulation could help to predict the seismic amplification if simulation would perform on sub-fault point 1.

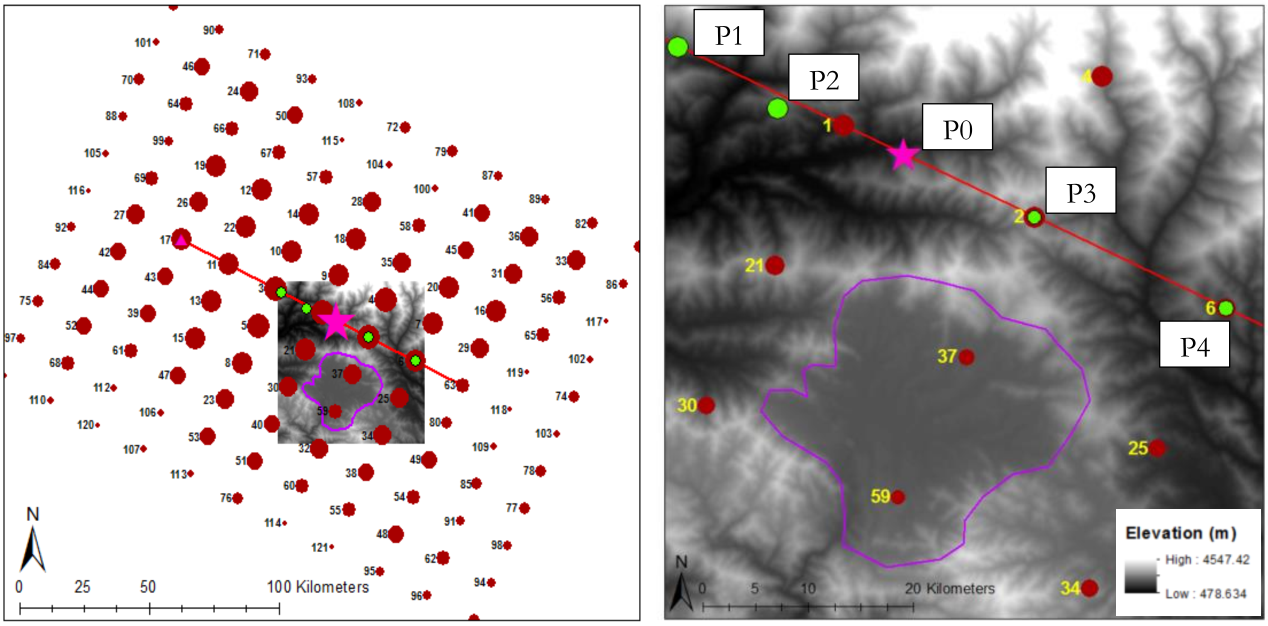

Figure 4-5: USGS Finite-Fault Model and Position of CMT. The left figure shows the whole fault plane of Nepal Earthquake. The approximate fault rupture line is shown by red straight line. Each red circle represents the centre of each sub-fault. The size of the circle represents the relative amount of released energy. The circles are also numbered by 1 to 121 according to the amount of released energy from the highest to the lowest. The study area as seen in the fault plane is zoomed in the right figure. The pink star represents the original CMT position. The four green circles represent the positions where the CMT source is placed to identify the radiation pattern of seismic energy in each scenario. These five CMT points are numbered by P0 to P4.

4.3.3. Stage 3: Preparation of Amplification Map

Under this study, the analysis was made based on Peak Ground Displacement (PGD) because PGD are mostly related to lower frequency component of earthquake (Kramer, 1996) and at the same time, the SEM technique is efficient for simulating low frequency earthquake ground motion (Dhanya et al., 2016).

After the simulation, the value of PGD and the synthetic seismogram were generated in ASCII format which was plotted by using Generic Mapping Tools (GMT) and Seismic Analysis Code (SAC) software.

At this stage, the ground motion maps in both cases (with and without topography) were used to create seismic amplification map by using the following formula:

$$\mathrm{SAF} = \frac{\mathrm{PGD_A} - \mathrm{PGD_B}}{\mathrm{PGD_B}} \times 100\% \quad \text{(Chaljub, 2006; Lee et al., 2008)}$$

Where, SAF=Seismic amplification factor, $\mathrm{PGD_A}$ and $\mathrm{PGD_B}$= Peak ground displacement with topography and without topography respectively.

4.3.4. Stage 4: Comparison between observed seismogram vs. synthetic seismogram

From the website of Strong Motion Center (http://www.strongmotioncenter.org/) and Hokkaido University (http://eprints.lib.hokudai.ac.jp), the raw data of actual seismogram was collected for the stations installed in the study area. Similarly, after getting the synthetic seismogram, it was convolved, at first, with the half-duration specified in CMT solution. Then, both of the seismograms were resampled to a common sampling rate (1 sample per second). Next, the same filtering was applied and the same time-window (0-60 seconds) was chosen. After that, a comparison was made between the synthetic and observed seismograms to identify the level of agreement between these two seismograms.

4.3.5. Stage 5: Preparation of Damage Map

The research planned to collect secondary damage data from different organizations which were involved in damage mapping after the earthquake. At first, some of the organizations and personnel were contacted by e-mail. However, it was found difficult to get the data directly from the organizations or office personnel. So, an extensive internet search was conducted to collect the damage data whatever was freely available. After detail search, it was found that four organizations UNITAR (http://www.unitar.org), Copernicus (http://www.copernicus.eu/), National Geospatial Intelligence Agency (http://nepal.nga. opendata.arcgis.com/), NASA ARIA (http://aria.jpl.nasa.gov/) have shared part or full of their data in one common platform Humanitarian Data Exchange (https://data.humdata.org/) . However, the data of the total buildings of Nepal was not found from any of those websites or any other national and international organizations. Thereby, it was collected from the open street map. The collected data was evaluated thoroughly to determine whether the quality of data is sufficient enough to meet the research requirements. For research purposes, it would be excellent if at least four types of information about building damages were found. These are (i) locations of building damages (ii) damage level of individual buildings as per European Macroseismic Scale-1998 (EMS-98) (iii) Building type (e.g. Masonry, Cement mortar, reinforced concrete, unreinforced masonry etc.) and (iv) Building height or number of floors. Noted that the EMS-98 scale is an widely used damage classification scheme, which defines five damage grades (grades 1 to 5) for masonry and reinforced buildings indicating gradual increasing of ground shaking in accordance with the increase of damage grade (Figure 4-6).

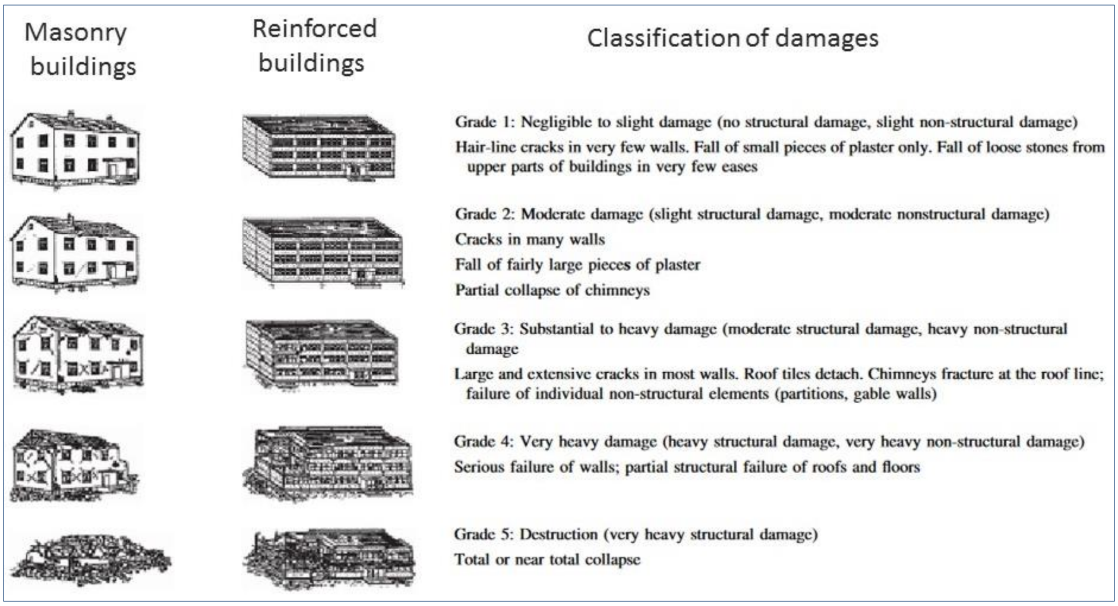

Figure 4-6: Classification of damage to masonry and reinforced buildings according to EMS-1998 scale [modified from Ohsumi et al., (2016) and Rezaeian & Gruen, (2011)]

While checking the quality and comprehensiveness of the collected damage data, significant limitations were found. The building damages were not classified based on building type/height and urban/rural context and the damage grade classification, in most of the cases, did not conform to EMS-98 scale. This was due to the rapid and non-technical damage assessment conducted by the organizations (World Bank Group, 2015).

Initially, all organizations did damage mapping individually but after that the data were combined by them. For example, UNITAR and Copernicus consolidated their data together with three damage grades (Destroyed, Severe damage and Moderate Damage). Similarly, the damage data of NGA and NASA/ARIA were combined with four damage grade (Destroyed, Severe damage, Moderate Damage and Possible damage). The research used this combined data assuming that all the disagreement existed in individual mapping was considered and solved during integration of the data. However, in the combined data, the explanation/criteria of different damage grades were not provided. Except Copernicus, no organization provided information on "no damage" or "unaffected" status of buildings in the map.

For total buildings data, the open street map shows polygons each of which indicates one building. The map does not have any information about the building type and height. So, the research only relied on the count of polygons to get the information on the total number of buildings.

A Table is provided in Annex-A2 for getting more insights into the data quality and completeness of the collected data.

Damage data was also checked to examine the overlapping or duplication of data. Some areas were found where multiple organizations worked for damage mapping. In the overlapped areas, firstly, it was checked whether same building was assigned different damage grade or not by the multiple agencies. If assigned grade was found different, NGA's data was considered for the analysis because they were mainly focused on Kathmandu valley and their data was also used by NASA/ARIA for validating their prepared damage map. Secondly, if the agencies mapped different buildings in the overlapped area, all data was counted and combined.

The damage map was prepared by using ArcGIS software. Noted, all the organizations prepared the damage map by satellite image analysis. Specially, UNOSAT and Copernicus used very high resolution images (World view 1 & 3, GeoEye-1, Pleiades 0.5m). However, even for very high resolution satellite images, mapping the lighter damage state (for example, grade 1-3 of EMS scale) is very challenging (Dell'Acqua & Gamba, 2012; Kerle, 2010). Moreover, all organizations had their own damage classification scheme and did not explain the criteria for being categorized the buildings into a particular damage level. Therefore, for simplicity, the present study categorized all damage data into three classes (No Damage, Moderate to Severe Damages and Destroyed). On the other hand, no standard classification of amplification value was found during the literature search. However, based on the review of Lee et al., (2009) and Lee et al., (2008), we preliminary defined four classes of amplification in which <=0.1 was considered was low amplification and after that, 0.1 to <=0.4, 0.4 to <=0.7 and > 0.7 was defined as moderate, high and very high amplification respectively.

4.3.6. Stage 6: Amplification vs. Damage Analysis

<u>Individual Building Level</u>

At this stage, the analysis was done at individual building level. The damage map was spatially overlaid on PGD amplification map to extract the amplification value at each building position. Then statistical analysis was performed to identify the pattern distribution of amplification value at each damage classes (i.e., No Damage, Moderate to Severe Damages and Destroyed). The distributions were shown by Box plot. As general rule of descriptive statistics, the 25th percentile to 75th percentile value displayed in box plot were considered as the representative amplification value for a particular damage class. Based on the analysis, a new classification scheme of amplification was proposed, which was used for correlation analysis at aggregate (pixel) level. This was done because we did not find any literature where PGD amplification value was clearly categorized. So, the research also tried to develop a simple classification scheme in order to carry out the correlation analysis at aggregate level.

Aggregate (Pixel) Level

In this stage, analysis was done by using the concept of damage ratio (Wu et al., 2012). Here, the total number of damaged buildings in each grid cell was divided by the total number of the buildings (Damage plus no damage) located in the same cell. To do that, the pixel size of the total damage map and total buildings map were fixed as same as ground motion amplification map (i.e., 270 m). Note that, the total damage map was prepared by counting all damaged building, irrespective of the different damage grade, located in each pixel. Then the damage ratio was grouped into four classes in the order of low, medium, high and very high as used by Wu et al., (2012). Moreover, based on the new classification scheme obtained from the analysis at individual building level, an amplification map of same pixel size was also prepared. Then, an agreement analysis was performed in binary way (0= No agreement, 1= Agreement) to determine the overall agreement between the amplification map and damage ratio map.

5. RESULTS AND DISCUSSION

In this chapter, all results from the methods applied under this research are reported. Each result is followed by its own discussion. At first, focus is given on evaluating the surface topography effects on seismic ground shaking in order to achieve the first specific objective and answer the corresponding research question RQ-1 to RQ-3 as mentioned in Chapter 1 (section 1.3). After that, the relationship between the ground shaking and building damages is presented and discussed to provide answers of the research questions RQ-4 to RQ-5 with a view to achieve the second specific objective.

5.1. Surface Topography Effects on Seismic Ground Motion

5.1.1. Mesh Implementation and Simulation Parameter

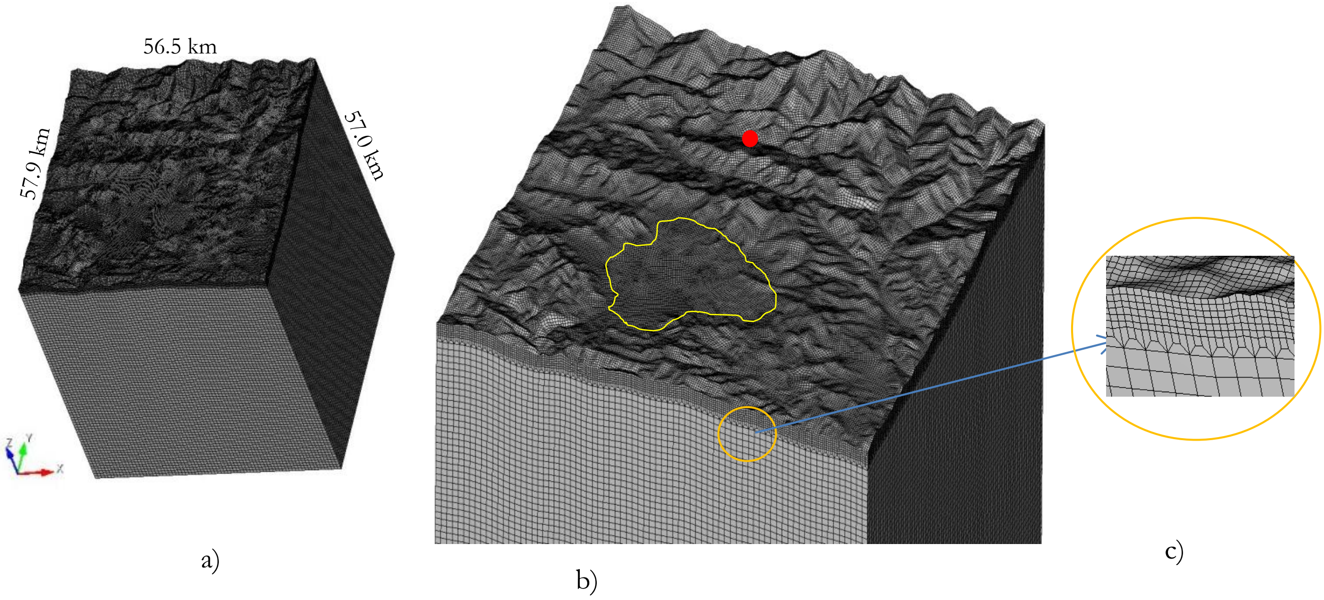

Figure 5-1: Spectral Element Mesh (a) The mesh for Kathmandu valley and surrounding areas. (b) The enlarged version of the realistic surface topography at the top of the model. The yellow outline shows the approximate boundary of the valley. The small red circle is the CMT location. (c) One tripling layer is used in the model

The constructed mesh incorporating realistic surface topography is shown in Figure 5-1. The mesh without topography is shown in Annex A3, where a perfectly flat surface, in place of realistic surface, is placed on top of it. The mesh covers the area of 56.5 km × 57.9 km and the depth is from +4.5 km to -57.0 km. The outline of Kathmandu valley and highly built up areas are also shown in the mesh. In both meshes, one mesh tripling was used, which increased the element size by three times immediately below the tripling layer.

The mesh properties are shown in Table 5-1 for both meshes. For mesh with topography, the total number of elements of the mesh was 0.85 million which was slightly higher than that of mesh without topography. The mean size of the element varied from 148 m at the surface to 1112 m at the bottom of the mesh whereas for mesh without topography, the mean size was 223 m and 735 m respectively. For both meshes, the average Gauss-Lobatto-Legendre (GLL) distance in the horizontal direction at the surface was 60~61 m which was small enough to resolve 9 arc seconds grid spacing DEM data. Because of having a higher number of elements, the mesh with topography consisted of a higher number of grid points (56.3 million) as compared to the mesh without topography (56.2 million). The mesh was designed to solve three components (XYZ) of displacement at each grid point. As a result, the number of degree of freedom (DOF) was three times higher than the number of grid points.

From the Table 5-1, it is also found that the length of each time step (Δt) for the mesh with topography and the mesh without topography are 0.0005 seconds and 0.0025 seconds respectively. Setting the value of time step is very important for the stability of the simulation. In addition, this parameter also determine the total time required for the available facilities (in this case, 16 processors) to complete the simulation (in this case, 60 seconds). The maximum Δt was determined from the Equation 4.10. Actually, the value of Δt depend on the minimum size of the element (more specifically, minimum GLL distance) and maximum velocity of the seismic wave. So, the presence of a very small element in mesh makes Δt very small and therefore, make the simulation very expensive in terms of computational time. Generally, if the chosen Δt is lower than the maximum Δt the simulations become stable, otherwise the simulation is not performed and blown up. However, if the mesh quality is very good, running the simulation is possible even if the selected Δt is slightly higher than the maximum Δt (Komatitsch et al., 2015). Fortunately, during simulation, the SPECFEM3D solver automatically calculated the Δt based on the equation 4.10 and suggested the maximum Δt for ensuring stability of the simulation (Komatitsch et al., 2015). In this study, the maximum Δt suggested by the solver was 0.00084 seconds and 0.0027 seconds for the mesh with topography and the mesh without topography respectively. As, the smallest GLL distance for mesh with topography is smaller than that of the mesh without topography, the suggested maximum Δt was also smaller for mesh with topography as compared to that of mesh without topography. Here, a lower Δt value (0.0005 seconds and 0.0025 seconds respectively) was used for simulation. The relevant part of the output file generated by the SPECFEM3D software after simulation is provided in Annex-A4.

Table 5-1: Mesh properties for simulation of seismic wave

Model Parameters and Simulation process	**Mesh (with Topography)**	**Mesh (without topography)**
Dimension of the mesh (km3)	56.5×57.9 × 57	56.5×57.9 × 57
Total number of elements (million)	0.854	0.842
Maximum element size (m)	1112.36	735.60
Minimum element size (m)	148.38	223.12
Maximum GLL distance (m)	503.21	244.01
Minimum GLL distance (m)	9.81	31.54
Average GLL distance at surface (m)	61.25	60.5
Number of grid points (million)	56.3	55.2
Number of degree of freedom (million)	168.9	165.6
Total MPI process (CPUs)	16	16
Simulation time (seconds)	60	60
Number of time steps	120000	24000
Length of each time step (Δt) (second)	0.0005	0.0025
Time taken for simulation (hours:minutes)	119:51	26:00

As can be seen from Figure 5-2 and Figure 5-3, for mesh with topography, the size of the elements is mainly distributed between the range of 209 m to 281 m and 667 m to 787 m which contains 40 % and 42% of all element sizes respectively. For mesh without topography, the element size was mainly limited to either 242 m or 729 m. These two sizes together cover 91% of total elements. These changes of the element size were due to the use of the mesh tripling layer. Because of having less variation of mean element size (mainly two sizes) in the whole volume, the quality of mesh considering without topography was indicated to be better than the mesh with topography.

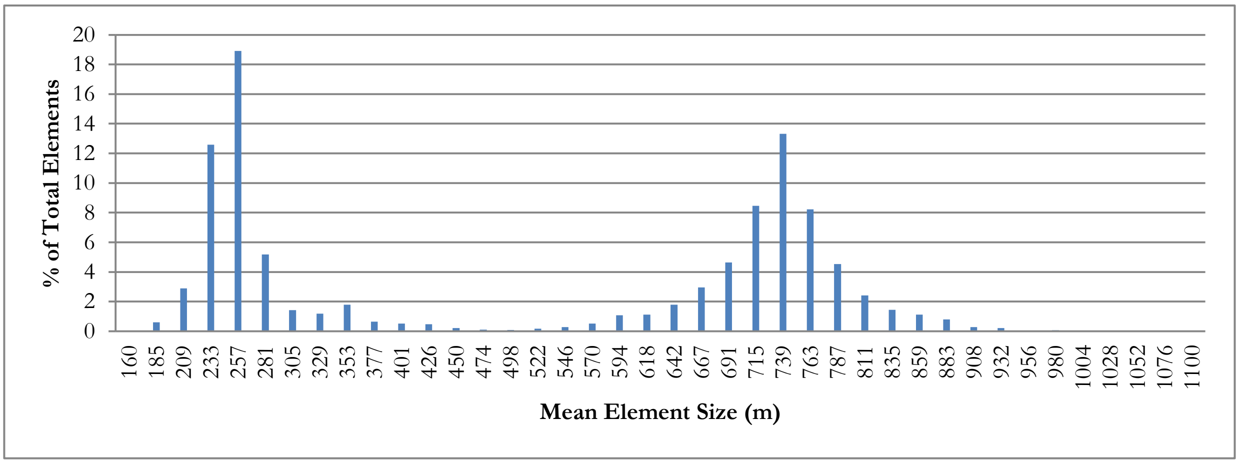

Figure 5-2 : Distribution of element size for mesh with topography

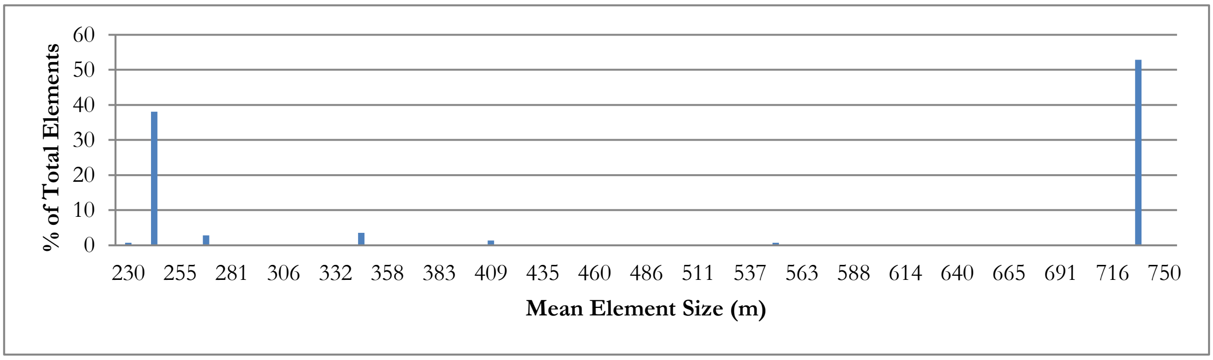

Figure 5-3 : Distribution of element size for mesh without topography

Regarding the quality of the mesh, the maximum skewness of the mesh with topography was 0.79 whereas for mesh without topography, it was 0.64. This means that the quality of mesh without topography was better than the mesh with topography. In the mesh without topography, the top surface was perfectly flat. So, the SEM mesh easily honoured the surface without causing strong deformations to its elements. In case of the realistic surface topography especially for highly rugged terrain areas like Nepal, there was a very high change of the elements to be distorted to a significance level during meshing. From the mesh with topography, it was seen that a total of 16 elements are distorted to the level of 0.79. On the other hand, 8394 elements were suffered with skewness 0.64 for mesh without topography. In both cases, the skewness was below the threshold of 0.8 (Casarotti et al., 2008) which indicate that the quality of both meshes was sufficient enough for simulation of seismic wave propagation accurately. For detail information about the skewness of the meshes, the readers are referred to the Table provided in the Annex –A5.

Note that the skewness determines the level of distortion in each element of a mesh. Keeping skewness value below a certain limit is very important because a large distortion may cause numerical error during simulation of the seismic wave. In ideal case, there should be no distortion in elements. This means, the six sides of a hexahedral element should be in full contact of the sides of other neighbouring elements. In other words, the angle between the edges of the faces of every element of a mesh should be perfectly 90 degree. If it deviates from the 90 degree angle, the element is defined as distorted. A skewness value of '0' means no deviation from the right angle position (i.e. perfect hexahedral element) and '1' means maximum deviation (i.e. very bad element). In reality, it is not always possible to keep the skewness value at minimum level especially during meshing highly uneven mountainous earth surface like Nepal. In general, a skewness below <0.8 is considered as acceptable (Casarotti et al., 2008).

Though the skewness of both meshes was below the threshold, it was still high in the case of the mesh with topography as some authors considered the maximum skewness to be 0.75 (Komatitsch et al., 2015). This could be possible if mesh tripling was not used. A large number of the elements having skewness above 0.75 are located in the mesh tripling layer. The tripling layer was basically a transition layer where three elements were stitched to one element. As a result, the elements in this layer contained higher skewness value. In fact, that layer was used to increase the element size with depth in keeping with the corresponding increases of wave velocity so that the ratio of wave velocity to element size does not vary over the whole mesh. In this research, there was no need to apply mesh tripling as uniform velocity of seismic wave was used throughout the model. In spite of this, the mesh tripling layer was used so that the total number of element could not be very high for the available computational facilities (i.e., 16 processors); otherwise the computational time would be very expensive. Komatitsch et al., (2004) used 144 processors for simulations where the element size at the surface was 332 m and total number of elements was 0.67 million. It took 6.5 hours for 180 seconds simulation. Lee et al., (2008) decomposed study area (101 km x 87 km x 100 km) into 324 slices (i.e. 324 highly configured processors) whereas the average grid resolution at the surface was 112 m. The total number of elements was 45 million. The system consumed 9.5 hours for 14 seconds simulation. So, despite of the uniform seismic wave velocity used in this research, the use of mesh tripling without compromising the overall quality of the mesh was reasonable.

According to the condition mentioned in Equation 4.9, the mesh with topography was able to resolve seismic waves with a shortest period of 0.57 sec (i.e. up to 1.75 Hz frequency). The ability of the mesh without topography to resolve seismic wave was higher than the mesh with topography. That mesh was capable to simulate the seismic wave with a shortest period of 0.27 sec (i.e., up to 3.67 Hz frequency). So, the configurations of both meshes were capable to resolve the frequencies of the seismic waves of the Nepal earthquake which varied from 0.05 to 2.0 Hz (mostly dominated by ~1.0 Hz) (Avouac et al., 2015; Fan & Shearer, 2015; Galetzka et al., 2015; Yagi & Okuwaki, 2015).

During simulation, both meshes were decomposed into 16 slices which were allocated over 16 processors based upon the message passing interface (MPI). For mesh with topography, the number of time steps chosen was 120,000 and the length of each time step was set 0.0005 sec, that means, total 60 seconds simulation. It took around 119 hr 51 minutes to complete the simulation. For mesh without topography, it required approximately five times less CPU time for completing 60 seconds simulation.

5.1.2. Peak Ground Shaking Distribution

The peak ground displacement (PGD) map after simulation of seismic wave is shown in Figure 5-4. As can be seen from (a) and (b), the seismic energy is predominantly propagated in east–west direction. It mainly spread into the outside part of the valley but for model with topography significant reflection and scattering of seismic wave is observed. The central part of the valley also receives some part of reflected and scattered seismic energy.

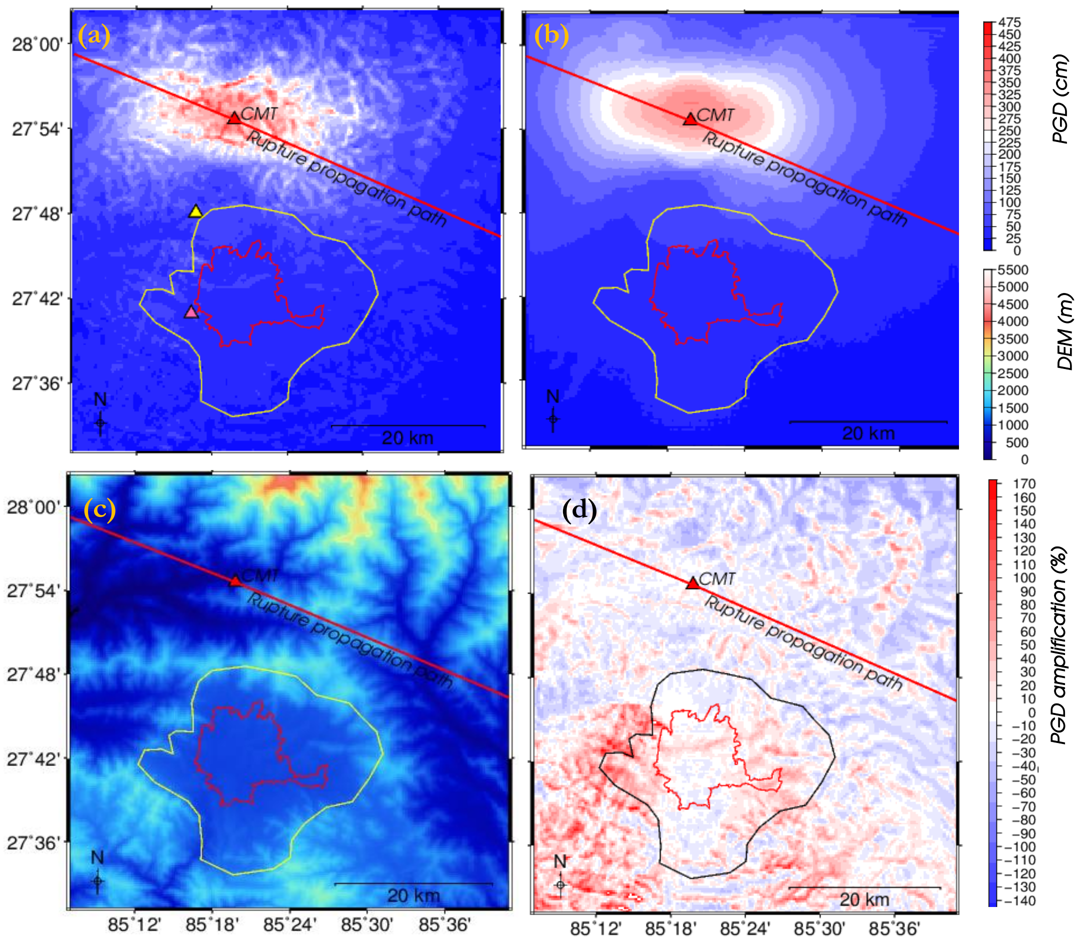

Figure 5-4 : Peak Ground Displacement (PGD) Model (a) PGD for model with topography, (b) PGD for model without topography, (c) Surface topography (Digital Elevation Model), (d) PGD amplification (%) map in which the white and blue colour respectively shows no or very low amplification and de-amplification. The red colour indicates high amplification. The CMT is shown by black-outlined red triangle. The rupture propagation path, as shown by red straight line, passed through the north of the Kathmandu valley. The red line also indicates the path of dominant release of seismic energy. The outline of the whole valley is illustrated by yellow line for Figure (a)-(c) and by black line for Figure (d). Inside the valley, the area enclosed by red line is the highly built-up and populous areas which mainly composed of Kathmandu Metropolitan, Lalitpur Sub-metropolitan and Bhaktapur Municipality. Except this core area, the other parts of the valley are mainly the sub-urban and rural areas. The yellow and pink triangle in Figure (a) correspondingly indicates the GPS and accelerometer station installed in the rock site.

The displacement value in the Kathmandu valley varied from 0.5 meter to 2.0 meter under realistic surface topography condition (Figure 5-4a). The maximum PGD value (displacement norm) was observed at a point close to the CMT, which was ~4.75 meter for model with topography and ~4.0 meter for model without topography (Figure 5-4a-b). This value was significantly high as compared to other studies (e.g., Grandin et al., 2015; Greicius, 2015; Lindsey et al., 2015; Liu et al., 2016; McKinney, 2015; Schütz, 2015) where InSAR technique and/or GPS data were used and the vertical and horizontal displacements close to the CMT location were found 1.0 ~ 1.6 meter and 2.0 meter respectively. This was because the model used the centroid source (i.e. point source representation of earthquake moment distribution) which means that the whole seismic energy was assumed to be released from one single CMT point. As a result, the ground motion was highest at the source point and decreased with increasing distance from the source. Yenier & Atkinson, (2014) mentioned this limitation of using point source as ‘distance saturation effects’. However, Takai et al., (2016) found maximum 2.2 meter and 1.5 meter displacement norm in KKN4 GPS station and KTP Accelerometer station (shown by yellow and pink triangle in Figure 5-4a, which was close to the modelled value (1.92 meter in KKN4 and 1.43 meter in KTP). In addition, the present research followed the method used by Lee et al., (2009) and Chaljub, (2006) for generating the seismic amplification map, which considers the relative change of values of PGD both for with and without topography and therefore, the effect of higher value was cancelled out for the amplification analysis.

The PGD amplification map (d) depicts that except one narrow channel of higher amplification (30% - 40%) orienting east-west direction in the central areas, most of the areas of the central part of the valley is amplified by a factor of maximum 10%. However, the east and west margin of the valley is amplified up to 170%. So in summary, the valley shows little to no amplification (at places even de-amplification) and the absolute displacement map (Figure 5-4a) clearly indicates that the displacement are lower in the valley than in the surrounding areas, apparently creating a shadow zone of energy due to two mountains ridges between the source and the valley.

To assess the effect of the two ridges on the seismic wave propagation and to judge if the location and topography were indeed controlling this de-amplification effect for the valley, the CMT location was moved to four other possible locations along the same fault. The simulation results obtained from these four hypothetical points (P1 to P4) are shown in Figure 5-5 in which the role of surface topography is clearly seen. In almost all cases, the central urbanized areas of Kathmandu valley experienced higher shaking if the maximum energy was released in upstream points P1 and P2. In both of these cases, more than two third of the valley area would be largely amplified up to ~130%. However, the upper half of the valley would be out of danger while the lower half would suffer with even more ground shaking (around 180%) if the CMT would located on a downstream point of the rupture propagation path (point P3). A very different pattern of amplification was observed for point 4. Here, the whole mountains/hills surrounding the valley would be largely amplified and let the upper half of the central urban areas to be amplified by around 20%. In this case, the lower half of the valley would not feel any significant ground shaking. The PGD maps considering with and without topography for all four scenarios are provided in Annex-A6.

The results give an indication about the role of surface topography behind limited ground shaking observed during the earthquake. Under the current earthquake setting (original CMT position), the surrounding surface topography prevented the seismic energy to enter into the central part of the valley. Similar results were found in Ma et al., (2007) where the San Gabriel Mountains shielded the Los Angeles Metropolitan areas from Mw 7.5 earthquake by significantly scattering seismic waves and reduced the peak ground velocity by 50%. From our results, the topography also significantly scattered the seismic waves, trapped energy in the topography and divert it to bypass the valley and thereby, reducing the ground motion in the valley centre. In this way, the surface topography created a shadow zone in the core urban areas. However, the bypassed seismic wave met with the local seismic wave in the Kathmandu valley periphery and continued to interact with the topography, which ultimately produced massive amplification along the east and west boundary of the valley. This possibly can explain why damage was more pronounced at the edge of the valley as compared to the centre of it as was observed by Hashash et al., (2015). In case of CMT position P1 and P2, the surface topography no longer plays a role of seismic shield. At position P4, it insulates a major part of the seismic energy propagated towards the valley. For P1 and P2, the reason behind high ground shaking observed in the whole valley was probably due to the scattering of body waves by the topography and therefore, propagated as surface wave towards the valley.

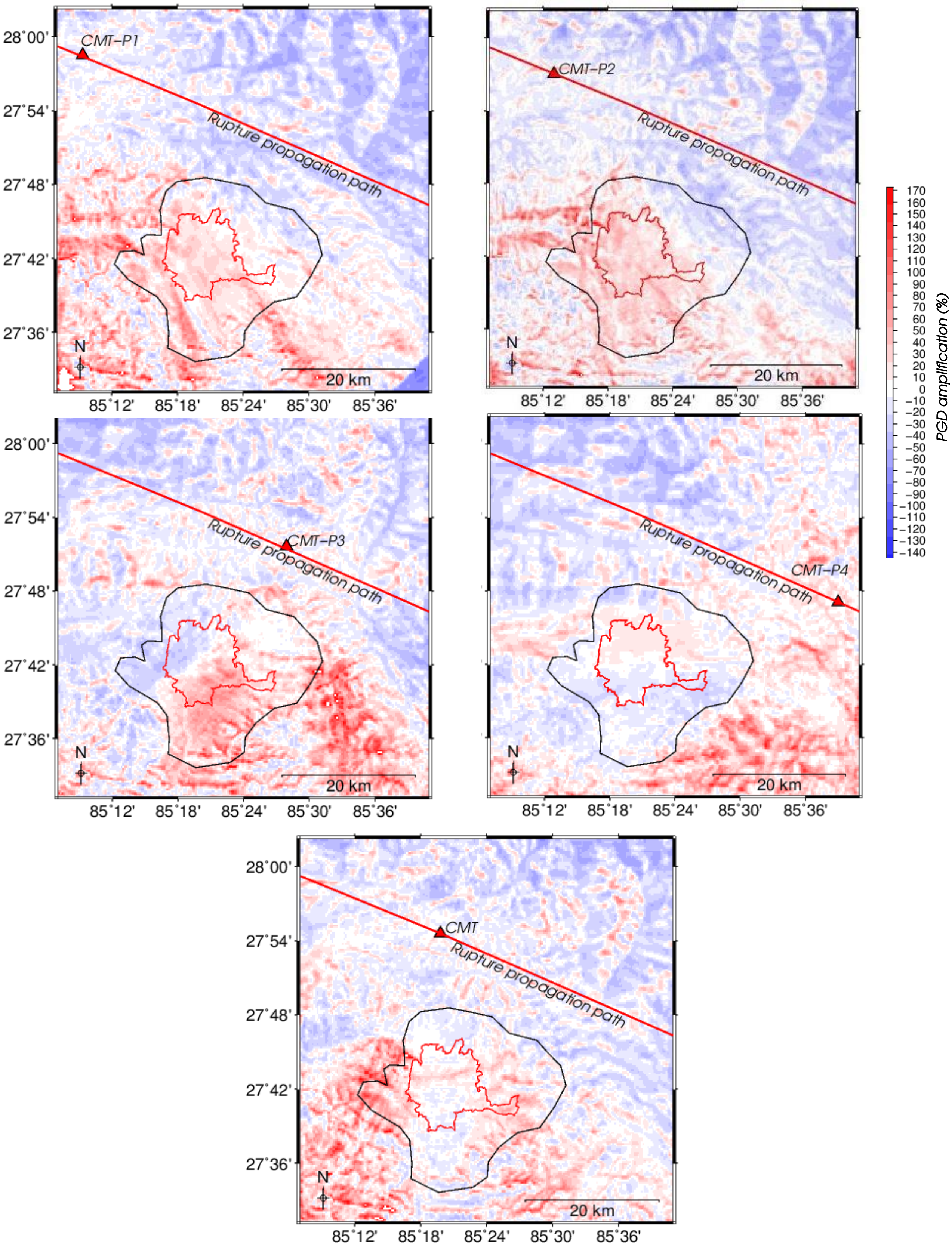

Figure 5-5: PGD amplification due to the shift of CMT to four different locations (P1 to P4) along the fault-rupture line. The PGD amplification map for original CMT position is also shown at the bottom for easy comparison with four hypothetical scenarios.

However, for P4, the mountains scattered the surface wave and directed the wave to propagate outside the valley. As a result, most of the valley would receive less energy. The role of topography for point P3 was found to be similar to that of the original CMT point. However, because of the position of CMT point, the scattering and reflection of seismic wave by the surface topography invite more ground shaking in the right half of the valley.

It was also observed that the seismic wave was amplified at ridges and de-amplified at the toe of the hills and mountains located specially in the upper part of the study area. This was also observed from past earthquake events (Hartzell et al., 1994; Lee et al., 2009). The sides of the mountains facing towards the CMT experience low or no amplification, whereas the opposite sides facing away from the earthquake source receive high amplification.

5.1.3. Displacement Wave Field with Time

The shake movie of X, Y and Z component of the displacement wave field of the 2015 Mw 7.8 Nepal Earthquake is displayed in Figure 5-6. The figure shows that the faster P-wave reaches the surface at around 2.1 seconds and continues to spread (e.g., 2.8 sec). At approximately 3.5 seconds, the slower but stronger S-wave is appeared at the surface. It is observed from the snapshot taken at 4.5 sec, the highly uneven terrain areas located to the north of the valley (especially the two mountain ridges) reflect and scatter large amount of seismic energy (surface wave) emanating after the appearance of S-wave and produce a complex wave fronts in the vicinity of the origin (i.e. CMT point). Specially, for two horizontal components, the middle part of the wave field propagating toward the valley are significantly distorted and become weaker (6.7 sec). The other part still has sufficient energy to vibrate the valley exterior significantly. However, at 6.7 seconds, the vertical component wave field experience constructive interference from the isolated waves generated from the reflection and scattering and therefore, the amount of seismic energy is increased (still less as compared to the energy released from the CMT point). At 6.7 sec, the P-wave propagated out of the valley (shown by black arrow) and at 10 sec, it is out from the study area. However, still the valley continues to shake at 10 sec because of the isolated reflected and refracted seismic wave produced from the scattering by the surrounding topography.

It is also observed that the P wave is not largely affected by the surface topography (2.8 sec and 3.5 sec) but the S wave is clearly affected by them (4.5 sec). From Z-component, it is clearly seen that the lower half land surface from the CMT point is uplifted (dominated by warm colour which mean upward displacement), whereas the upper half experience subsidence (dominated by blue colour which mean downward displacement). The changing pattern of ground displacement is similar to other studies conducted on the 2015 Nepal mainshock (e.g., Greicius, 2015; Malla, 2015; Schütz, 2015; USGS, 2015).

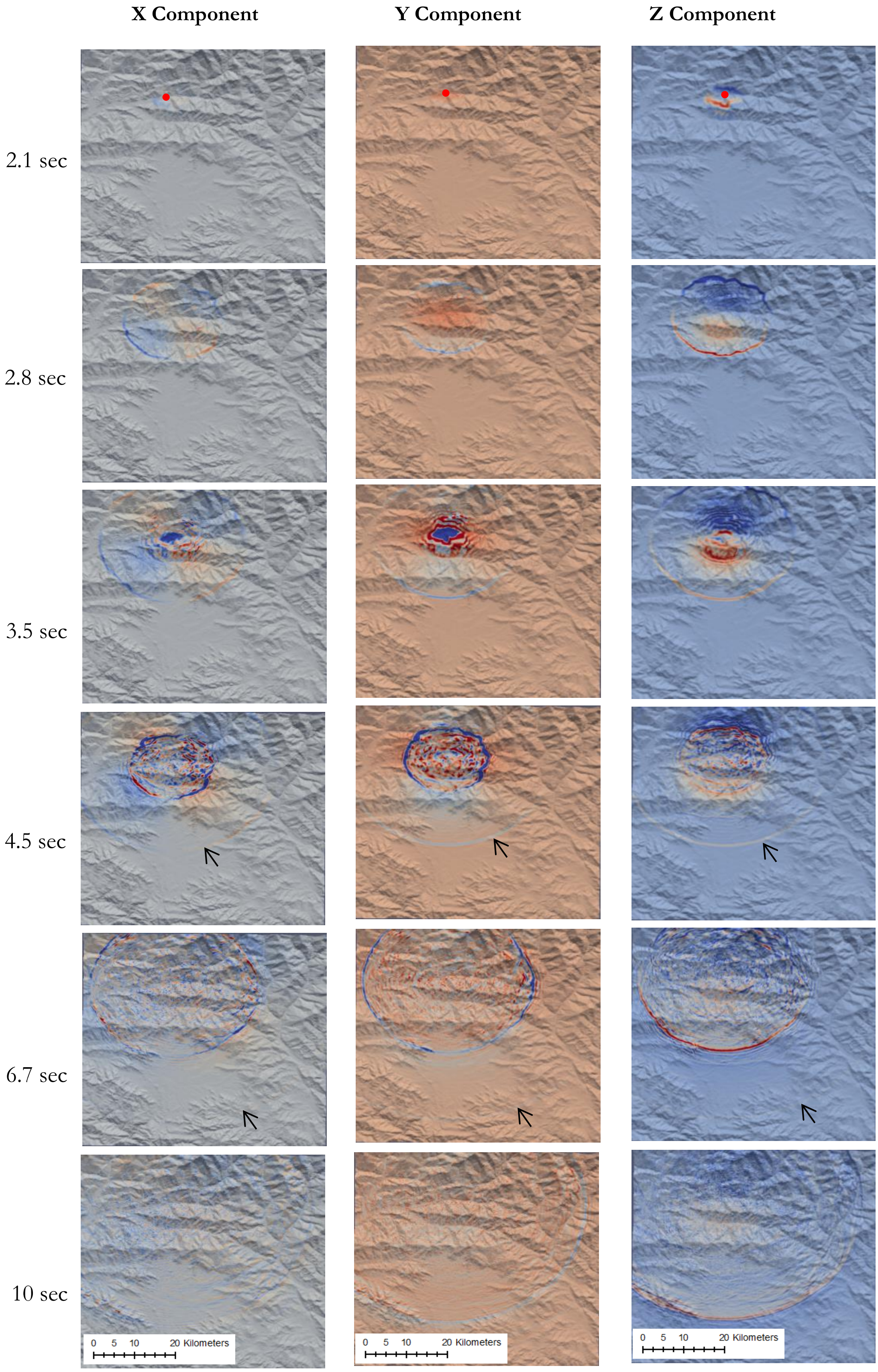

Figure 5-6 : Snapshots of displacement wave field for X, Y and Z component. Within each snapshot, warm colour (e.g., red) indicates positive displacement and cold colour (e.g., blue) indicates negative displacement. The wave fronts, especially the X and Y components, are significantly distorted and scattered by the topography. However, some constructive interference is seen for Z component at 6.7 seconds. The black arrows indicate P-wave field shown only for 4.5 and 6.7 seconds (it is clearly seen for 2.8 and 3.5 seconds). At 10 seconds, the P-wave propagated out of the study area. The CMT is shown by red dot in the first snapshot only.

5.1.4. Observed Vs. Synthetic Seismograms

The synthetic seismogram generated from the model was compared with the observed seismogram. The actual data recorded on KTP station (Kirtipur Municipality Office, Kirtipur) (Figure 5-7) located inside the valley were only considered for comparison because this station is installed on hard rock site. Only acceleration data of this site was found available on the website.

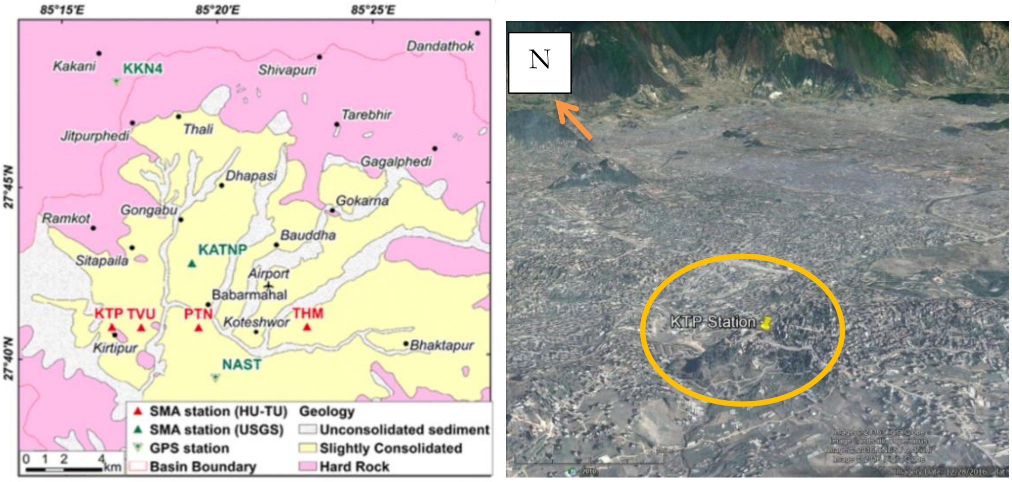

Figure 5-7 : Location of Accelerometer and GPS station installed inside the Kathmandu valley (Takai et al., 2016). (Left figure) The KTP, TVU, PTN, THM are installed by Hokkaido University and Tribhuvan University and KATNP by USGS. (Right figure): The location of KTP is shown in Google Earth Image.

Before comparison, both the observed and synthetic acceleration (cm/s^2) records were band pass filtered between 8 and 60 seconds and between 10 and 60 seconds. This was done because SEM synthetics are accurate at periods of ~8 seconds and longer (http://global.shakemovie.princeton.edu/science.jsp). The instrument response of the observed seismogram was not removed due to the unavailability of the response data of the sensor (Highly damped moving coil type accelerometer, Mistutoyo JEP-6A3-2).

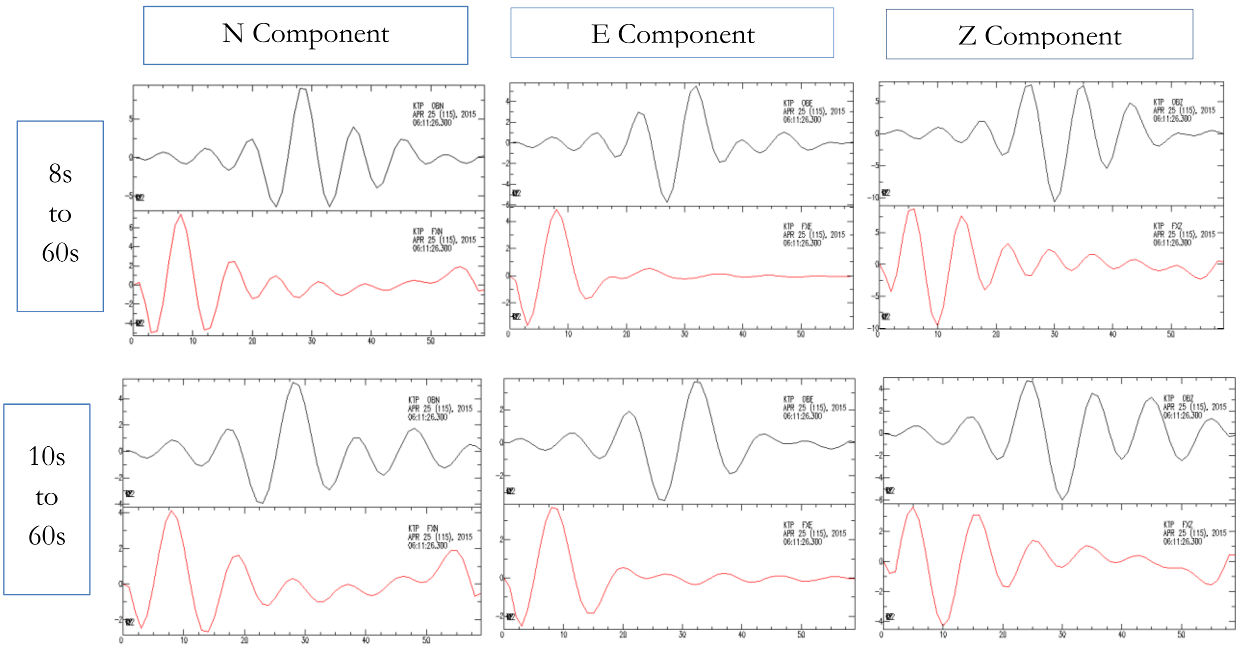

Figure 5-8 : Comparison between the observed (black line) and synthetic ground acceleration (red line) (cm/s^2). The first row of the figure shows the results of seismograms prepared by filtering the traces between 8 to 60 seconds. The second row is the results of 10 to 60s filtering. In each case, the three components (North, East and Up) are presented.

The results of the comparison between the observed seismograms and synthetic seismograms are presented in Figure 5-8 Overall, the results show a good agreement between the two seismograms regarding the pattern of amplitude of the acceleration waveform. The results obtained from 10 -60s filtering shows better agreement between the two graphs in terms of the value of the amplitude. However, the misfit of time and some disagreement of amplitude value between the two seismograms might be due to the value of P-wave and S-wave velocity used in the model. The model assumed a uniform velocity over the whole domain and considered the average value of the velocity found in different studies performed in Himalayan region (e.g., Galetzka et al., 2015; Ichiyanagi et al., 2016; Koketsu et al., 2016; Monsalve et al., 2006 ; U.S. Geological Survey, 2016a). Apparently the velocity model used in this study is faster leading to the earlier arrivals of seismic waves compared to the observed. The model also considered uniform material properties over the whole mesh block, which was not fully comparable with the realistic earth surface. According to Chaljub, (2006), a more realistic selection of S-wave velocity can improve the agreement level between the observed and synthetic seismograms.

However, the amplitude value of the N and Z component at the tail end (after 50 seconds) of the synthetic seismogram tended to go up. The possible reason is that the surface topography scattered and reflected the seismic wave and part of the reflected wave again started propagating back towards the station. The same effect was found in Lee et al., (2008) where the mountains significantly reflected the seismic energy and produced a complex wave propagation behaviour because of which at late phase, high PGA value was observed in the Taipei basin. The phenomenon is possibly not captured within the first 60 seconds of simulation. It might be clearer if the simulation time was increased more. But because of the lack of time, the study did not run the model again with extended simulation time.

5.2. Relation Between Seismic Amplification and Observed Buildings Damages

5.2.1. Damage Mapping

The damage map after combining all the data collected from secondary sources is shown in Figure 5-9. It is observed that a large part of the study area does not have any damage information. The information about whether this part was either not mapped or not affected was fully unclear from the collected data. So, the research excluded these areas from the analysis. However, two small areas were found where buildings were mapped as 'not affected' by Copernicus (shown by blue dots). The research only considered those buildings as 'No Damage' and therefore, used those for the analysis. The overall damage map shows that the damage is more intense outside the valley than in its interior. Within the valley, the damage is mainly distributed in North-south direction.

The total number of buildings mapped by NGA, UNOSAT and Copernicus are provided in Table 5-2. It is found that, a total of 12578 buildings were mapped, out of which 33.2% (4170) buildings were marked as 'No damage', around 46% (5750) of buildings were categorized as ' Moderate to severe damage (intermediate damage) and the rest 20% (2658) were found destroyed. The table also shows that the total number of mapped buildings outside the valley (8922) was higher than that of inside the valley (3656). Moreover, the total number of damage buildings (excluding 'No Damage' class) was also high (4968) outside the valley as compared to that of inside the valley (3440). Inside the valley, around two-third of the buildings (2384) was classified as 'Intermediate Damage' and nearly one-third (1056) were named as 'destroyed', whereas for outside the valley, these number was 3366 (38%) and 1602 (18%) respectively.

Table 5-2: Statistics of the Damage Buildings Mapped by NGA, UNOSAT and Copernicus

Category	Inside the valley		Outside the valley		Whole Study Area	
	Number	%	Number	%	Number	%
No damage	216	5.9	3954	44.3	4170	33.2
Intermediate damage	2384	65.2	3366	37.7	5750	45.7
Destroyed	1056	28.9	1602	18.0	2658	21.1
Total	**3656**	**100.0**	**8922**	**100.0**	**12578**	**100.0**

As already mentioned in section 4.3.4, the amplification was categorized into four groups (Low, medium, high, very high amplification). At this stage, the amplification status of three damage classes was analysed which is described in the subsequent sections. Then, the relation between the damage and topography induced amplification was also estimated.

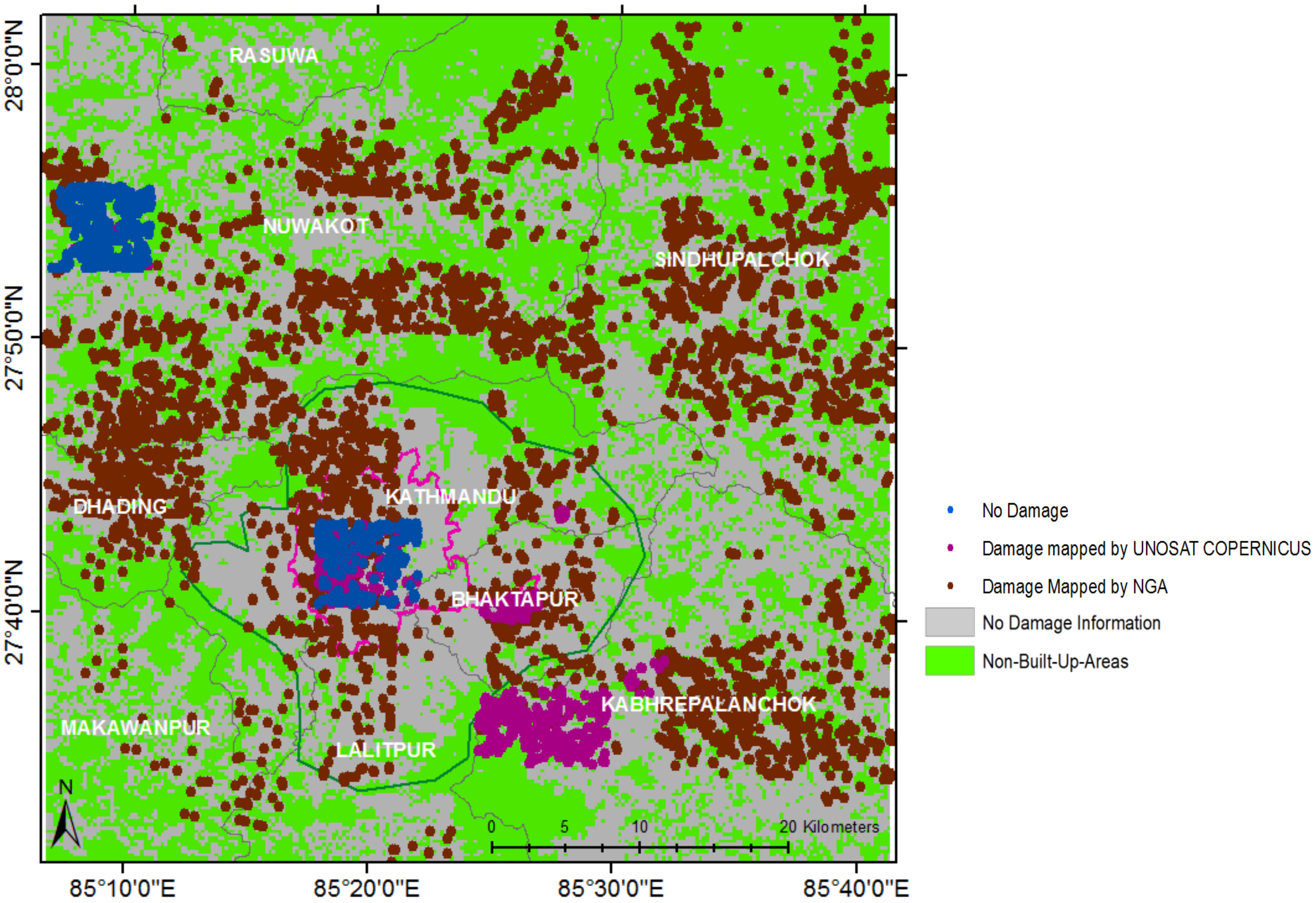

Figure 5-9: Damage map of the study area. The borderline of the Valley and the central Kathmandu areas are also shown. The green colour means no building is there. The grey indicates that there are buildings but no information on the damage status ('Damage' or 'No damage') is provided.

5.2.2. 'No damage' Vs. Amplification

A total of 4170 buildings in Kathmandu metropolitan areas and Nuwakot were detected as 'no damage' by Copernicus (shown by red rectangle) (Figure 5-10). All 'No damage' buildings were spatially overlaid on the PGD amplification map to extract the value of amplification at each building position.

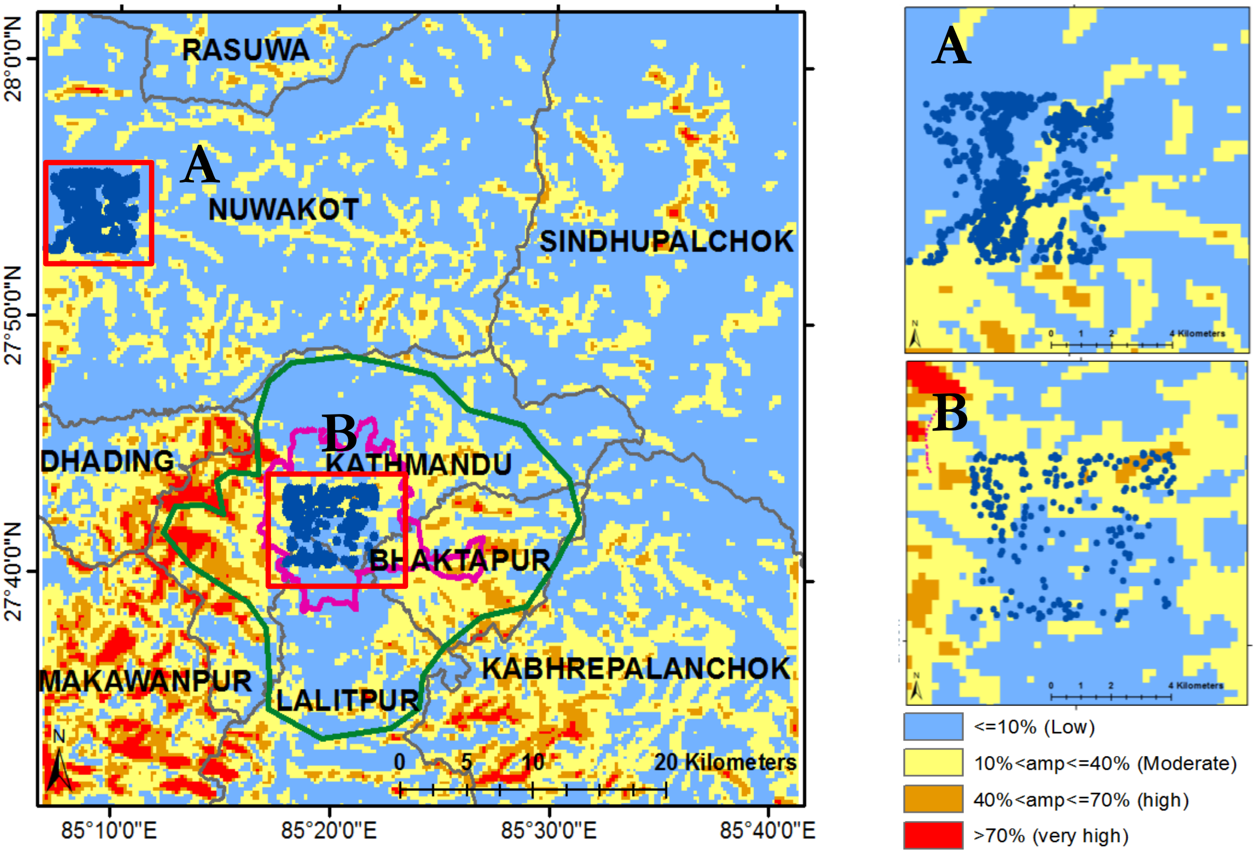

Figure 5-10 : 'No Damage' building class overlaid on PGD amplification map. (A-B) The two clusters of 'No Damage' buildings (blue dots) are enlarged in right side of the figure to get a general idea about the distribution of amplification at individual building position.

Figure 5-10 shows that most of the 'no damage' buildings are located in the low or medium amplification zone. However, high amplification (40 % to 70%) is also observed in some buildings located in the Kathmandu valley.

The distribution of amplification value for 'No damage building classes is shown in Figure 5-11. It is observed that more than two-third of all 'No damage' buildings experienced low amplification (<10%) during the earthquake. Around one-third buildings were shook by moderate amplification. Less than 1% buildings received amplification between 40% to 70%.

From box plot graph (Figure 5-11), it is also found that the amplification value at each 'No damage' building position was mainly within the range of -8% to 12% (corresponds to 25th percentile to 75th percentile value) where the median value is 1%. So, the analysis reveals a very good agreement between the 'No Damage' building and low amplification. However, from box plot graph, it is found that 25 % of the buildings were vibrated by an amplification factor of >12% to 55%. The variability of the amplification value of 'No damage' building might be due to the different types (masonry, Cement concrete, adobe etc.) of building located in those areas. However, the analysis was performed for two small areas which might not be representable for the whole study area. Therefore, additional 'no damage' data for other areas is required to make an overall conclusion for the whole study area.

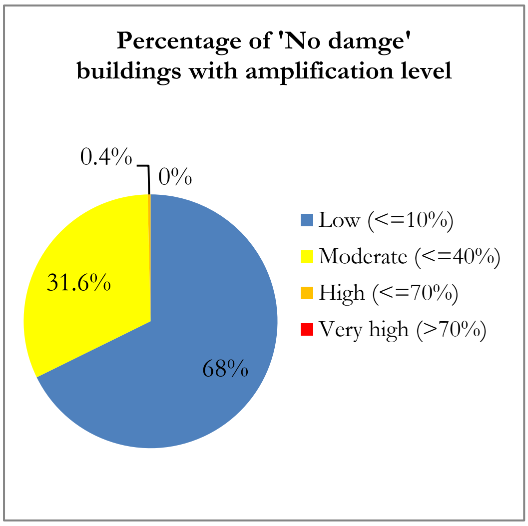

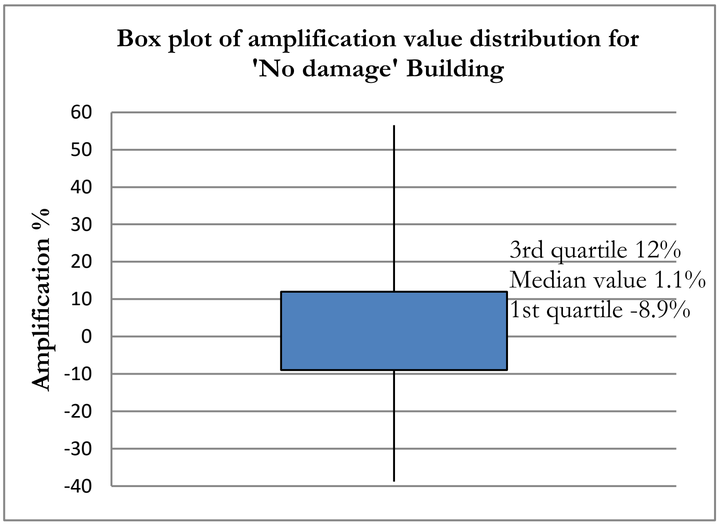

Figure 5-11 : Amplification distribution of 'No Damage' building

5.2.3. 'Destroyed' Building Vs Amplification

The positions of each destroyed buildings are shown in Figure 5-12. A total of 2658 buildings were mapped as 'destroyed'. As can be seen from the figure, the destroyed buildings are spread over the whole study area. However, the concentration of destroyed buildings are high along the east and west border of the valley. Outside the valley, the destroyed buildings are frequently seen in the south-east part (Kabhrepalanchok district), western part (Dhading district) and north-east part (Sindhupalchak district) of the study area.

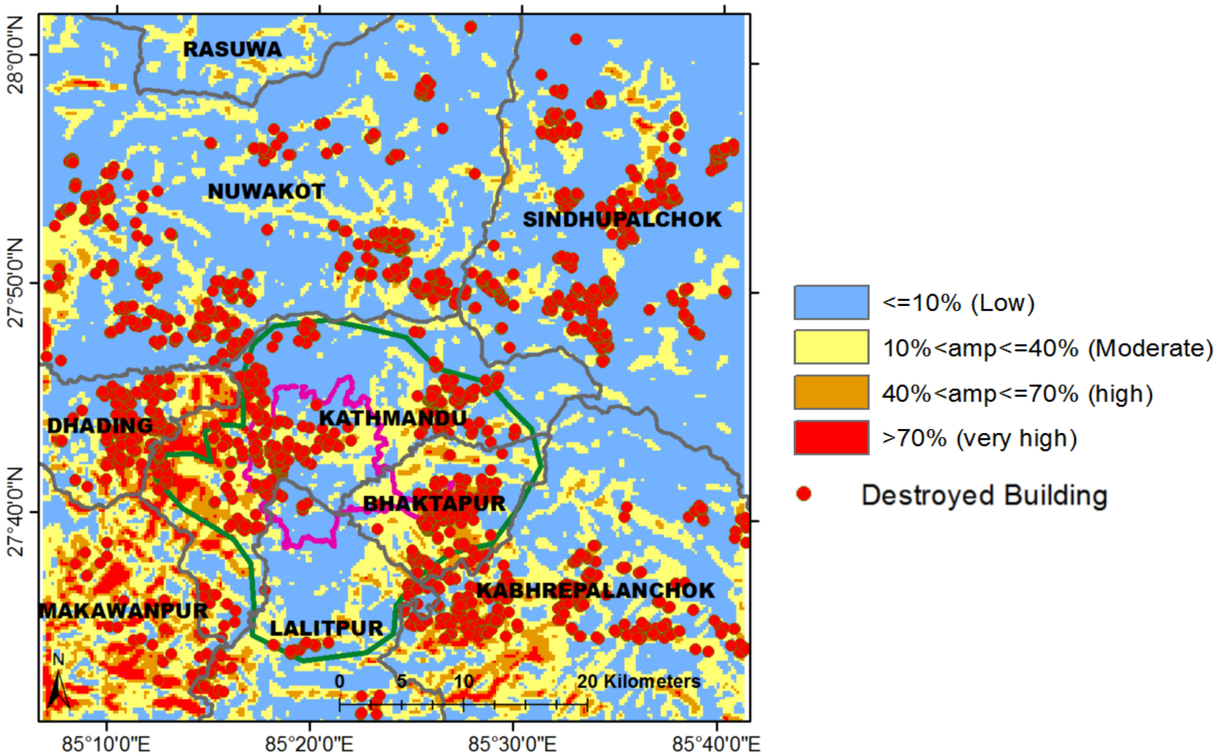

Figure 5-12: Destroyed buildings spatially overlaid on PGD amplification map

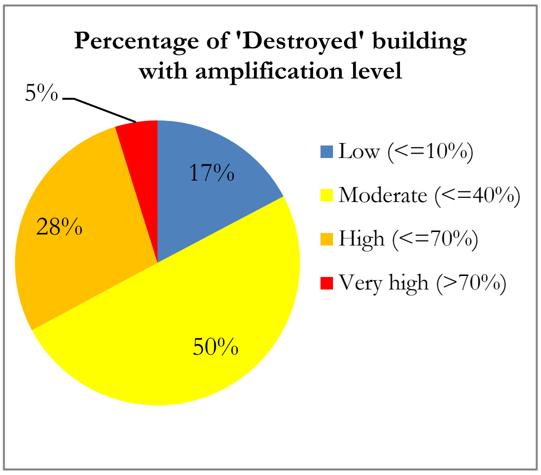

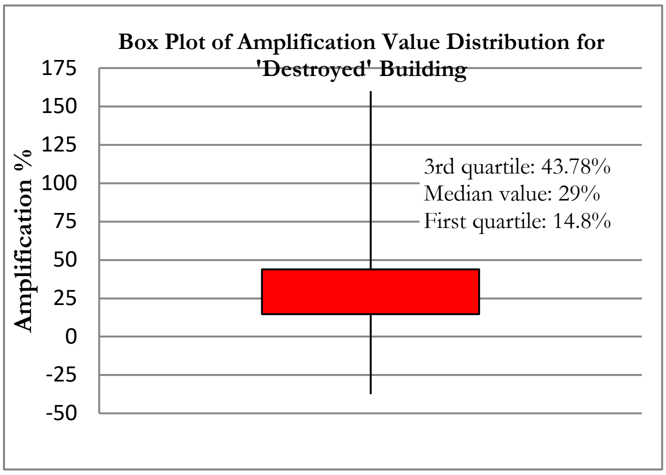

Figure 5-13: Amplification distribution of destroyed buildings

The percentage of destroyed building with amplification level and the distribution of amplification value at each ‘destroyed’ building position are presented in Figure 5-13. The pie chart shows that the amplification values of around 50% of total destroyed buildings were between 10 % to 40%. Around, one-third of the building locations have high amplification (40 % to 70%).

The box plot graph shows that the dominant amplification values for this damage class are ranged between 15 % to 44 %. However, 25% of total buildings were found destroyed even if the amplification value was below 14 % at those buildings positions. A closer look on the Google Earth Map (Figure 5-14) shows that this type of buildings is located along the border line of the valley.

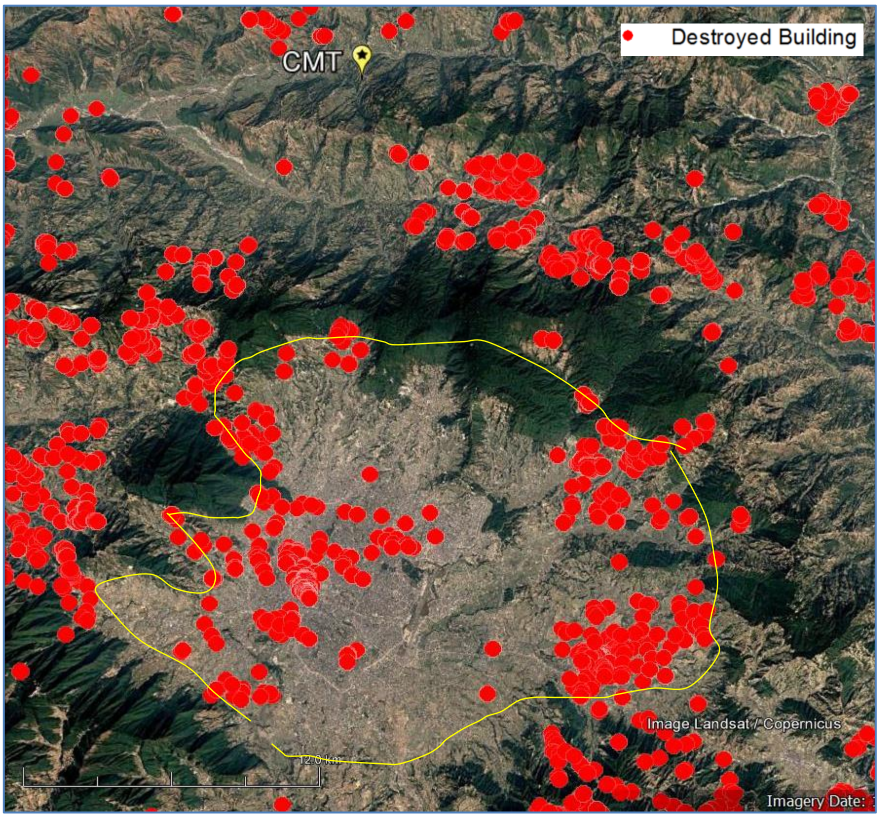

Figure 5-14 : Location of destroyed buildings inside the Kathmandu valley on Google Earth Image. A significant number of destroyed buildings are oriented along the margin of the valley. The outline of the valley is shown by yellow line. The CMT point is also shown.

There can be two possible reasons behind the collapse of the buildings even at low amplification. First: the building quality is very low on these locations. So a very low amplification can have devastating effect to those buildings. This can be true for remote villages where most of the houses are low strength masonry type structures (Government of Nepal, 2015). Second: Especially in the Kathmandu valley, the 'Basin edge effects' might play the significant role behind this damages. Generally large PGD is observed near the basin edge because of the transformation of body waves into the high frequency surface waves (Narayan, 2005) which cause significant damages to the structures. So a combination of basin edge effects along with topography induced amplification could be the reasons behind the collapses of buildings along the edge of the valley.

5.2.4. Intermediate damage (Moderate to Severe damage) Vs. Amplification

A total of 5750 buildings were identified as moderate to severe damage by UNOSAT, Copernicus and NGA. The damage map and the amplification distribution of this damage class are shown in Figure 5-15. This type of damage is also pronounced inside the Kathmandu valley. Outside the valley, this damage was frequently occurred in the north, west and south–southeast (SSE) part of the study area. From pie chart, around 60% of the buildings of this damage class suffered low amplification (below 10%). Near about one-fourth of buildings damages positions, the amplification values were between 10% to 40%.

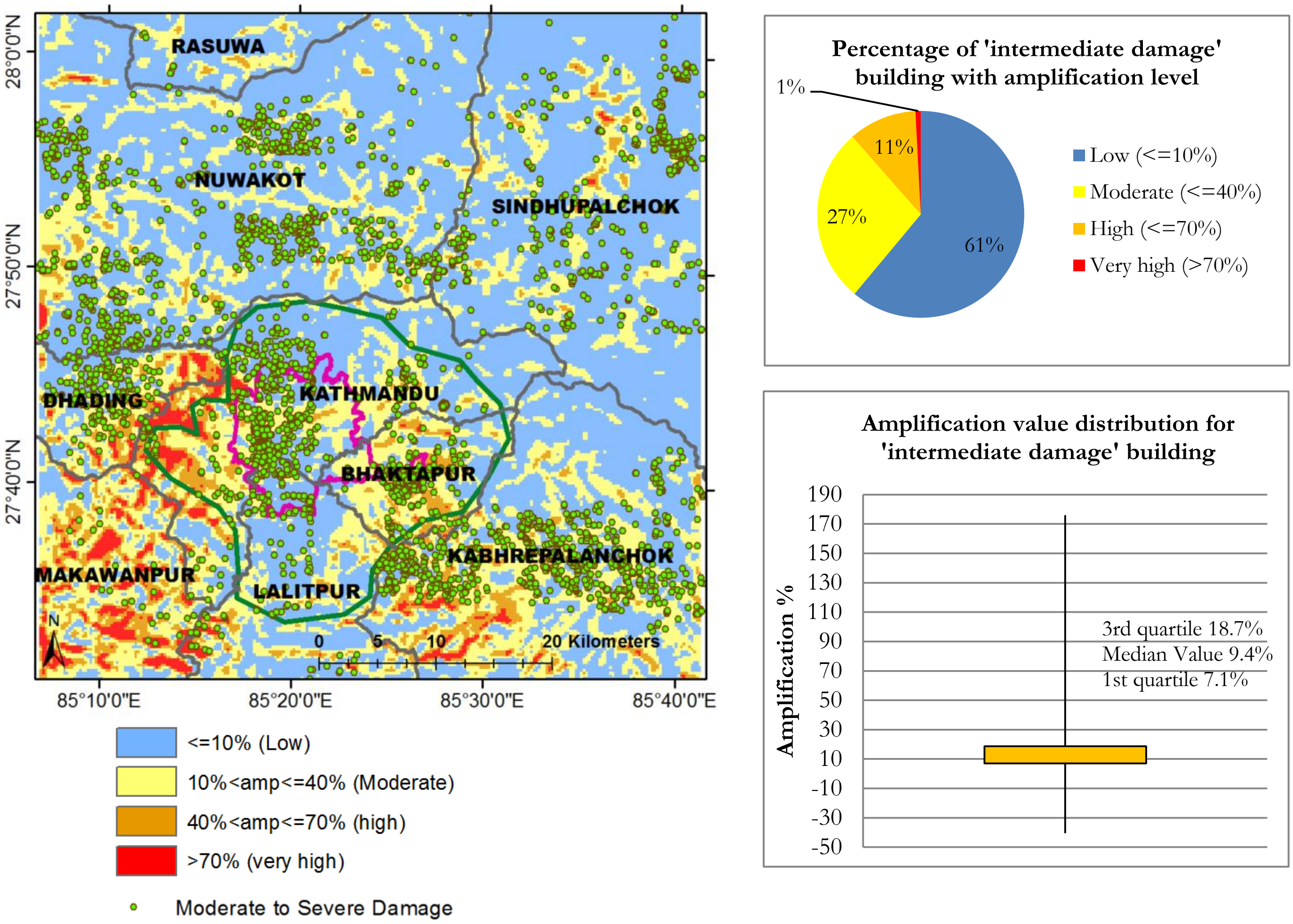

Figure 5-15 : Spatial overlay of intermediate damage buildings on amplification map. The percentage of intermediate damage buildings with amplification distribution are also shown by the pie chart and the box plot.

The box plot shows that, the range of amplification value (1st quartile to 3rd quartile) for this damage mainly varies from 7 % to 19 %. The median value (9%) indicates that within the narrow range of 7% to 9% amplification, 25% of buildings experienced moderate to severe damage. However, the upper whisker of the box plot tells that the amplification of 25 % of the damage buildings fall within the very wide range of value (19% to 175% amplification).

5.2.5. Overall pattern of amplification value in different damage grade

The box plots for three different damage classes are combined in Figure 5-16 to identify the pattern of amplification value in each damage class. It is very clearly observed that the severity of the damage increases when the amplification value goes up. In other words, the results show a clear trend of increasing amplification in accordance with the increasing severity of damages. The median value of amplification for no damage, intermediate damage and destroyed damage classes are 1 %, 9% and 29 % respectively. However, the whisker plot indicates that there were cases where different level of damages was observed under the same amplification value. This indicates that building detail information (building type, height etc.) is utmost important to reveal the reason behind the occurrence of different damage level under the same amplification value. Not only that, Dhakal et al., (2016); Dixit et al., (2015); Rajaure et al., (2016) identified the role of sediment thickness for both amplifying or de-amplifying the seismic wave in different frequencies inside the valley. So, the sediment thickness-induced amplification is also important for explain the damage inside the valley. However, the research only considers the surface topography. Except this limitation, the box plot represents that the model developed under this research is reasonably useful for predicting the severity of damages in the study area.

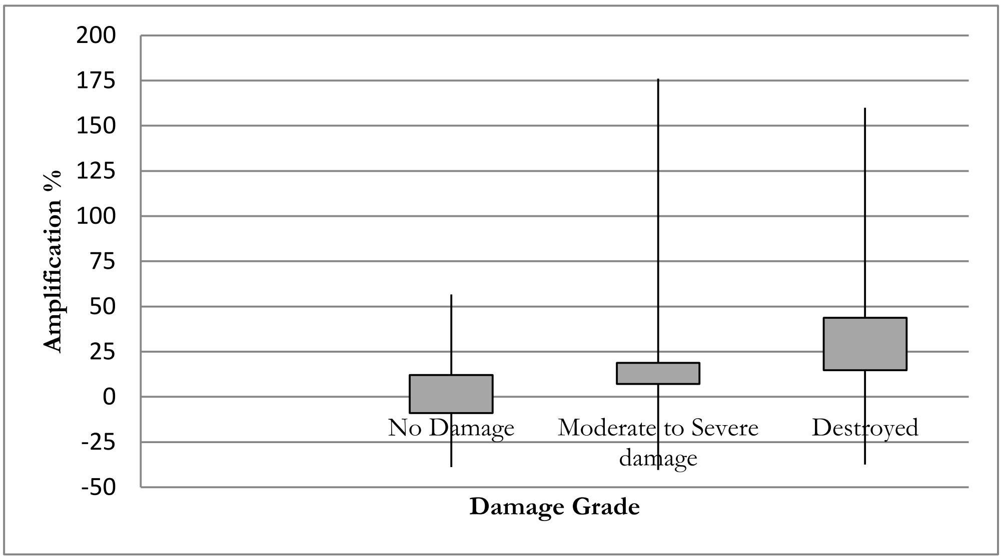

Figure 5-16 : Amplification value distribution for all damage classes

Considering the first and third quartile amplification value for each damage class, an overall summary can be made on the relation between amplification and damages. The summary is provided in Table 5-3. According to the table, an amplification value of up to 14% was found for both no damage and intermediate damage classes. Similarly, at each position of 'moderate to severe damage' or 'destroyed' buildings, the PGD amplification values were varied from 14 % to 18 %. Finally, the spots with amplification value greater than 18% were heavily suffered by complete collapse of the buildings.

Table 5-3 : Overall summary of amplification value distribution for three damage classes

Damage Class	Amplification value (%) range (25th -75th percentile)	Comments
No Damage	0-12	0% to 14% value was found both for 'No Damage' and 'Moderate to severe damage' building positions
Moderate to Severe Damage	7-18	>14% to 18 % value was found both for 'Intermediate damage' and 'Destroyed' building positions
Destroyed	14.7 -44	>18% value was found for 'destroyed' building positions

5.2.6. 'Damage' Building vs. Amplification in Aggregate (Pixel) Level

Figure 5-17 shows the total buildings map and total damage map of the study area. As already mentioned in section 4.3.5, at first the whole study area was divided into 270 m x 270 m grid cells. The total buildings map was prepared by counting the number of buildings located in each cell and assigning the 'counted value' to each cell. Similarly, the damage map was prepared by counting the damaged building only. In this case, there were many cells found where damage information was not available. These cells were assigned 'zero' value in the damage map and excluded from the analysis.

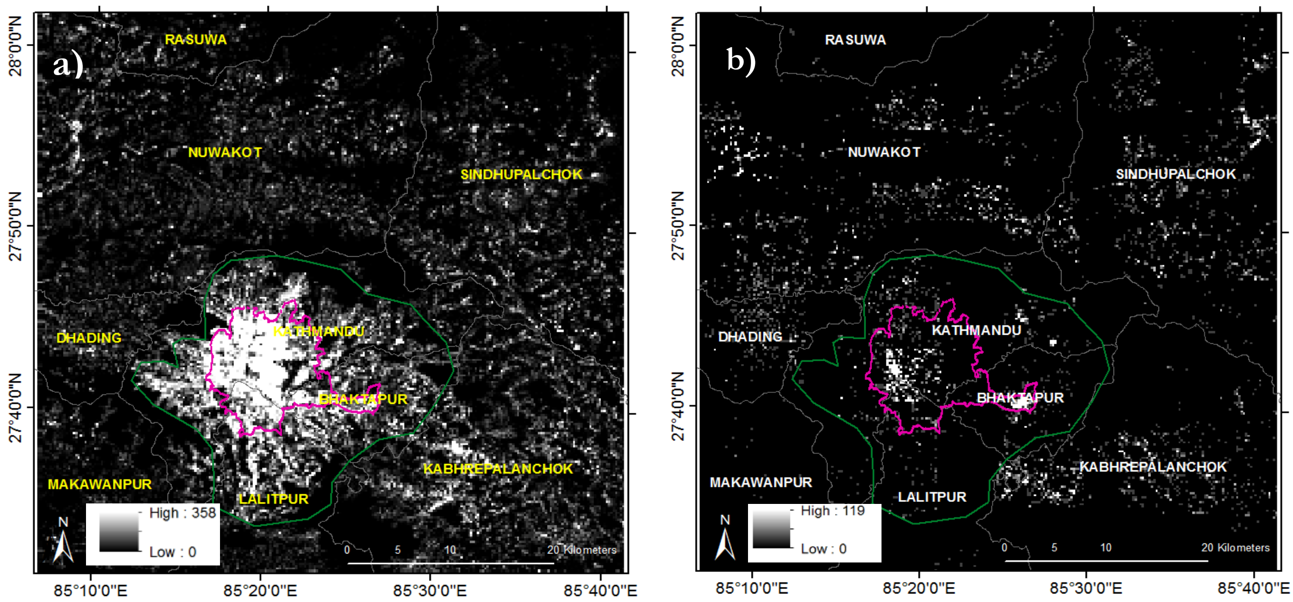

Figure 5-17 : (a) Total buildings map and (b) Total damage map. In each map, the pixel size is 270 m x 270 m. For 'Total buildings map', the value of each pixel defines the total number of buildings located in that particular pixel. For 'Total damage map', it is the number of damaged buildings that determines the value of each pixel.

From the total buildings map, the total number of buildings in each pixel was found to be very high in Kathmandu valley. Similarly the number of damaged buildings was also high in the valley especially in the western side of the central metropolitan areas and Bhaktapur. It is also seen that the areas of Sindhupalchak, Dhading, Kabhrepalanchak and Nuwakot also suffered by significant number of building damages. Note that, the damage map only shows the number of damaged buildings. It does not explain the damage grade of each building.

As also can be seen from damage map of Figure 5-17b, the 'total damage' is not pronounced along the edge of the valley. Actually, the total damage map was prepared by counting the number of damaged buildings irrespective of the damage grades. So, whatever the damage state, every damage building was assigned the value as '1'. In actual observation, along the margin of the valley, most of the damaged buildings were found as 'destroyed'. On the other hand, the buildings in rest of the part of the valley were predominantly suffered by low to severe damage. Based on the available data provided by NGA, UNOSAT and Copernicus, a summary of the damage data in the valley is provided in Figure 5-18. The total number of damage buildings along the margin was 673 out of which 68% buildings were destroyed. In contrast, the central part of the valley was suffered dominantly by the intermediate damage (78%). The total number of damage buildings (2767) in the valley interior was around four times higher than the damage buildings (673) located along the margin. So, the total damage is observed less along the margin of the valley despite the number of destroyed buildings is high.

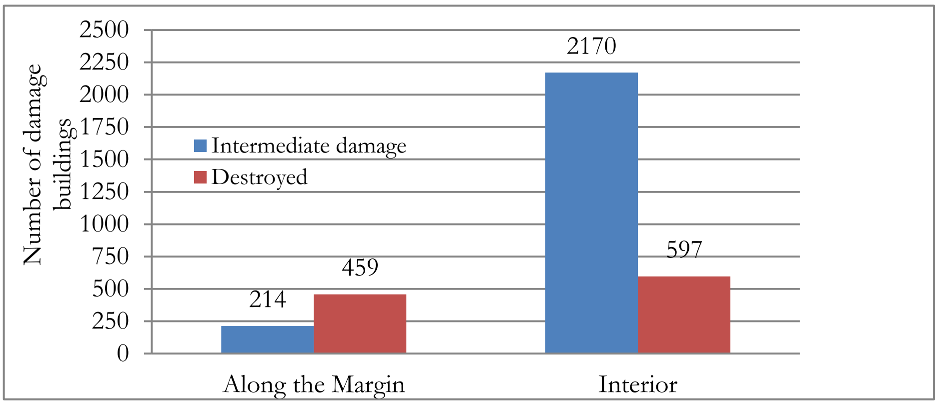

Figure 5-18: Damage data in the Kathmandu valley.

The damage ratio map prepared by dividing the total damage map with total buildings map is presented in Figure 5-19a. To prepare the damage ratio map, only those pixels were counted where the damage information is available. From damage ratio map, it is clearly seen that the damage ratio inside the valley was less as compared to the other areas. The damage ratio per pixel in the valley varies from 0 % to 20%.

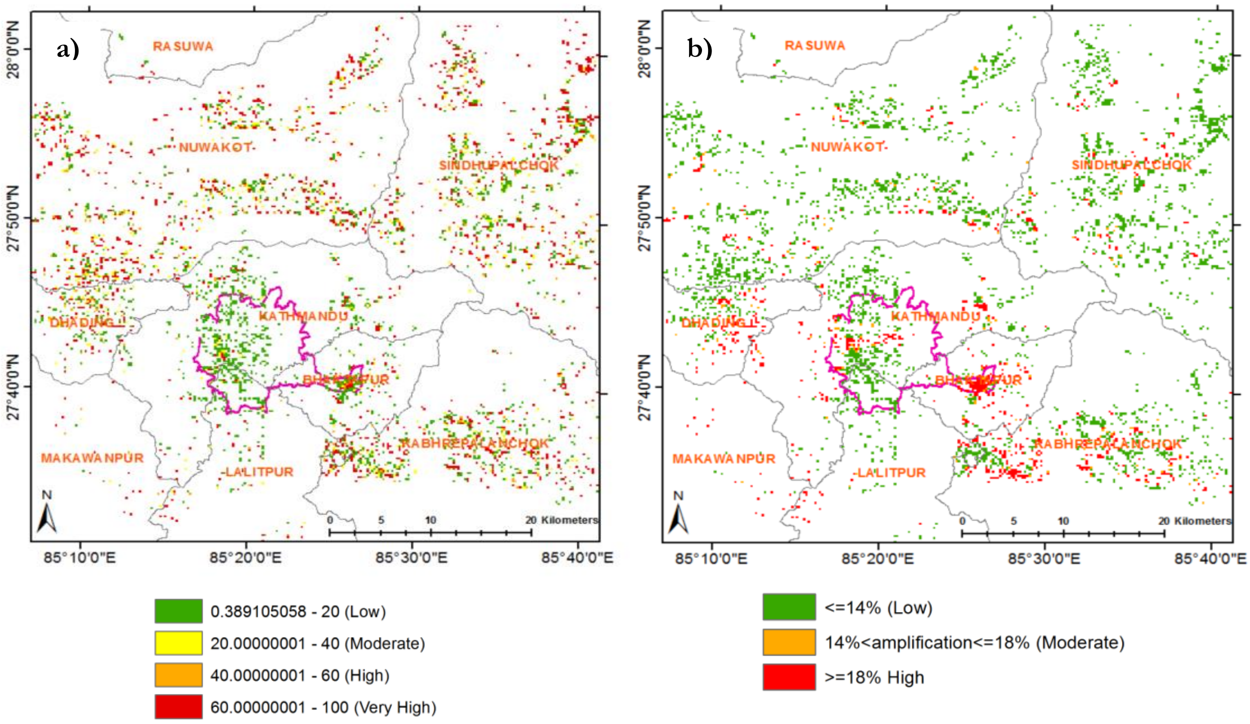

Figure 5-19 : (a) Damage ratio map and (b) Amplification map. The white area of the damage ratio map and amplification map indicates that the damage information is not available.

On the other hand, an amplification map was also prepared (Figure 5-19b) and categorized into three classes based on the Table 5-3. An argument was also developed based on the conclusion made on the Table 5-3. The arguments were as follows:

- A low amplification (0 to 14%) can cause low to moderate damage ratio
- A moderate amplification (>14% to 18%) can cause moderate to high damage ratio
- A high amplification (>18%) can cause very high damage ratio

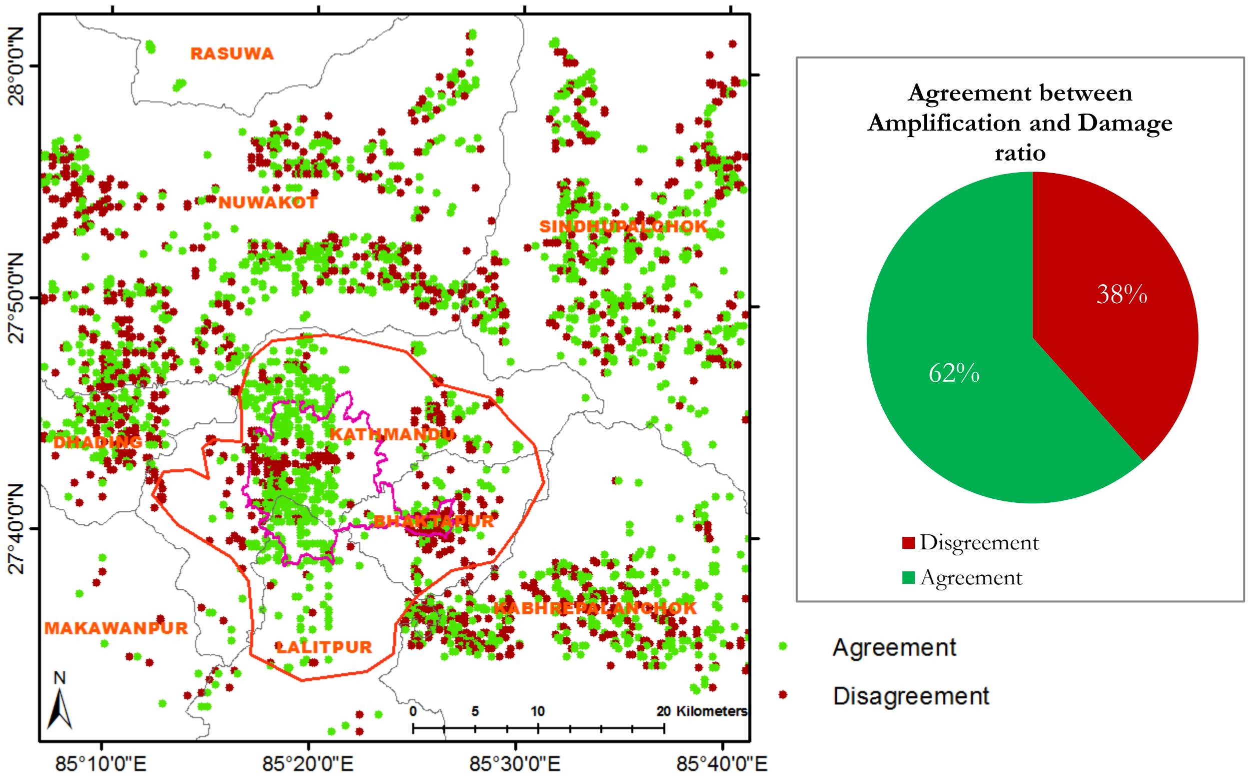

Figure 5-20 : Agreement level between amplification and damage ratio. The green dots mean the amplification can explain the damage, whereas for red dots, it is unable to explain the damage.

Based on the above argument, an agreement analysis was performed on a pixel by pixel level. The results are shown in Figure 5-20 which shows that 62 % of total pixels have agreement between the amplification and damage ratio whereas, 38% of the pixels have no agreement. This indicates that at aggregate level, the model can predict the damage ratio reasonably well. However, the disagreement of 32 % pixels again illustrates that getting building detail information is very crucial for modelling the relationship between the amplification and building damages.

6. CONCLUSIONS AND RECOMMENDATIONS

The principal purpose of this study was to identify the role of surface topography behind less ground shaking observed in the Kathmandu valley during the 2015 Mw 7.8 Nepal earthquake. The Kathmandu valley is quite unique in terms of the position, shape, orientation and elevation of the surrounded mountains and hills. As a result, an inevitable interaction between the seismic wave and the topography was assumed to have occurred during this event. However, this issue was not investigated before. The study has tried to determine the unrevealed role of surface topography for this earthquake. The research used Spectral Element Method (SEM) to develop a DEM derived 3D geometrical model representing the real characteristics of the surface topography of the Kathmandu valley and its surrounding areas. The seismic wave was simulated through the 3D-model in order to generate the ground motion map. The research revealed that the seismic energy was significantly reduced by the surface topography before the energy entered into the valley. Because of the position of surface topography, the seismic energy was scattered and reflected and therefore, creating a shadow zone inside the valley. As a result, the highly populated central areas of Kathmandu valley were amplified by a low factor of 0.1. However, the interference of the scattered and reflected wave with the direct wave created massive shaking (a minimum factor of 1.0) along the periphery of the valley.

The research also tried to determine the extended role of surface topography by placing the Mw 7.8 earthquake source in different locations inside the study area. It was found that the surface topography did not always act as a shield of the valley. Depending on the position of earthquake source, the surface topography fully or partly insulated the seismic energy; even in one case, surface topography invited more seismic energy into the valley.

The research used a simple model where uniform velocity of P-wave and S-wave and material properties were defined over the whole volume block. The study also used ~270 m coarse DEM and did not incorporate the fault in SEM mesh generation. Koketsu et al., (2016) and U.S. Geological Survey, (2016a) have developed depth varying velocity, material properties and attenuation model in Nepal region, especially after the occurrence of the 2015 earthquake. Yet, the synthetic seismogram produced by the present model showed reasonably good agreement with the observed seismogram. But, using high resolution DEM, multi-layer velocity model as well as incorporating fault in SEM mesh, it should be possible to produce more accurate results.

Another very important purpose of this research was to determine the ability of the model for explaining the pattern and distribution of damages observed in the aftermath of the 2015 Nepal main shock. A general pattern of relationship between the amplification and damage level was depicted by the model. The analysis indicates that the amplification value found at each 'destroyed' building position was higher than that of 'Moderate to Severe damage' building. Similarly, the amplification value found at each 'No damage' building location was close to zero. The model also performs reasonably well to explain the intensity of damages (i.e. percentage of total buildings suffered damages) in the study areas. Overall, the results show that the higher grade of damage is occurred when the amplification values go up. This indicates that the ground motion amplification and the building damages are complement to each other. However, the research realized that (i) a combination of sediment-induced and surface-topography induced amplification could explain the damage better, especially inside the valley; and (ii) without knowing the information about the building type it is not possible to make an overall conclusion about the relationship between the damage and amplification. Apart from this, the resolution of DEM was very high as compared to the area of each building. The average area of a single building in Nepal varies largely from 30 m^2 to 90 m^2 in different districts (CBS, 2012). So, a finer resolution DEM (at or below 30 m) can be used to accurately model the relation between the topography induced amplification and the damages provided that the sufficient information (type, height and damage grade) of building is available.

The overall findings emphasize that surface topography should be considered as a crucial factor behind the limited ground shaking and limited damage observed during the 2015 Mw 7.8 Earthquake. Kathmandu valley is located in the 'central seismic gap' (Khattri, 1987) of the Himalayan region and only a small amount of the fault was ruptured during the 2015 Nepal earthquake (Avouac et al., 2015). Therefore, this region is expected to be affected by further significant earthquakes in the near future. The present research illuminates the fact that surface topography must be considered for seismic hazard assessment in the Kathmandu valley and surrounding regions. In this context, this study is very useful for the government, engineers and planners for effective infrastructure planning as well as for developing earthquake preparedness and response plan.

LIST OF REFERENCES

Ader, T., Avouac, J., Liu-zeng, J., Lyon-caen, H., Bollinger, L., Galetzka, J., … Flouzat, M. (2012). Convergence rate across the Nepal Himalaya and interseismic coupling on the Main Himalayan Thrust : Implications for seismic hazard. *Journal of Geophysical Research*, *117*(B04403), 1–16. http://doi.org/10.1029/2011JB009071

Adhikari, L. B., Gautam, U. P., Koirala, B. P., Bhattarai, M., Kandel, T., Gupta, R. M., … Bollinger, L. (2015). The aftershock sequence of the 2015 April 25 Gorkha–Nepal earthquake. *Geophysical Journal International*, *203*(3), 2119–2124. http://doi.org/10.1093/gji/ggv412

Assimaki, D. (2004). *Topography Effects in the 1999 Athens Earthquake: Engineering Issues in Seismology*. Massachusetts Institute of Technology.

Athanasopoulos, G. A., Pelekis, P. C., & Leonidou, E. A. (1999). Effects of surface topography on seismic ground response in the Egion (Greece) 15 June 1995 earthquake. *Soil Dynamics and Earthquake Engineering*, *18*(2), 135–149. http://doi.org/10.1016/S0267-7261(98)00041-4

Avouac, J.-P. (2003). Mountain Building , Erosion , and the Seismic Cycle in the Nepal Himalaya. *Advances in Geophysics*, *46*(2003), 1–80. http://doi.org/10.1016/S0065

Avouac, J. P., Meng, L., Wei, S., Wang, T., & Ampuero, J. P. (2015). Lower edge of locked Main Himalayan Thrust unzipped by the 2015 Gorkha earthquake. *Nature Geoscience*, *8*(9), 708–711. Retrieved from http://dx.doi.org/10.1038/ngeo2518

Baker, J. W. (2008). *An introduction to Probabilistic Seismic Hazard Analysis (PSHA). Baker research group*. Stanford. Retrieved from http://www.stanford.edu/~bakerjw/Publications/Baker_(2008)_Intro_to_PSHA_v1_3.pdf

Bao, H., Bielak, J., Ghattas, O., Kallivokas, L. F., O'Hallaron, D. R., Shewchuk, J. R., & Xu, J. (1998). Large-scale simulation of elastic wave propagation in heterogeneous media on parallel computers. *Computer Methods in Applied Mechanics and Engineering*, *152*(1), 85–102. http://doi.org/10.1016/S0045-7825(97)00183-7

Bard, P.-Y. (1982). Diffracted waves and displacement field over two-dimensional elevated topographies. *Geophysical Journal International*, *71*(3), 731–760. http://doi.org/10.1111/j.1365-246X.1982.tb02795.x

Bhattarai, M., Adhikari, L. B., Gautam, U. P., Laurendeau, A., Labonne, C., Hoste-Colomer, R., … Hernandez, B. (2015). Overview of the Large 25 April 2015 Gorkha, Nepal, Earthquake from Accelerometric Perspectives. *Seismological Research Letters*, *86*(6), 1540–1548. http://doi.org/10.1785/0220150140

Bielak, J., Loukakis, K., Hisada, Y., & Yoshimura, C. (2003). Domain Reduction Method for Three-Dimensional Earthquake Modeling in Localized Regions, Part I: Theory. *Bulletin of the Seismological Society of America*, *93*(2).

Bilham, R. (1995). Location andmagnitude of the 1833Nepal earthquake and its relation to the rupture zones of contiguous great Himalayan earthquakes. *Current Science*, *69*(2), 101–127.

Bohlen, T., & Saenger, E. H. (2006). Accuracy of heterogeneous staggered-grid finite-difference modeling of Rayleigh waves. *Geophysics*, *71*(4).

Bommer, J. J., & Akkar, S. (2012). Consistent source-to-site distance metrics in ground-motion prediction equations and seismic source models for PSHA. *Earthquake Spectra*, *28*(1), 1–15. http://doi.org/10.1193/1.3672994

Boore, D. M. (1972). A NOTE ON THE EFFECT OF SIMPLE TOPOGRAPHY ON SEISMIC SH WAVES. *Bulletin of the Seismological Society of America*, *62*(1), 275–284.

Boore, D. M. (1973). The effect of simple topography on seismic waves: Implications for the accelerations recorded at Pacoima Dam, San Fernando Valley, California. *Bulletin of the Seismological Society of America*, *63*(5), 1603–1609.

Boore, D. M., Harmsen, S. C., & Harding, S. T. (1981). Wave scattering from a step change in surface topography. *Bulletin of the Seismological Society of America*, *71*(1).

Boore, D. M., Stewart, J. P., Seyhan, E., & Atkinson, G. M. (2014). NGA-West2 Equations for Predicting PGA, PGV, and 5% Damped PSA for Shallow Crustal Earthquakes. *Earthquake Spectra*, *30*(3), 1057–1085. http://doi.org/10.1193/070113EQS184M

Bouchon, M., & Barker, J. S. (1996). Seismic response of a hill: The example of Tarzana, California. *Bulletin of the Seismological Society of America*, *86*(1A), 66–72.

Bouchon, M., Schultz, C. A., & Toksöz, M. N. (1996). Effect of three-dimensional topography on seismic motion. *Journal of Geophysical Research: Solid Earth*, *101*(B3), 5835–5846. http://doi.org/10.1029/95JB02629

Bouckovalas, G. D., & Papadimitriou, A. G. (2005). Numerical evaluation of slope topography effects on seismic ground motion. *Soil Dynamics and Earthquake Engineering*, *25*(7–10), 547–558. http://doi.org/10.1016/j.soildyn.2004.11.008

Canuto, C., Hussaini, M. Y., Quarteroni, A., & Zang, A. T. (1988). *Spectral Methods in Fluid Dynamics*. New York: Springer-Verlag. http://doi.org/10.1007/978-3-642-84108-8

Carrington, L., Komatitsch, D., Laurenzano, M., Tikir, M., Michéa, D., Le Goff, N., … Tromp, J. (2008). High-frequency simulations of global seismic wave propagation using SPECFEM3D_GLOBE on 62 thousand processor cores. In *2008 SC - International Conference for High Performance Computing, Networking, Storage and Analysis* (pp. 1–11). Austin, TX: IEEE. http://doi.org/10.1109/SC.2008.5215501

Casarotti, E., Stupazzini, M., Lee, S. J., Komatitsch, D., Piersanti, A., & Tromp, J. (2008). CUBIT and seismic wave propagation based upon the Spectral-Element Method: An advanced unstructured mesher for complex 3D geological media. *Proceedings of the 16th International Meshing Roundtable, IMR 2007*, 579–597. http://doi.org/10.1007/978-3-540-75103-8_32

CBS. (2012). *National Population and Housing Census 2011 (National Report)* (Vol. 1). Kathmandu. Retrieved from http://cbs.gov.np/atlas/general.html?page=population_and_housing_cencus

Celebi, M. (1987). Topographical and geological amplications determined from strongmotion and aftershock records of the 3 March 1985 Chile earthquake. *Ulletin of the Seismological Society of America*, *77 (4)*(1987), 1147–1167.

Celebi, M. (1991). Topographical and geological amplification: case studies and engineering implications. *Structural Safety*, *10*(1–3), 199–217. Retrieved from http://pubs.er.usgs.gov/publication/70016616

Celebi, M., Bazzurro, P., Chiaraluce, L., Clemente, P., Decanini, L., Desortis, A., … Stephens, C. (2010). Recorded motions of the 6 April 2009 Mw 6.3 L'Aquila, Italy, earthquake and implications for building structural damage: Overview. *Earthquake Spectra*, *26*(3), 651–684. http://doi.org/10.1193/1.3450317

Chaljub, E. (2006). Spectral Element Modeling of 3D Wave Propagation in the Alpine Valley of Grenoble, France. In *Third International Symposium on the Effects of Surface Geology on Seismic Motion* (Vol. 2, pp. 1467–1473). Grenoble. Retrieved from http://www.risknat.org/projets/sismovalp/CD3/a-Papers/12-Chaljub-pSO4_ESG 2006.pdf%5Cnpapers2://publication/uuid/67E17E6D-EA25-4977-9B56-274DA7B810D7

Chaljub, E., Komatitsch, D., Vilotte, J.-P., Capdeville, Y., Valette, B., & Festa, G. (2005). Spectral-Element Analysis in Seismology. *IASPEI*.

CIG. (2016). Computational Infrastructure for Geodynamics : SPECFEM3D Cartesian. Retrieved December 29, 2016, from https://geodynamics.org/cig/software/specfem3d/

Cupillard, P., Delavaud, E., Burgos, G., Festa, G., Vilotte, J.-P., Capdeville, Y., & Montagner, J.-P. (2012). RegSEM: a versatile code based on the spectral element method to compute seismic wave propagation at the regional scale. *Geophysical Journal International*, *188*(3), 1203–1220. http://doi.org/10.1111/j.1365-246X.2011.05311.x

Davis, L. L., & West, L. R. (1973). Observed effects of topography on ground motion. *Bulletin of the Seismological Society of America*, *63(1)*. http://doi.org/10.1017/CBO9781107415324.004

Delgado, D. B. (2009). *High-order finite element methods for seismic wave propagation (PhD Thesis)*. The University of Texas at Austin. Retrieved from https://repositories.lib.utexas.edu/handle/2152/6864

Dell'Acqua, F., & Gamba, P. (2012). Remote sensing and earthquake damage assessment: Experiences, limits, and perspectives. *Proceedings of the IEEE*, *100*(10), 2876–2890. http://doi.org/10.1109/JPROC.2012.2196404

Detweiler, S., & Reddy, P. R. (2016). The 2015 M7 . 8 Gorkha , Nepal , Earthquake : Possible Implications for Northeastern India. *J. Ind. Geophys. Union*, *20*(April), 291–294.

Dhakal, Y. P., Kubo, H., Suzuki, W., Kunugi, T., Aoi, S., & Fujiwara, H. (2016). Analysis of strong ground motions and site effects at Kantipath, Kathmandu, from 2015 Mw 7.8 Gorkha, Nepal, earthquake and its aftershocks. *Earth, Planets and Space*, *68*(1), 58. http://doi.org/10.1186/s40623-016-0432-2

Dhanya, J., Gade, M., & Raghukanth, S. T. G. (2016). Ground motion estimation during 25th April 2015 Nepal earthquake. *Acta Geodaetica et Geophysica*, (April 2015). http://doi.org/10.1007/s40328-016-0170-8

Diao, F., Walter, T. R., Motagh, M., Prats-Iraola, P., Wang, R., & Samsonov, S. V. (2015). The 2015 Gorkha earthquake investigated from radar satellites: Slip and stress modeling along the MHT.

Frontiers in Earth Science, *3*(October), 1–9. http://doi.org/10.3389/feart.2015.00065

Dixit, A. M., Ringler, A. T., Sumy, D. F., Cochran, E. S., Hough, S. E., Martin, S. S., … McNamara, D. E. (2015). Strong-Motion Observations of the M 7.8 Gorkha, Nepal, Earthquake Sequence and Development of the N-SHAKE Strong-Motion Network. *Seismological Research Letters*, *86*(6), 1533–1539. http://doi.org/10.1785/0220150146

Duputel, Z., Kanamori, H., Tsai, V. C., Rivera, L., Meng, L., Ampuero, J. P., & Stock, J. M. (2012). The 2012 Sumatra great earthquake sequence. *Earth and Planetary Science Letters*, *351–352*(January), 247–257. http://doi.org/10.1016/j.epsl.2012.07.017

Ekström, G., Nettles, M., & Dziewoński, A. M. (2012). The global CMT project 2004-2010: Centroid-moment tensors for 13,017 earthquakes. *Physics of the Earth and Planetary Interiors*, *200–201*, 1–9. http://doi.org/10.1016/j.pepi.2012.04.002

Elliott, J. R., Jolivet, R., González, P. J., Avouac, J.-P., Hollingsworth, J., Searle, M. P., & Stevens, V. L. (2016). Himalayan megathrust geometry and relation to topography revealed by the Gorkha earthquake. *Nature Geoscience*, *9*(2), 174–180. http://doi.org/10.1038/ngeo2623

Fan, W., & Shearer, P. M. (2015). Detailed rupture imaging of the 25 April 2015 Nepal earthquake using teleseismic P waves. *Geophysical Research Letters*, *42*(14), 5744–5752. http://doi.org/10.1002/2015GL064587

Frankel, A., & Vidale, J. (1992). A three-dimensional simulation of seismic waves in the Santa Clara Valley, California, from a Loma Prieta aftershock. *Bulletin of the Seismological Society of America*, *82*(5), 2045–2074.

Galetzka, J., Melgar, D., Genrich, J. F., Geng, J., Owen, S., Lindsey, E. O., … Hudnut, K. W. (2015). Slip pulse and resonance of Kathmandu basin during the 2015 Gorkha earthquake, Nepal. *Science*, (July).

Gautam, D., Bhetwal, Krishna Kumar Rodrigues, H., Neupane, P., & Sanada, Y. (2015). Observed Damage Patterns on Buildings during 2015 Gorkha (Nepal) Earthquake. In *In Proceedings of the 14th International Symposium on New Technologies for Urban Safety of Mega Cities in Asia* (p. 8). Kathmandu. http://doi.org/10.13140/RG.2.1.4422.3444

Géli, L., Bard, P. Y., & Julien, B. (1988). The effect of topography on earthquake ground motion: a review and new results. *Bulletin of the Seismological Society of America*, *78*, *No. 1*, 42–63.

Geller, R. J., Jackson, D. D., Kagan, Y. Y., & Mulargia, F. (1997). Earthquakes Cannot Be Predicted. *Science*, *275*(5306), 1616–1616. http://doi.org/10.1126/science.275.5306.1616

Global Centroid Moment Tensor Catalog. (2016). Retrieved December 15, 2016, from http://www.globalcmt.org/CMTsearch.html

Global Seismic Hazard Assessment Program. (1999). Retrieved December 19, 2016, from http://www.seismo.ethz.ch/static/GSHAP/

Goda, K., Kiyota, T., Pokhrel, R. M., Chiaro, G., Katagiri, T., Sharma, K., & Wilkinson, S. (2015). The 2015 Gorkha Nepal Earthquake: Insights from Earthquake Damage Survey. *Frontiers in Built Environment*, *1*(April), 1–15. http://doi.org/10.3389/fbuil.2015.00008

Government of Nepal, N. P. C. (2015). *Nepal Earthquake 2015 Post Disaster Needs Assessment: Sector Reports (Volume B)*. Singha Durbar, Kathmandu. Retrieved from www.npc.gov.np

Grandin, R., Doin, M. P., Bollinger, L., Pinel-Puysségur, B., Ducret, G., Jolivet, R., & Sapkota, S. N. (2012). Long-term growth of the Himalaya inferred from interseismic InSAR measurement. *Geology*, *40*(12), 1059–1062. http://doi.org/10.1130/G33154.1

Grandin, R., Vallée, M., Satriano, C., Lacassin, R., Klinger, Y., Simoes, M., & Bollinger, L. (2015). Rupture process of the Mw=7.9 2015 Gorkha earthquake (Nepal): Insights into Himalayan megathrust segmentation. *Geophysical Research Letters*, *42*(20), 8373–8382. http://doi.org/10.1002/2015GL066044.Received

Greicius, T. (2015). Radar Shows Kathmandu Area Uplifted 5 Feet by Gorkha, Nepal Earthquake. Retrieved February 8, 2017, from https://www.nasa.gov/jpl/

Griffiths, D. W., & Bollinger, G. A. (1979). The effect of Appalachian Mountain topography on seismic waves. *Bulletin of the Seismological Society of America*, *69*(4), 1081–1105.

Hand, E. (2015). Why the Nepal earthquake was far less damaging than feared. http://doi.org/10.1126/science.aac8979

Hartzell, S. H., Carver, D. L., & King, K. W. (1994). Initial investigation of site and topographic effects at Robinwood Ridge, California. *Bulletin of the Seismological Society of America*, *84*(5), 1336–1349.

Hashash, Y., Tiwari, B., Moss, R., Asimaki, D., Clahan, K., Kieffer, D., … Adhikari, B. (2015). *Geotechnical Field Reconnaissance: Gorkha (Nepal) Earthquake of April 25, 2015 and Related Shaking Sequence*. *Geotechnical Extreme Event Reconnaisance GEER Association, Report No. GEER-040*. Retrieved from http://digitalcommons.calpoly.edu/cenv_fac/311

Hough, S. E. (2015). Introduction to the Focus Section on the 2015 Gorkha, Nepal, Earthquake. *Seismological Research Letters*, *86*(6), 1502–1505. http://doi.org/10.1785/0220150212

Hough, S. E., Altidor, J. R., Anglade, D., Given, D., Janvier, M. G., Maharrey, J. Z., … Yong, A. (2010). Localized damage caused by topographic amplification during the 2010 Mw7.0 Haiti earthquake. *Nature Geoscience*, *3*(11), 778–782. Retrieved from http://dx.doi.org/10.1038/ngeo988

Huang, Q., Gerstenberger, M., & Zhuang, J. (2016). Current Challenges in Statistical Seismology. *Pure and Applied Geophysics*, *173*(1), 1–3. http://doi.org/10.1007/s00024-015-1222-7

Hughes, T. J. R., Reali, A., & Sangalli, G. (2008). Duality and unified analysis of discrete approximations in structural dynamics and wave propagation: Comparison of p-method finite elements with k-method NURBS. *Computer Methods in Applied Mechanics and Engineering*, *197*(49), 4104–4124. http://doi.org/10.1016/j.cma.2008.04.006

Ichiyanagi, M., Takai, N., Shigefuji, M., Bijukchhen, S., Sasatani, T., Rajaure, S., … Takahashi, H. (2016). Aftershock activity of the 2015 Gorkha, Nepal, earthquake determined using the Kathmandu strong motion seismographic array. *Earth, Planets and Space*, *68*(1), 25. http://doi.org/10.1186/s40623-016-0402-8

IPGP. (2016). Central Nepal Earthquake - April 25th, 2015. Retrieved January 3, 2016, from http://www.ipgp.fr/en/central-nepal-earthquake-april-25th-2015

Jayalakshmi, S., & Raghukanth, S. T. G. (2016). Regional ground motion simulation around Delhi due to future large earthquake. *Natural Hazards*, *82*(3), 1479–1513. http://doi.org/10.1007/s11069-016-2254-8

Kamalian, M., Gatmiri, B., Sohrabi-Bidar, A., & Khalaj, A. (2006). Amplification pattern of 2D semi-sine-shaped valleys subjected to vertically propagating incident waves. *Communications in Numerical Methods in Engineering*, *23*(9), 871–887. http://doi.org/10.1002/cnm.933

Kawase, H., & Aki, K. (1990). Topography effect at the critical SV-wave incidence: Possible explanation of damage pattern by the Whittier Narrows, California, earthquake of 1 October 1987. *Bulletin of the Seismological Society of America*, *80*(1), 1–22.

Kerle, N. (2010). Satellite-based damage mapping following the 2006 Indonesia earthquake-How accurate was it? *International Journal of Applied Earth Observation and Geoinformation*, *12*(6), 466–476. http://doi.org/10.1016/j.jag.2010.07.004

Khan, S., Meijde, M., & Werff, H. (2015). The Impact of DEM and Mesh Resolution in a 3D Simulation of Seismic Response. In *EGU general assembly* (Vol. 17, p. 9106). Vienna, Austria: European Geosciences Union.

Khattri, K. N. (1987). Great earthquakes, seismicity gaps and potential for earthquake disaster along the Himalaya plate boundary. *Tectonophysics*, *138*(1), 79–92. http://doi.org/10.1016/0040-1951(87)90067-9

Koketsu, K., Miyake, H., Guo, Y., Kobayashi, H., Masuda, T., Davuluri, S., … Sapkota, S. N. (2016). Widespread ground motion distribution caused by rupture directivity during the 2015 Gorkha, Nepal earthquake. *Scientific Reports*, *6*(June), 28536. http://doi.org/10.1038/srep28536

Komatitsch, D., Liu, Q., Tromp, J., Süss, P., Stidham, C., & Shaw, J. H. (2004). Simulations of ground motion in the Los Angeles basin based upon the spectral-element method. *Bulletin of the Seismological Society of America*, *94*(1), 187–206. http://doi.org/10.1785/0120030077

Komatitsch, D., & Tromp, J. (1999). Introduction to the spectral element method for three-dimensional seismic wave propagation. *Geophysical Journal International*, *139*(3), 806–822. http://doi.org/10.1046/j.1365-246X.1999.00967.x

Komatitsch, D., Tsuboi, S., & Tromp, J. (2005). The Spectral-Element Method in Seismology. In *Seismic Earth: Array Analysis of Broadband Seismograms, Geophysical Monograph Series 157* (pp. 205–227). American Geophysical Union. http://doi.org/10.1029/157GM13

Komatitsch, D., & Vilotte, J.-P. (1998). The Spectral Element Method : An Efficient Tool to Simulate the Seismic Response of 2D and 3D Geological Structures. *Bulletin of the Seismological Society of America*, *88*(2), 368–392. Retrieved from http://bssa.geoscienceworld.org/content/88/2/368.short

Komatitsch, D., Vilotte, J., Tromp, J., & Team. (2015). *SPECFEM 3D cartesian user manual version 3*.

Kramer, S. L. (1996). *GEOTECHNICAL EARTHQUAKE ENGINEERING*. New Jersy: Prentice-Hall.

Lee, S.-J., Komatitsch, D., Huang, B.-S., & Tromp, J. (2009). Effects of Topography on Seismic-Wave Propagation : An Example from Northern Taiwan Effects of Topography on Seismic-Wave Propagation :, (July 2016). http://doi.org/10.1785/0120080020

Lee, S.-J., Liu, Q., Tromp, J., Komatitsch, D., Liang, W. T., & Huang, B. S. (2014). Toward real-time regional earthquake simulation II: Real-time Online earthquake Simulation (ROS) of Taiwan earthquakes. *Journal of Asian Earth Sciences*, *87*, 56–68. http://doi.org/10.1016/j.jseaes.2014.02.009

Lee, S. J., Chan, Y. C., Komatitsch, D., Huang, B. S., & Tromp, J. (2009). Effects of realistic surface topography on seismic ground motion in the Yangminshan region of Taiwan based upon the spectral-element method and LiDAR DTM. *Bulletin of the Seismological Society of America*, *99*(2 A), 681–693. http://doi.org/10.1785/0120080264

Lee, S. J., Chen, H. C., Liu, Q., Komatitsch, D., Huang, B. S., & Tromp, J. (2008). Three-dimensional simulations of seismic-wave propagation in the Taipei Basin with realistic topography based upon the spectral-element method. *Bulletin of the Seismological Society of America*, *98*(1), 253–264. http://doi.org/10.1785/0120070033

Lindsey, E. O., Natsuaki, R., Xu, X., Shimada, M., Hashimoto, M., Melgar, D., & Sandwell, D. T. (2015). Line-of-sight displacement from ALOS-2 interferometry: Mw 7.8 Gorkha Earthquake and Mw 7.3 aftershock. *Geophysical Research Letters*, *42*(16), 6655–6661. http://doi.org/10.1002/2015GL065385

Liu, C., Zheng, Y., Wang, R., Shan, B., Xie, Z., Xiong, X., & Ge, C. (2016). Rupture processes of the 2015 Mw 7.9 Gorkha earthquake and its Mw 7.3 aftershock and their implications on the seismic risk. *Tectonophysics*, *682*, 264–277. http://doi.org/10.1016/j.tecto.2016.05.034

Lizundia, B., Shrestha, S. N., Bevington, J., Davidson, R., Jaiswal, K., Jimee, G. K., … Ortiz, M. (2016). *EERI Earthquake Reconnaissance Team Report:M7.8 Gorkha, Nepal Earthquake on April 25, 2015 and its Aftershocks*. California. Retrieved from http://www.eeri.org.

Ma, S., Archuleta, R. J., & Page, M. T. (2007). Effects of large-scale surface topography on ground motions, as demonstrated by a study of the San Gabriel Mountains, Los Angeles, California. *Bulletin of the Seismological Society of America*, *97*(6), 2066–2079. http://doi.org/10.1785/0120070040

Magnoni, F., Casarotti, E., Michelini, A., Piersanti, A., Komatitsch, D., Peter, D., & Tromp, J. (2014). Spectral-Element Simulations of Seismic Waves Generated by the 2009 L'Aquila Earthquake. *Bulletin of the Seismological Society of America*, *104*(1), 73–94. http://doi.org/10.1785/0120130106

Mahesh, P., Rai, S. S., Sivaram, K., Paul, A., Gupta, S., Sarma, R., & Gaur, V. K. (2013). One-dimensional reference velocity model and precise locations of earthquake hypocenters in the Kumaon-Garhwal Himalaya. *Bulletin of the Seismological Society of America*. http://doi.org/10.1785/0120110328

Malla, S. (2015). *LESSONS OF 2015 NEPAL EARTHQUAKE DISASTER*. Zurich. Retrieved from http://californiaeqclearinghouse.org/wp-content/uploads/2015/13/Lessons_of_2015_Nepal_earthquake_disaster_by_Sujan_Malla.pdf

Martin, S. S., Hough, S. E., & Hung, C. (2015). Ground Motions from the 2015 Mw 7.8 Gorkha, Nepal, Earthquake Constrained by a Detailed Assessment of Macroseismic Data. *Seismological Research Letters*, *86*(6), 1524–1532. http://doi.org/10.1785/0220150138

McKinney, S. C. (2015). Caltech, JPL Team Captures Movement on Nepal Earthquake Fault Rupture | Caltech. Retrieved February 9, 2017, from http://www.caltech.edu/news/caltech-jpl-team-captures-movement-nepal-earthquake-fault-rupture-46709

McNamara, D. E., Yeck, W., Barnhart, W., Schulte-Pelkum, V., Bergman, E., Adhikari, L. B., … Earle, P. (2016). Source Modeling of the 2015 Mw 7.8 Nepal (Gorkha) Earthquake Sequence: Implications for Geodynamics and Earthquake Hazards. *Tectonophysics*, (TECTO-127212), 0–9. http://doi.org/10.1016/j.tecto.2016.08.004

Mencin, D., Bendick, R., Upreti, B. N., Adhikari, D. P., Gajurel, A. P., Bhattarai, R. R., … Bilham, R. (2016). Himalayan strain reservoir inferred from limited afterslip following the Gorkha earthquake. *Nature Geoscience*, *9*(7), 533–537. http://doi.org/10.1038/ngeo2734

Meza-Fajardo, K. C., & Papageorgiou, A. S. (2008). The Spectral Element Method (Sem): Formulation and Implementation Of The Method For Engineering Seismology Problems. *14th World Conference on Earthquake Engineering (14WCEE)*, (2008).

Monsalve, G., Sheehan, A., Rajaure, S., Pandey, M. R., & Wu, F. (2006). Seismicity and one-dimensional velocity structure of the Himalayan collision zone : Earthquakes in the crust and upper mantle, *111*, 1–19. http://doi.org/10.1029/2005JB004062

Moss, R. E. S., Thompson, E. M., Scott Kieffer, D., Tiwari, B., A Hashash, Y. M., Acharya, I., … Uprety, S. (2015). Geotechnical Effects of the 2015 Magnitude 7.8 Gorkha, Nepal, Earthquake and Aftershocks. *Seismological Research Letters*, *86*(6), 1514–1523. http://doi.org/10.1785/0220150158

Narayan, J. P. (2005). Study of Basin-edge Effects on the Ground Motion Characteristics Using 2.5-D Modelling. *Pure and Applied Geophysics*, *162*(2), 273–289. http://doi.org/10.1007/s00024-004-2600-8

National Oceanic and Atmospheric Administration. (2016). Earthquake damage in Mexico City, Mexico, September 19, 1985. Retrieved December 10, 2016, from https://data.noaa.gov/dataset/earthquake-damage-in-mexico-city-mexico-september-19-1985

Nguyen, K.-V., & Gatmiri, B. (2007). *Evaluation of seismic ground motion induced by topographic irregularity*. *Soil Dynamics and Earthquake Engineering* (Vol. 27).

OCHA. (2015). About OCHA Nepal. Retrieved February 10, 2017, from http://www.unocha.org/nepal/about-ocha-nepal/about-ocha-nepal

Ohsumi, T. (2015). Investigation of damage to buildings and ground truth verification for satellite data in Kathmandu Valley due to the 2015 Gorkha Earthquake.

Ohsumi, T., Mukai, Y., & Fujitani, H. (2016). Investigation of Damage in and Around Kathmandu Valley Related to the 2015 Gorkha, Nepal Earthquake and Beyond. *Geotechnical and Geological Engineering*, *34*(4), 1223–1245. http://doi.org/10.1007/s10706-016-0023-9

Okamura, M., Bhandary, N. P., Mori, S., Marasini, N., & Hazarika, H. (2015). Report on a reconnaissance survey of damage in Kathmandu caused by the 2015 Gorkha Nepal earthquake. *Soils and Foundations*, *55*(5), 1015–1029. http://doi.org/10.1016/j.sandf.2015.09.005

Oliveira, S. P., & Seriani, G. (2011). Effect of element distortion on the numerical dispersion of spectral element methods. *Communications in Computational Physics*, *9*(4), 937–958. http://doi.org/10.4208/cicp.071109.080710a

Parajuli, R. R., & Kiyono, J. (2015). Ground Motion characteristics of the 2015 gorkha earthquake, survey of Damage to stone Masonry structures and structural Field Tests. *Frontiers in Built Environment*, *1*(23), 0–12. http://doi.org/10.3389/fbuil.2015.00023

Patera, A. T. (1984). A spectral element method for fluid dynamics: Laminar flow in a channel expansion. *Journal of Computational Physics*, *54*(3), 468–488. http://doi.org/10.1016/0021-9991(84)90128-1

Pitarka, A., Irikura, K., Iwata, T., & Sekiguchi, H. (1998). Three-Dimensional Simulation of the Near-Fault Ground Motion for the 1995 Hyogo-ken Nanbu (Kobe), Japan, Earthquake. *Bulletin of the Seismological Society of America*, *88*(2), 428–440.

Qin, W., & Yao, H. (2016). Characteristics of subevents and three-stage rupture processes of the 2015Mw 7.8 Gorkha Nepal earthquake from multiple-array back projection. *Journal of Asian Earth Sciences*, *133*, 72–79. http://doi.org/10.1016/j.jseaes.2016.11.012

Qiu, J. (2015). Nepal earthquake caused fewer landslides than feared. *Nature*. http://doi.org/10.1038/nature.2015.19038

Raghukanth, S. T. G., Kumari, K. L., & Somala, S. N. (2012). Regional level ground motion simulation for a hypothetical great earthquake in the Garwhal Himalaya. *Geomatics, Natural Hazards and Risk*, *5705*(April 2013), 1–24. http://doi.org/10.1080/19475705.2012.731658

Raghukanth, S. T. G., Lakshmi Kumari, K., & Kavitha, B. (2012). Estimation of ground motion during the 18th September 2011 Sikkim Earthquake. *Geomatics, Natural Hazards and Risk*, *3*(1), 9–34. http://doi.org/10.1080/19475705.2011.646323

Rai, M. (2015). *Topographic effects in strong ground motion (PhD Thesis)*. Virginia Polytechnic Institute and State University. Retrieved from https://vtechworks.lib.vt.edu/handle/10919/56593

Rajaure, S., Asimaki, D., Thompson, E. M., Hough, S., Martin, S., Ampuero, J. P., … Paudel, L. (2016). Characterizing the Kathmandu Valley sediment response through strong motion recordings of the 2015 Gorkha earthquake sequence. *Tectonophysics*. http://doi.org/10.1016/j.tecto.2016.09.030

Restrepo, D. L. (2013). *Effect of Topography on 3D Seismic Ground Motion Simulation with an Application to the Valley of Aburra in Antioquia , Colombia (Phd Thesis)*. Carnegie Mellon University. Retrieved from http://repository.cmu.edu/dissertations Recommended

Rezaeian, M., & Gruen, A. (2011). Automatic 3D building extraction from aerial and space images for earthquake risk management. *Georisk: Assessment and Management of Risk for Engineered Systems and Geohazards*, *5*(1), 77–96. http://doi.org/10.1080/17499511003679998

Rogers, A. M., Bennett, T. J., & Katz, L. J. (1974). Topographic effect on ground motion for incident P-waves. *International Journal of Rock Mechanics and Mining Science & Geomechanics*, *11(3):55-5*. http://doi.org/DOI: 10.1016/0148-9062(74)91617-9

Sánchez-Sesma, F., Herrera, I., & Avilés, J. (1982). A Boundary Method for Elastic Wave Diffraction: Application to Scattering of SH Waves by Surface Irregularities. *Bulletin of the Seismological Society of America*, *72*(2), 473–490.

Sandia. (2016). Sandia National Laboratories: CUBIT Geometry and Mesh Generation Toolkit 13.2 Release Notes. Retrieved December 29, 2016, from https://cubit.sandia.gov/public/13.2/13.2.html

Sato, T., Graves, R. W., & Somerville, P. G. (1999). Three-dimensional finite-difference simulations of long-period strong motions in the Tokyo metropolitan area during the 1990 Odawara earthquake (MJ 5.1) and the great 1923 Kanto earthquake (MS 8.2) in Japan. *Bulletin of the Seismological Society of*

America, *89*(3), 579–607.

Scholl, R. E. (1989). Observations of the performance of buildings during the 1985 Mexico earthquake, and structural design implications. *International Journal of Mining and Geological Engineering*, *7*(1), 69–99. http://doi.org/10.1007/BF01552841

Schuberth, B. (2003). *The Spectral Element Method for Seismic Wave Propagation Theory, Implementation and Comparison to Finite Difference Methods*. (Diploma Thesis), Ludwig Maximilian University of Munich. Retrieved from https://www.geophysik.uni-muenchen.de/.../Diploma_Thesis_Bernhard_Schuberth.pdf

Schütz, A. (2015). Update: Disaster relief – DLR provides aerial images of Kathmandu. Retrieved February 9, 2017, from http://www.dlr.de/dlr/en/desktopdefault.aspx/tabid-10081/151_read-13487/#/gallery/19391

Semblat, J.-F., Kham, M., & Bard, P.-Y. (2008). Seismic-Wave Propagation in Alluvial Basins and Influence of Site-City Interaction. *Bulletin of the Seismological Society of America*, *98*(6), 2665–2678. http://doi.org/10.1785/0120080093

Semblat, J. F. (2006). Modeling seismic wave propagation and amplification in 1D / 2D / 3D linear and nonlinear unbounded media, (Table I), 1–12. http://doi.org/10.1061/(ASCE)GM.1943-5622.0000023

Shafique, M., van der Meijde, M., Kerle, N., & van der Meer, F. (2011). Impact of DEM source and resolution on topographic seismic amplification. *International Journal of Applied Earth Observation and Geoinformation*, *13*(3), 420–427. http://doi.org/10.1016/j.jag.2010.09.005

Shakal, A. F., Huang, M., Darragh, R., Cao, T., Sherburne, R., Malhotra, P., … Wampole, J. (1994). *CSMIP strong-motion records from the Northridge, California earthquake of January 17 1994*. Sacramento, California.

Shakya, M., & Kawan, C. K. (2016). Reconnaissance based damage survey of buildings in Kathmandu valley: An aftermath of 7.8Mw, 25 April 2015 Gorkha (Nepal) earthquake. *Engineering Failure Analysis*, *59*, 161–184. http://doi.org/10.1016/j.engfailanal.2015.10.003

Showstack, R. (2015). Weak Shaking Lessened Nepal Earthquake Impact. Retrieved from https://eos.org/articles/weak-shaking-lessened-nepal-earthquake-impact

Smith, W. D. (2007). The Application of Finite Element Analysis to Body Wave Propagation Problems. *Geophysical Journal of the Royal Astronomical Society*, *42*(2), 747–768. http://doi.org/10.1111/j.1365-246X.1975.tb05890.x

Spudich, P., Hellweg, M., & Lee, W. H. K. (1996). Directional Topographic Site Response at Tarzana Observed in Aftershocks of the 1994 Northridge, California, Earthquake: Implications for Mainshock Motions. *Bulletin of the Seismological Society of America*, *86*(1B), 193–208.

Stidham, C., Süss, M. P., & Shaw, J. H. (2001). 3D density and velocity model of the Los Angeles basin. In *Geological Society of America 2001 annual meeting Abstracts* (Vol. 33, p. 299). Boston: Geological Society of America.

Stupazzini, M., Paolucci, R., & Igel, H. (2009). Near-fault earthquake ground-motion simulation in the Grenoble Valley by a high-performance spectral element code. *Bulletin of the Seismological Society of America*, *99*(1), 286–301. http://doi.org/10.1785/0120080274

Takai, N., Shigefuji, M., Rajaure, S., Bijukchhen, S., Ichiyanagi, M., Dhital, M. R., & Sasatani, T. (2016). Strong ground motion in the Kathmandu Valley during the 2015 Gorkha, Nepal, earthquake. *Earth, Planets and Space*, *68*(1), 10. http://doi.org/10.1186/s40623-016-0383-7

Trifunac, M. D., & Hudson, D. E. (1971). Analysis of the Pacoima dam accelerogram—San Fernando, California, earthquake of 1971. *Bulletin of the Seismological Society of America*, *61 (5)*, 1393–1411. Retrieved from http://resolver.caltech.edu/CaltechAUTHORS:20140915-125446485

Tromp, J., Komatitsch, D., & Liu, Q. (2008). Spectral-Element and Adjoint Methods in Seismology. *COMMUNICATIONS IN COMPUTATIONAL PHYSICS*, *3*(1), 1–32. Retrieved from http://www.global-sci.com/

Tsai, V. C., Nettles, M., Ekström, G., & Dziewonski, A. M. (2005). Multiple CMT source analysis of the 2004 Sumatra earthquake. *Geophysical Research Letters*, *32*(17), 1–4. http://doi.org/10.1029/2005GL023813

USAID. (2016). Retrieved December 27, 2016, from https://www.usaid.gov/nepal-earthquake/fy15/fs01

USGS. (2015). M 7.8 - 36km E of Khudi, Nepal :Updated Finite Fault Results for the Apr 25, 2015 Mw 7.9 35 km E of Lamjung, Nepal Earthquake (Version 2). Retrieved December 20, 2016, from http://earthquake.usgs.gov/earthquakes/eventpage/us20002926#finite-fault

USGS. (2016a). Earthquake Hazards Program. Retrieved May 20, 2016, from http://earthquake.usgs.gov/

USGS. (2016b). The M7 . 8 Nepal Earthquake , 2015 – A Small Push to Mt . Everest In the Shadow of Mountains. Retrieved August 23, 2016, from http://earthquake.usgs.gov/research/fy16-nepal2015/

Wang, K., & Fialko, Y. (2015). Slip model of the 2015 Mw 7.8 Gorkha (Nepal) earthquake from inversions of ALOS-2 and GPS data. *Geophysical Research Letters*, *42*(18), 7452–7458. http://doi.org/10.1002/2015GL065201

World Bank Group. (2015). *Nepal Earthquake Post Disaster Needs Aassessment : Sector Reports*. Washington, DC. Retrieved from https://openknowledge.worldbank.org/handle/10986/22096

Wu, H., Masaki, K., Irikura, K., Saguchi, K., Kurahashi, & Susumu. (2012). Relationship between Building Damage Ratios and Ground Motion Characteristics during the 2011 Tohoku Earthquake. *Journal of Natural Disaster Science*, *34*(1), 59–78. http://doi.org/DOI: 10.2328/jnds.34.59

Yadav, R. K., Roy, P. N. S., Gupta, S. K., Khan, P. K., Catherine, J. K., Prajapati, S. K., … Gahalaut, V. K. (2016). Rupture model of Mw 7.8 2015 Gorkha, Nepal earthquake: Constraints from GPS measurements of coseismic offsets. *Journal of Asian Earth Sciences*, *133*, 56–61. http://doi.org/10.1016/j.jseaes.2016.04.015

Yagi, Y., & Okuwaki, R. (2015). Integrated seismic source model of the 2015 Gorkha, Nepal, earthquake. *Geophysical Research Letters*, *42*(15), 6229–6235. http://doi.org/10.1002/2015GL064995

Yenier, E., & Atkinson, G. M. (2014). Equivalent point-source modeling of moderate-to-large magnitude earthquakes and associated ground-motion saturation effects. *Bulletin of the Seismological Society of America*, *104*(3), 1458–1478. http://doi.org/10.1785/0120130147

Yin, A. (2006). Cenozoic tectonic evolution of the Himalayan orogen as constrained by along-strike variation of structural geometry , exhumation history , and foreland sedimentation. *Earth-Science Reviews*, *76*(1), 1–131. http://doi.org/10.1016/j.earscirev.2005.05.004

Yue, H., Simons, M., Duputel, Z., Jiang, J., Fielding, E., Liang, C., … Samsonov, S. V. (2016). Depth varying rupture properties during the 2015 Mw 7.8 Gorkha (Nepal) earthquake. http://doi.org/10.1016/j.tecto.2016.07.005

Yun, S.-H., Hudnut, K., Owen, S., Webb, F., Simons, M., Sacco, P., … Coletta, A. (2015). Rapid Damage Mapping for the 2015 M w 7.8 Gorkha Earthquake Using Synthetic Aperture Radar Data from COSMO–SkyMed and ALOS-2 Satellites. *Seismological Research Letters*, *86*(6), 1549–1556. http://doi.org/10.1785/0220150152

Zhang, H., Van Der Lee, S., & Ge, Z. (2016). Multiarray rupture imaging of the devastating 2015 Gorkha, Nepal, earthquake sequence. *Geophysical Research Letters*, *43*(2), 584–591. http://doi.org/10.1002/2015GL066657

Zhang, L., Li, J., Liao, W., & Wang, Q. (2016). Source rupture process of the 2015 Gorkha, Nepal Mw7.9 earthquake and its tectonic implications. *Geodesy and Geodynamics*, *7*(2), 124–131. http://doi.org/10.1016/j.geog.2016.03.001

Zhang, W., Shen, Y., & Chen, X. (2008). Numerical simulation of strong ground motion for the M 8.0 Wenchuan earthquake of 12 May 2008. *Science in China Series D: Earth Sciences*, *51*(3), 1673–1682. http://doi.org/10.1007/s11430-008-0130-4

Zhao, W., Nelson, K. D., Che, J., Quo, J., Lu, D., Wu, C., & Liu, X. (1993). Deep seismic reflection evidence for continental underthrusting beneath southern Tibet. *Nature*, *366*(6455), 557–559. Retrieved from http://dx.doi.org/10.1038/366557a0

Annex –A1

Centroid Moment Tensor (CMT) Solution of the 2015 Mw 7.8 Nepal Earthquake
(Source : Global CMT Catalog, http://www.globalcmt.org/)

```
PDEW2015  4 25  6 11 26.30  28.1500   84.7100  15.0 0.0 7.8 NEPAL
event name:     201504250611A
time shift:     32.3400
half duration:  21.3000
latitude:       27.9100
longitude:      85.3300
depth:          12.0000
Mrr:       1.760000e+27
Mtt:      -1.820000e+27
Mpp:       5.790000e+25
Mrt:       8.040000e+27
Mrp:      -1.510000e+27
Mtp:       4.750000e+26
```

Annex –A2

Details of Damage Data Prepared by UNOSAT, Copernicus, NGA and NASA ARIA

Sl	Issue	UNOSAT	Copernicus	UNOSA+COPERNICUS (consolidated)	NGA	NASA ARIA	NGA (consolidated)
1	How was the damage data prepared?	World view 1 & 3, GeoEye-1, Pleiades 0.5m satellite image analysis	World view-2/pan- sharpened imagery (0.5m) analysis	Combining the data of UNOSAT and Copernicus. Work done by UNITAR	Multiple satellite image analysis, Direct field observations	COSMO–SkyMed and ALOS-2 SAR	Combining the data of NGA, and NASA. Work done by NGA
2	Data format	Point and polygon shape file	Point shape file	Point shape file	Point and polygon shape file	Raster	Point and polygon shape file
3	Mapped area	Mainly focus on the districts in epicenter areas (but also covered few areas of Kathmandu and surrounding districts	-same as UNOSAT-	Mainly epicenter areas but also covered some parts of Kathmandu and surrounding districts	Wide coverage. Mainly focus on Kathmandu and all surrounding districts. Also covered epicenter areas but in small scale	Mainly focus on Kathmandu and all surrounding districts.	Mainly focused on Kathmandu and surrounding districts. Also covered epicenter areas but in small scale
4	Is type and height information of the damaged buildings provided?	No	No	No	No	No	No

(Continued…)

Sl	Issue	UNOSAT	Copernicus	UNOSA+COPERNICUS (consolidated)	NGA	NASA ARIA	NGA (consolidated)
5	Damage grade	Destroyed Moderate damage Severe damage	Not affected Negligible to slight damage (EMS-1) Completely destroyed (EMS-5) Unknown	Destroyed Moderate damage Severe damage	Affected Minor Major Destroyed	Yellow to red pixels indicate increasingly more significant damage	Possible damage Moderate Damage Severe Damage Destroyed
6	Does damage grade conform to EMS-98 scale?	Criteria for damage classification are not explained. So, difficult to conclude about the conformity with EMS-98	Two damage grades directly conform to EMS-1 and EMS-5 grade.	Criteria for damage classification are not explained. So, difficult to conclude about the conformity with EMS-98	Criteria for damage classification are not explained. So, difficult to conclude about the conformity with EMS-98	-	Criteria for damage classification are not explained. So, difficult to conclude about the conformity with EMS-98.
7	Is damage data overlapped with other organization?	Mainly overlapped with Copernicus. Some overlapping with NGA but in few areas	Mainly overlapped with UNOSAT. Some overlapping with NGA but in few areas	Overlapped with NGA but in few areas	Overlapped with UNOSAT and Copernicus but in few areas	-	Overlapped with UNOSAT and Copernicus but in few areas
8	If overlapped, how is about the agreement between the damage data prepared by two or more organizations in the overlapped area?	Good agreement with Copernicus.	Good agreement with UNOSAT.	Good agreement with NGA for classifying "destroyed" damage grade. However, some disagreement is found in Moderate and severe damage classification	Good agreement with UNOSAT and Copernicus for classifying "destroyed" damage grade. However, some disagreement is found in Moderate and severe damage classification	Good agreement with NGA	Good agreement with UNOSAT and Copernicus for classifying "destroyed" damage grade. However, some disagreement is found in Moderate and severe damage classification

Annex –A3

Spectral Element Mesh without Topography with one Tripling Layer

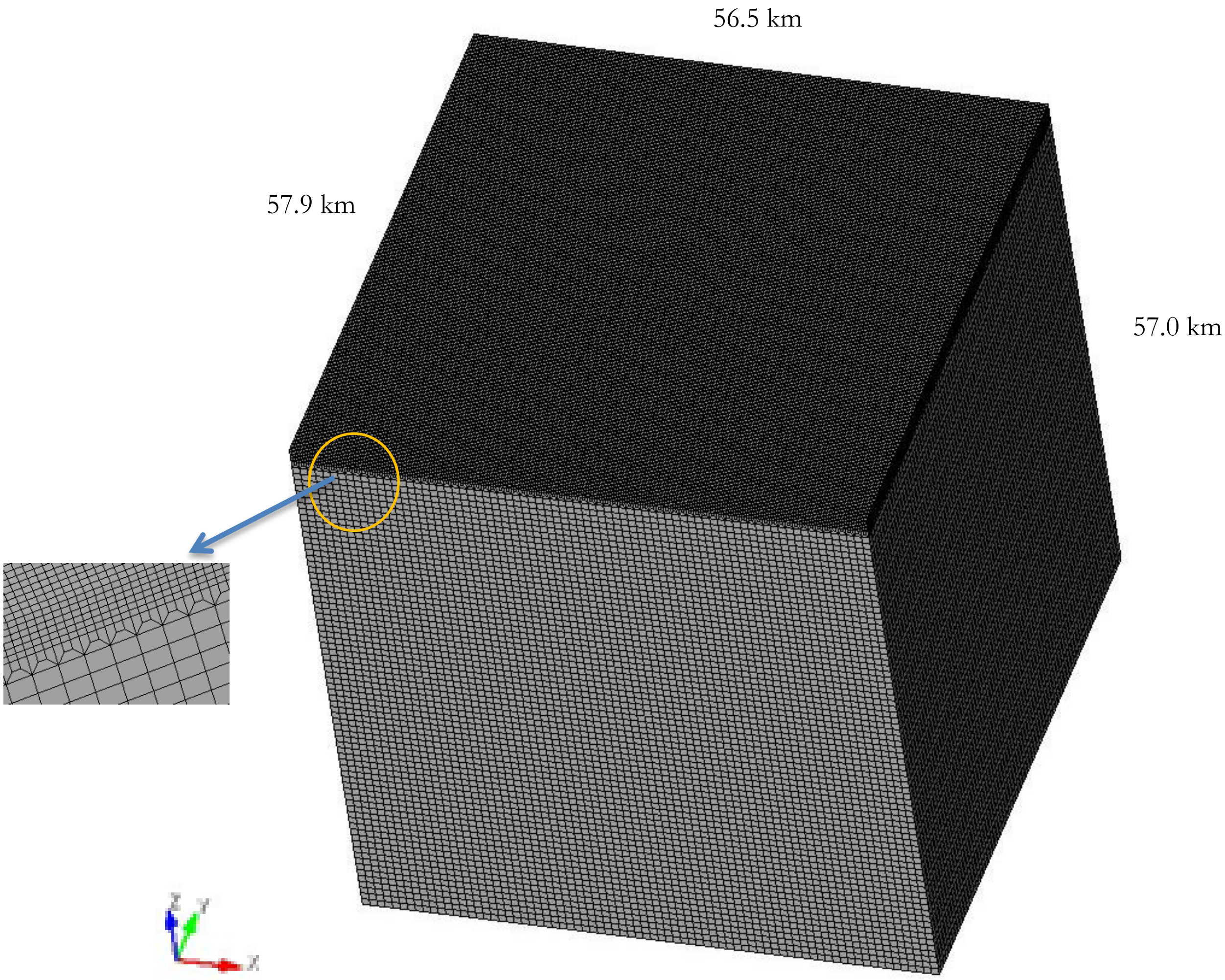

Annex –A4

A4.1: Output file (output_solver.txt) generated after simulation (For mesh with topography)

```
**********************************************
**** Specfem 3-D Solver - MPI version f90 ****
**********************************************
Version: v2.0.2-2075-g36a8e9b
Fixing slow underflow trapping problem using small initial field

There are           16  MPI processes
Processes are numbered from 0 to          15

There is a total of           16  slices

 NDIM =            3

 NGLLX =            5
 NGLLY =            5
 NGLLZ =            5

using single precision for the calculations

smallest and largest possible floating-point numbers are:   1.17549435E-38  3.40282347E+38

velocity model:   default

total acoustic elements    :           0
total elastic elements     :      854698
total poroelastic elements :           0

********
minimum and maximum number of elements
and points in the CUBIT + SCOTCH mesh:

NSPEC_global_min =        28531
NSPEC_global_max =        32051
NSPEC_global_max / NSPEC_global_min imbalance =    1.1233746      =    12.337458      %
NSPEC_global_sum =       854698

NGLOB_global_min =      1880570
NGLOB_global_max =      2126456
NGLOB_global_max / NGLOB_global_min imbalance =    1.1307508      =    13.075078      %
NGLOB_global_sum =     56319007

If you have elements of a single type (all acoustic, all elastic, all poroelastic, and without CPML)
in the whole mesh, then there should be no significant imbalance in the above numbers.
Otherwise, it is normal to have imbalance in elements and points because the domain decomposer
compensates for the different cost of different elements by partitioning them unevenly among processes.
********
********
Model: P velocity min,max =    5849.9995       5849.9995
Model: S velocity min,max =    3370.0002       3370.0002

Model: Poisson's ratio min,max =    0.25165960      0.25165960
********

*********************************************
*** Verification of simulation parameters ***
*********************************************

*** Xmin and Xmax of the model =    313990.50       370496.13
*** Ymin and Ymax of the model =    3044630.3       3102599.3
*** Zmin and Zmax of the model =   -57000.000       4498.6738

*** Max GLL point distance =    503.20901
*** Min GLL point distance =    9.8066854
*** Max/min ratio =    51.312855

*** Max element size =    1537.0857
*** Min element size =    56.665493
*** Max/min ratio =    27.125603

*** Minimum period resolved =    0.57013559
*** Maximum suggested time step =    8.38178326E-04

*** for DT :    5.0000000000000010E-004
```

Maximum Δt suggested by the solver

Used Δt for simulation

(Continued...)

Annex –A4

A4.1: Output file (output_solver.txt) generated after simulation (For mesh without topography)

```
**********************************************
**** Specfem 3-D Solver - MPI version f90 ****
**********************************************
Version: v2.0.2-2075-g36a8e9b
Fixing slow underflow trapping problem using small initial field

There are           16  MPI processes
Processes are numbered from 0 to           15

There is a total of           16  slices

 NDIM =            3

 NGLLX =            5
 NGLLY =            5
 NGLLZ =            5

using single precision for the calculations

smallest and largest possible floating-point numbers are:   1.17549435E-38   3.40282347E+38

velocity model:   default

total acoustic elements    :           0
total elastic elements     :      841776
total poroelastic elements :           0

********
minimum and maximum number of elements
and points in the CUBIT + SCOTCH mesh:

NSPEC_global_min =        39989
NSPEC_global_max =        43914
NSPEC_global_max / NSPEC_global_min imbalance =    1.0981520      =    9.8151989      %
NSPEC_global_sum =       841776

NGLOB_global_min =      2628549
NGLOB_global_max =      2873885
NGLOB_global_max / NGLOB_global_min imbalance =    1.0933352      =    9.3335142      %
NGLOB_global_sum =     55215868

If you have elements of a single type (all acoustic, all elastic, all poroelastic, and without CPML)
in the whole mesh, then there should be no significant imbalance in the above numbers.
Otherwise, it is normal to have imbalance in elements and points because the domain decomposer
compensates for the different cost of different elements by partitioning them unevenly among processes.
********
********
Model: P velocity min,max =    5849.9995       5849.9995
Model: S velocity min,max =    3370.0002       3370.0002

Model: Poisson's ratio min,max =    0.25165960      0.25165960
********

*********************************************
*** Verification of simulation parameters ***
*********************************************

*** Xmin and Xmax of the model =    313990.50       370496.13
*** Ymin and Ymax of the model =    3044630.3       3102599.3
*** Zmin and Zmax of the model =   -57000.000       0.0000000

*** Max GLL point distance =    244.01445
*** Min GLL point distance =    31.546021
*** Max/min ratio =    7.7351894

*** Max element size =    745.29358
*** Min element size =    182.69226
*** Max/min ratio =    4.0795026

*** Minimum period resolved =    0.27644420
*** Maximum suggested time step =    2.69624125E-03

*** for DT :    2.50000000000000005E-003
```

Maximum Δt suggested by the solver

Used Δt for simulation

Annex –A5: Skewness of Mesh

With Topography			Without Topography		
Skewness	Number of elements	% of total elements	Skewness	Number of elements	% of total elements
0.01	15833	1.85	0.01	770640	91.55
0.04	70646	8.27	0.04	0	0.00
0.06	94308	11.03	0.06	0	0.00
0.09	92381	10.81	0.09	0	0.00
0.11	83057	9.72	0.11	0	0.00
0.14	77169	9.03	0.14	0	0.00
0.16	70534	8.25	0.16	0	0.00
0.19	63649	7.45	0.19	0	0.00
0.21	52376	6.13	0.21	0	0.00
0.24	41338	4.84	0.24	0	0.00
0.26	31952	3.74	0.26	0	0.00
0.29	26132	3.06	0.29	0	0.00
0.31	20870	2.44	0.31	0	0.00
0.34	17740	2.08	0.34	0	0.00
0.36	14234	1.67	0.36	1123	0.13
0.39	10644	1.25	0.39	4805	0.57
0.41	8816	1.03	0.41	23712	2.82
0.44	6260	0.73	0.44	0	0.00
0.46	4657	0.54	0.46	0	0.00
0.49	3428	0.40	0.49	0	0.00
0.51	2703	0.32	0.51	0	0.00
0.54	2304	0.27	0.54	0	0.00
0.56	2828	0.33	0.56	0	0.00
0.59	5758	0.67	0.59	17784	2.11
0.61	8970	1.05	0.61	15318	1.82
0.64	9422	1.10	0.64	8394	1.00
0.66	7435	0.87	0.66	0	0.00
0.69	4632	0.54	0.69	0	0.00
0.71	2603	0.30	0.71	0	0.00
0.74	1339	0.16	0.74	0	0.00
0.76	664	0.08	0.76	0	0.00
0.79	16	0.00	0.79	0	0.00
0.81	0	0.00	0.81	0	0.00
0.84	0	0.00	0.84	0	0.00
0.86	0	0.00	0.86	0	0.00
0.89	0	0.00	0.89	0	0.00
0.91	0	0.00	0.91	0	0.00
0.94	0	0.00	0.94	0	0.00
0.96	0	0.00	0.96	0	0.00
0.99	0	0.00	0.99	0	0.00
Total	854698	100.00	Total	841776	100.00

Annex –A6

Peak ground Displacement (PGD) Maps of four hypothetical scenarios P1 to P4 (from top to bottom). In each case, the left figure is the PGD map with topography and the right one is the PGD map without topography

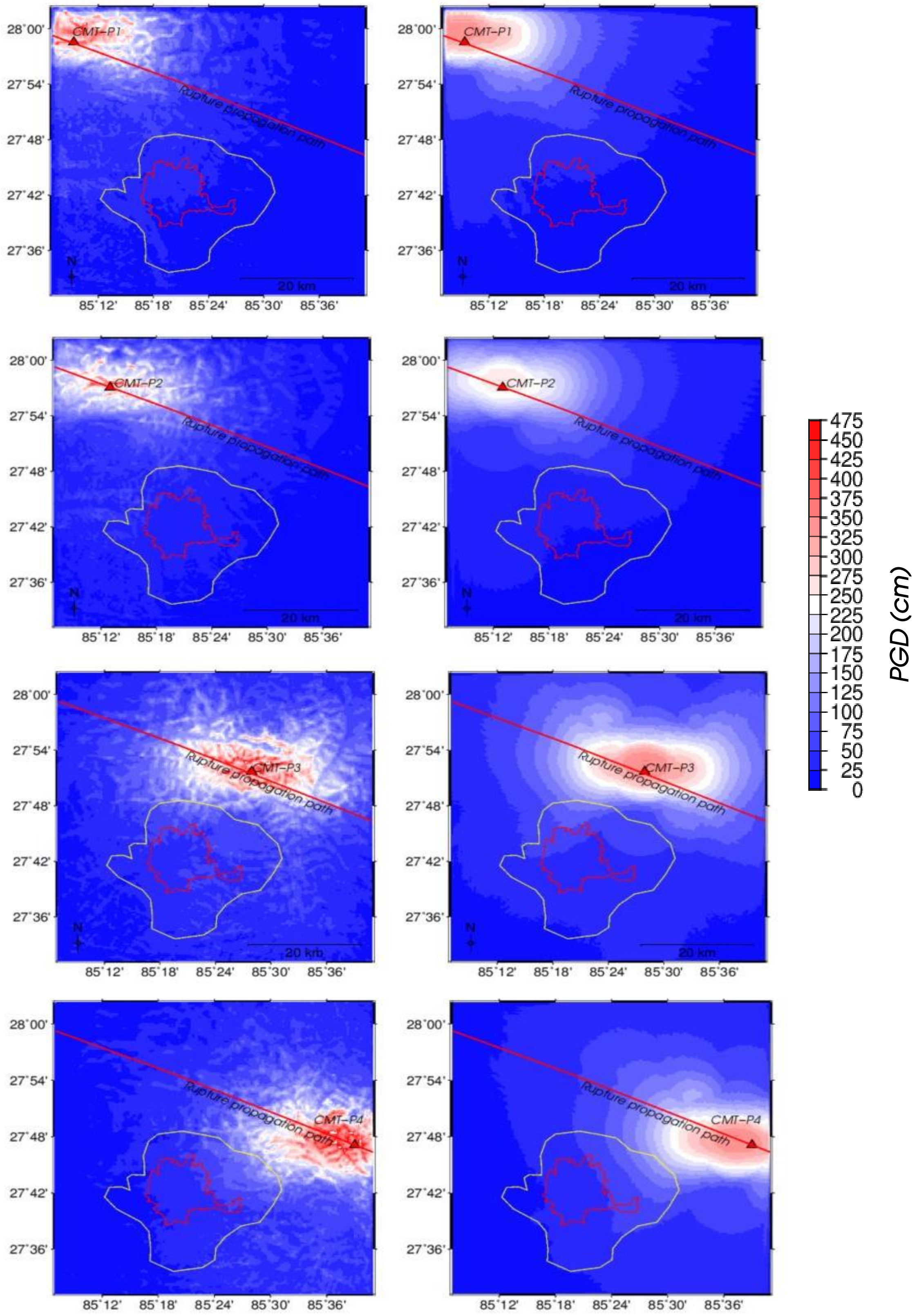

The End